UNIVERSITY OF CALIFORNIA
Los Angeles

Modeling Asteroid Shapes and Orbits with Radar Data

A dissertation submitted in partial satisfaction
of the requirements for the degree
Doctor of Philosophy in Astronomy

by

Adam Hodge Greenberg

2017

Abstract of the Dissertation

Modeling Asteroid Shapes and Orbits with Radar Data

by

Adam Hodge Greenberg
Doctor of Philosophy in Astronomy
University of California, Los Angeles, 2017
Professor Jean-Luc Margot, Chair

The purpose of this work is to describe and advance the use of radar data for the determination of asteroid orbits, shapes, and physical characteristics. The data used for these goals include radar images and spectra, as well as radar range and velocity measurements. Herein, I describe improved algorithms for the inversion of asteroid shapes from radar images and spectra, and demonstrate that these algorithms improve shape determination runtime by a factor of two, as well as improve accuracy. I also use radar astrometry, along with optical plane-of-sky observations, to accurately determine asteroid orbits. The results, applied across a sample of 159 near-Earth asteroids, demonstrate that it is possible to constrain the physical characteristics of these objects using dynamics. I also use the size of this sample (currently the largest published) to perform statistical analyses of the results. Finally, I describe radar observations that I took of the near-Earth asteroid 1566 Icarus, and apply the techniques described above to these data. I determine a shape and spin model for this object, and describe several of its heretofore unknown unusual surface scattering properties.

The dissertation of Adam Hodge Greenberg is approved.

David Paige

Michael P. Fitzgerald

Edward Wright

Jean-Luc Margot, Committee Chair

University of California, Los Angeles

2017

To my wife, for keeping me sane,

and to Pansy, for foreseeing an unlikely future.

Table of Contents

List of Figures

List of Tables

Acknowledgments

I gratefully acknowledge the American Astronomical Society and IOP Publishing for their permission to reprint articles originally published in The Astronomical Journal.

To my advisor, Jean-Luc – you have supported me, not just as a student and mentee, but also has a friend. I can still remember that first meeting in your PAB office three years ago, when you described the terrifying-sounding project that would become my thesis work. On days that I felt overwhelmed, you helped guide me through the process of becoming a better scientist. I am lucky to have had you as an advisor.

To Ashok, Shantanu, and the various office-mates throughout the years – thank you for the tea-breaks, physics discussions, puzzle sessions, and balance-board mishaps.

And of course, to my wife. You have been there for everything from comps nightmares to late-night code angst ("I swear it was working yesterday!"). I'm thankful that I got to grow up with you, and I can't wait to grow old with you too. You are a better partner than I deserve.

Vita

2012	B.A. (Astrophysics), Columbia University, New York, New York.
2013	M.S. (Astronomy), UCLA, Los Angeles, California.

Publications and Presentations

Greenberg, Adam H.; Margot, Jean-Luc; Verma, Ashok K.; Taylor, Patrick A.; Naidu, Shantanu P.; Brozovic, Marina.; Benner, Lance A. M. , *Asteroid 1566 Icarus's Size, Shape, Orbit, and Yarkovsky Drift from Radar Observations*, The Astronomical Journal, Volume 153, Issue 3, article id. 108, 16 pp. (2017)

Greenberg, Adam H.; Margot, Jean-Luc, *Improved Algorithms for Radar-based Reconstruction of Asteroid Shapes*, The Astronomical Journal, Volume 150, Issue 4, article id. 114, 10 pp. (2015)

Greenberg, Adam H.; Margot, Jean-Luc; Verma, Ashok K.; Taylor, Patrick A., *Yarkovsky Drift Detections for 159 Near-Earth Asteroids*, The Astronomical Journal, (submitted)

Greenberg, Adam H.; McGuire, Chris; Kavner, Abby; *The Automatic Peak EXtractor (APEx) – A New Tool for X-Ray Diffraction Feature Extraction*, (in preparation)

Greenberg, A.; Erasmus, N.; Nesvold, E. R.; van Heerden, E.; Galache, J. L.; Dahlstrom, E.; Marchis, F. , *The Deflector Selector: A Machine Learning Framework for Prioritizing Deflection Technology Development*, Planetary Defense Conference (2017)

Greenberg, Adam; Margot, Jean-Luc; *Non-Gravitational Perturbations And The Importance Of Radar Observations On Neo Trajectory Determination*, Planetary Defense Conference (2017)

Lesyna, Larry; Margot, Jean-Luc; Greenberg, Adam; Shinde, Akshay; Alladi, Yashaswi; Prasad MN, Srinivas; Bowman, Oliver; Fisher, Callum; Gyalay, Szilard; McKibbin, William; Miles, Brittany E.; Nguyen, Donald; Power, Conor; Ramani, Namrata; Raviprasad, Rashmi; Santana, Jesse, *The Benefits of Adding SETI to the University Curriculum and What We Have Learned from a SETI Course Recently Offered at UCLA*, American Astronomical Society, AAS Meeting #229, id.333.03, (2017)

McGuire, Chris; Greenberg, Adam; Santamari-Perez, David; Makhluf, Adam; Kavner, Abby, *Isothermal equation of state of Fe5Si3 up to 96 GPa*, COMPRES Annual Meeting, (2016)

Raissi, Chedy; Lamee, Mehdi; Mosiane, Olorato; Vassallo, Corinne; Busch, Michael W.; Greenberg, Adam; Benner, Lance A. M.; Naidu, Shantanu P.; Duong, Nicholas, *New Approaches For Asteroid Spin State and Shape Modeling From Delay-Doppler Radar Images*, American Astronomical Society, DPS meeting #48, id.326.11, (2016)

Introduction

Earth-based radar is a powerful tool for gathering information about bodies in the Solar System. Radar observations can dramatically improve the determination of the physical properties and orbital elements of small bodies (such as asteroids and comets). Unlike most observational techniques inside the Solar System, radar does not rely on any external sources of light, be it reflected sunlight, transmitted starlight, or thermal emission. This human-controlled illumination allows for greater flexibility with respect to the observations. In addition, because of the wavelengths involved, radar observations can be performed during the day, further enhancing this flexibility. Radar also has the ability to probe an object's sub-surface properties, which can give important information about the object such as porosity, surface and sub-surface dielectric constant, and the presence of near-surface ice.

Radar is particularly useful for studying Near-Earth Objects (NEOs). As fragments of leftover planetesimals, NEOs serve as a window into the processes that governed the formation of the Solar System. NEO studies probe the accretional, collisional, erosional, radiative, and tidal processes which shape the continued evolution of the minor planets. Determination of NEO orbits and gravity environments opens the door to human exploration of these objects, including potentially valuable sample return missions. Arguably most important of all, the discovery, categorization, and orbit determination of NEOs, as mandated by the United States' Congress, helps identify those objects which are potentially hazardous to life on Earth.

An important development in the past two decades has been the formulation and implementation of algorithms for asteroid shape reconstruction based on radar data (Hudson, 1993; Hudson & Ostro, 1994; Ostro et al., 1995; Hudson & Ostro, 1995). This problem is not trivial because it requires the joint estimation

of the spin state and shape of the asteroid. Because of the nature of radar data, recovery of the spin state depends on knowledge of the shape and vice versa. Even with perfect spin state information, certain peculiarities of radar images (such as the two-to-one or several-to-one mapping between surface elements on the object and pixels within the radar image) make recovery of the physical shape challenging (Ostro, 1993). This is a computationally intensive problem, potentially involving hundreds to thousands of free parameters and millions of data points.

Despite the computational cost, astronomers are keen on deriving shape and spin information from asteroid radar images. The most compelling reason to do so is the fact that radar is the only Earth-based technique that can produce detailed three-dimensional information of near-Earth objects. This is possible because radar instruments achieve spatial resolutions that dramatically surpass the diffraction limit. In other words, radar instruments can resolve objects substantially smaller than the beamwidth of the antenna used to obtain the images. For example, the Arecibo telescope, the primary instrument used for the data presented in this paper, has a beamwidth of $\sim$2 arcminutes at the nominal 2380 MHz frequency of the radar. Yet observers can easily gather shape information to an accuracy of decameters for objects several millions of kilometers from Earth, achieving an effective spatial resolution of $\sim$1 milliarcsecond.

Radar ranging is also extremely valuable with regards to accurate modelling of asteroids' orbits. Radar can acquire range data for objects several lunar distances from the Earth, at accuracies on the level of only a few meters. This level of fractional precision (one part in $\sim 10^8$) provides an additional level of constraint for orbit determination, beyond that which can be achieved by optical (i.e., plane-of-sky angular) observations alone. Furthermore, radar range data are spatially orthogonal to optical observations, providing constraints that lie out of the plane-of-sky.

In the following chapters I will discuss applications of, and improvements upon,

analyses of radar data. In Chapter 1 (Greenberg & Margot, 2015), I will discuss how radar imaging can be used to reconstruct asteroid shapes for objects far too distant to observe in detail with standard optical techniques. I will also present a new method for radar image analysis, and present testing and results of this new technique. In Chapter 2 (Greenberg et al. 2017b, AJ, submitted), I will describe how both radar and optical data can be used to gain extremely accurate knowledge of asteroid orbits – accurate enough to detect and quantify subtle, non-gravitational perturbational forces acting on these orbits. I will present a list of objects for which I have measured these perturbatory forces, and discuss what interpretations can be made on the basis of these measurements. I will also examine the extent to which radar observations aid in the detection of these forces. Finally, in Chapter 3 (Greenberg et al., 2017), I will present the first ever radar images and range measurements taken of the asteroid 1566 Icarus. I will discuss both the shape inversion of Icarus from radar imaging data, as well as the measurement of non-Keplerian orbit-perturbing forces on this object. I will show how these two (seemingly disparate) forms of data can complement eachothers' analysis, and discuss Icarus' unusual observational history and confounding surface.

CHAPTER 1

Improved Algorithms for Radar-Based Reconstruction of Asteroid Shapes

1.1 Introduction

Asteroid shape data are important for various reasons. Knowledge of the shape provides clues about the formation and interaction history of asteroids. For example, radar-derived shapes of asteroids have been instrumental in identifying binary asteroids and contact binaries, which represent ∼16% and ∼10% of the population, respectively (Margot et al., 2002; Benner et al., 2008). They have also provided strong evidence that NEA binaries form by a spin-up and mass shedding process (Margot et al., 2002; Ostro et al., 2006). For single asteroids, knowledge of the morphology guides interpretation of the collisional history and surface modification processes.

Shapes also affect spin evolution during two-body interactions (e.g., torques during close planetary encounters) and orbital evolution of binary NEAs (e.g., tidal, gravitational, and non-gravitational interactions between components) (e.g., Margot et al., 2002; Ostro et al., 2006; Scheeres et al., 2006; Ćuk & Nesvorný, 2010; Jacobson et al., 2014; Naidu & Margot, 2015). Finally, shapes are needed when calculating the gravity environment near asteroids, which is of special importance for proximity operations (Fujiwara et al., 2006; Naidu et al., 2013; Nolan et al., 2013; Takahashi & Scheeres, 2014).

The determination of an asteroid's spin state from radar data is equally valu-

able. In contrast to lightcurve period determinations, which are neither sidereal nor synodic, the radar-based measurements yield sidereal periods. These estimates are needed to test the agreement between physical theories and observations, e.g., the change in asteroid spin rate due to sunlight (e.g., Taylor et al., 2007; Lowry et al., 2007) and subsequent shape evolution (e.g., Harris et al., 2009; Fahnestock & Scheeres, 2009). Proper modeling of the Yarkovsky perturbations to an asteroid's heliocentric orbit or to the evolution of binary orbits (e.g., Margot et al., 2015) also require knowledge of the spin state. Finally, important insights can be gained about asteroid physical properties and collisional evolution from the spin distributions of both regular rotators and non-principal-axis rotators (e.g., Pravec et al., 2002).

In the following sections, we will present the methods that are currently employed to reconstruct radar shapes from asteroids. We will discuss some of the limitations of these techniques, and present the theory behind a set of improvements that we have implemented for the reconstruction of radar-derived shapes. We will quantify the extent of these improvements, and finally, discuss future changes that can be made to bolster these methods.

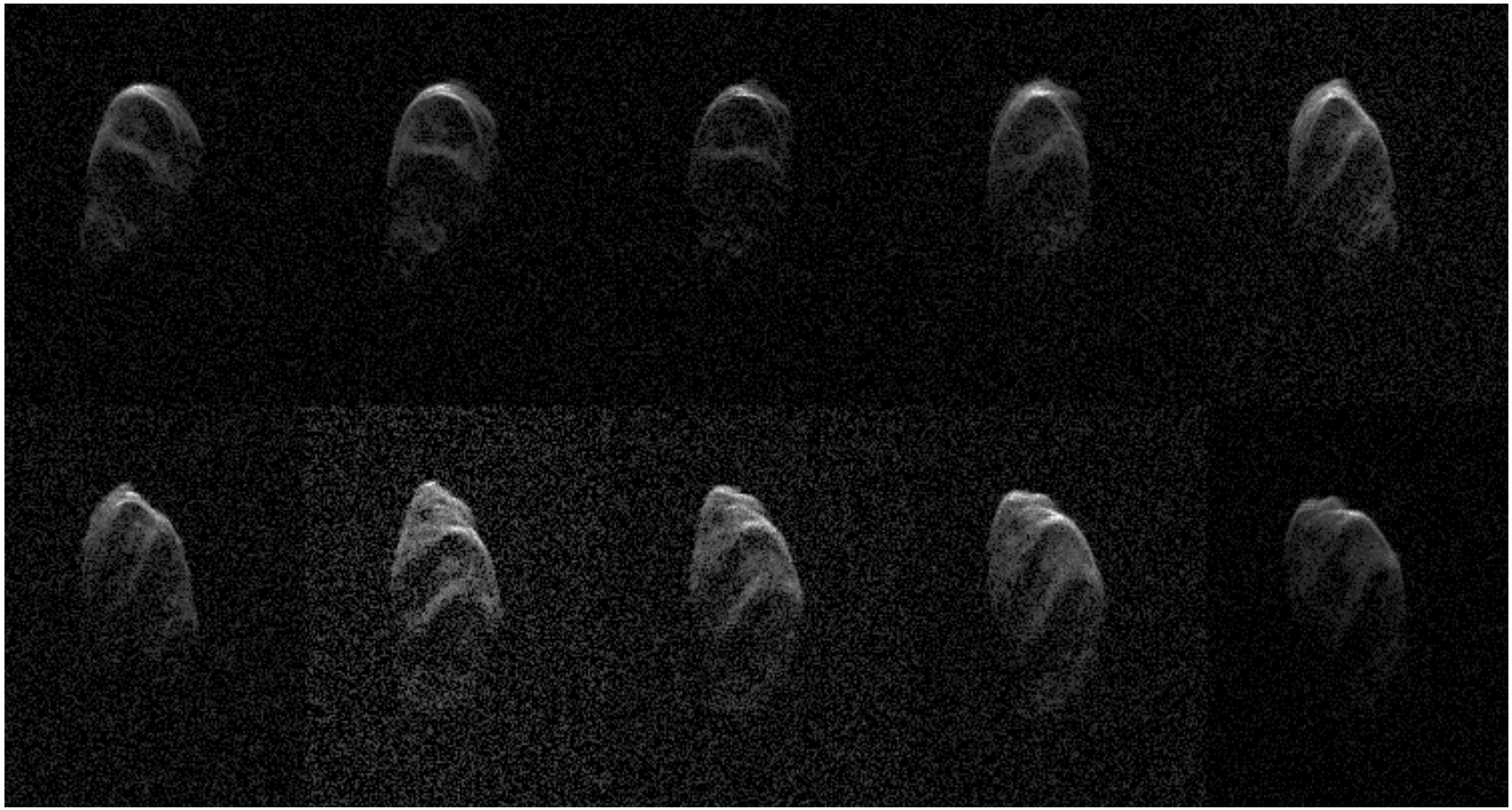

Figure 1.1: A time-series of range-Doppler images of the asteroid 2000 ET70 (Naidu et al., 2013), starting in the top left and proceeding to the right. The epochs of consecutive images are separated by 18 minutes. Distance from the observer increases downwards, and Doppler increases to the right.

1.2 Current Method

Asteroid shapes and spin states are currently modeled using the `shape` software package (Hudson, 1993; Magri et al., 2007b). `shape` takes a model for the asteroid, which is based on both shape and spin parameters, as well as scattering behavior, and projects that model into the same space as that of the radar observables. This space, called the range-Doppler space, has dimensions of range and line-of-sight velocity (Figure 1.1). `shape` can also handle optical lightcurve data when fitting for asteroid shapes, but we did not use this capability in this paper.

`shape` then compares the mapping of the model into this space to the radar observables, and makes changes to the model parameters in an attempt to minimize the sum of squares of residuals. `shape` uses increasing model complexity to build up a representation for the asteroid, from a basic ellipsoid model to capture gross features, to a spherical harmonic model which can represent finer surface elements (See section 1.5.1) and finally a model based on contiguous triangular facets (hereafter vertex model). The spin state is generally estimated in the early stages of the shape fitting – this is normally done by using trial values of the spin state while simultaneously fitting for the shape itself.

`shape` currently uses a Sequential Parameter Fit (SPF) mechanism to adjust the model following a comparison between the model projection and the radar observables. SPF minimizes χ^2 using a "bracket and Brent" method (Press et al., 1992) – for each iteration, this process minimizes χ^2 for variations in that individual parameter only, while all other parameters are held constant. This process is not only slow, but it also does not guarantee convergence on a global minimum, or even the nearest local minimum, because minimization always progresses along a single parameter axis at a time. We have worked towards replacing the SPF currently implemented in `shape` with a modified Square Root Information Filter (SRIF), as outlined in section 1.3.1.

1.3 Solution via Normal Equations

Before detailing the mechanics of the SRIF, it is worth discussing the Normal Equations Method (NEM), to which SRIF is related (Press et al., 1992). A classical NEM minimizes the weighted residuals between a model and data with noise assumed to be Gaussian by determining the direction in parameter space in which χ^2 is decreasing fastest. Specifically, suppose one has a set of m observables, $\vec{z}$, with weights that are the diagonal elements of an $m \times m$ matrix W, and a model function $\vec{f}(\vec{x})$, where $\vec{x}$ is an n-dimensional parameter vector. Assuming independent data points with Gaussian-distributed errors, the probability of the model matching the data is given by

$$p(\vec{f}(\vec{x}) \mid \vec{z}) \propto p(\vec{z} \mid \vec{f}(\vec{x})) \propto \exp(-\frac{1}{2}\vec{R}^\intercal W \vec{R}),$$

where $\vec{R} = \vec{z} - \vec{f}(\vec{x})$. Therefore maximizing the model probability is the same as minimizing the value

$$\chi^2(\vec{x}) = \vec{R}^\intercal W \vec{R}.$$

Perturbing $\vec{x}$ by some amount, $\vec{\delta x}$, and minimizing $\chi^2(\vec{x})$ over $\vec{\delta x}$ yields

$$(A^\intercal W A)\vec{\delta x} = A^\intercal W \vec{R},$$

where

$$A = \frac{\partial \vec{R}}{\partial \vec{x}}.$$

Thus, changing one's parameter vector by

$$\vec{\delta x} = (A^\intercal W A)^{-1} A^\intercal W \vec{R} \tag{1.1}$$

yields a decrease in $\chi^2(\vec{x})$. For non-linear systems, this process is repeated multiple times until the change in χ^2 from one iteration to the next has passed below a fiducial fraction. Equation 1.1 is also known as the weighted normal equation.

A major issue with NEM is the computation of the inverse of the matrix $A^\intercal WA$. This matrix has n^2 elements and thus can be quite large for a model with many parameters. In addition, numerical stability can be a serious issue – $A^\intercal WA$ may be ill-conditioned, and thus taking the inverse can result in numerical errors (see Appendix).

One way to quantify the issue of numerical stability is by using the condition number $\kappa(M)$, where $\kappa(M) \equiv ||M|| * ||M^{-1}||$. A smaller $\kappa(M)$ corresponds to a better conditioned matrix M, meaning that fewer errors will accrue in the calculation of M^{-1}.

Since

$$\kappa(A^\intercal WA) \propto \kappa(A)^2$$

and

$$\kappa(A) > 1$$

for non-orthogonal matrix A, the classical NEM increases the risk of numerical instabilities

Finally, for problems involving a very large number of observations and model parameters, even the calculation of $(A^\intercal WA)$ is non-trivial, as this matrix multiplication scales like m^2n. The number of observations needed for an asteroid shape reconstruction typically number in the millions, with potentially $10^2 - 10^5$ free parameters.

1.3.1 Square Root Information Filter

The Square Root Information Filter (SRIF) was originally developed by Bierman in 1977 (Bierman (1977), Lawson & Hanson (1995)). The algorithm minimizes χ^2 for time series data with Gaussian errors, and is inspired by the Kalman filter algorithm. SRIF is more stable, more accurate, and faster than the algorithm currently used in `shape` . SRIF is also more numerically stable (and, in some cases

faster) than a solution via normal equations. Our implementation of SRIF includes some changes to the original algorithm, which will be discussed in section 1.4.

SRIF gets around all the problems described above by utilizing matrix square roots and Householder operations (see Bierman (1977), pg. 59) to increase the numerical stability when determining $\delta\vec{x}$. Instead of minimizing χ^2, SRIF minimizes

$$Q = (\chi^2)^{\frac{1}{2}} = ||W^{\frac{1}{2}}\vec{R}||,$$

where $W^{\frac{1}{2}}$ is the square root of the matrix W, defined such that

$$W = W^{\frac{1}{2}}W^{\frac{1}{2}}.$$

In general, the square root of a matrix is multivalued, however since W is positive-semidefinite, all square roots are real. We select the positive root by convention.

Then, along similar lines as NEM, a change of $\vec{\delta x}$ is introduced to the parameter vector $\vec{x}$, and $Q' = Q(\vec{x} + \vec{\delta x})$ is minimized over this change.

Q' is smallest when

$$||W^{\frac{1}{2}}\vec{R}(\vec{x} + \vec{\delta x})|| \approx ||W^{\frac{1}{2}}(\vec{R}(\vec{x}) + A\vec{\delta x})||$$

$$= ||W^{\frac{1}{2}}\vec{R}(\vec{x}) + W^{\frac{1}{2}}A\vec{\delta x}||$$

is minimized.

A matrix H is defined such that $HW^{\frac{1}{2}}A$ is upper triangular. H is orthogonal and can be generated by the product of n Householder operation matrices. Note that the orthogonality of H guarantees that

$$||W^{\frac{1}{2}}\vec{R}(\vec{x}) + W^{\frac{1}{2}}A\vec{\delta x}|| = ||H(W^{\frac{1}{2}}\vec{R}(\vec{x}) + W^{\frac{1}{2}}A\vec{\delta x})||$$

$$= ||HW^{\frac{1}{2}}\vec{R}(\vec{x}) + HW^{\frac{1}{2}}A\vec{\delta x}||.$$

From the definition of H, $HW^{\frac{1}{2}}A$ can be rewritten as

$$HW^{\frac{1}{2}}A = \begin{pmatrix} A' \\ Z \end{pmatrix},$$

where A' is an $n \times n$ upper-triangular matrix, and Z is the $(m-n) \times n$ zero-matrix. Then, rewriting

$$HW^{\frac{1}{2}}\vec{R}(\vec{x}) = \begin{pmatrix} \vec{R'_x} \\ \vec{R'_z} \end{pmatrix},$$

where R'_x and R'_z are $m \times 1$ and $(n-m) \times 1$ arrays, respectively, yields

$$Q' = \left\| \begin{pmatrix} \vec{R'_x} + A'\vec{\delta x} \\ \vec{R'_z} + Z\vec{\delta x} \end{pmatrix} \right\| = \left\| \begin{pmatrix} \vec{R'_x} + A'\vec{\delta x} \\ \vec{R'_z} \end{pmatrix} \right\|.$$

This is clearly minimized over δx when

$$\vec{R'_x} = -A'\vec{\delta x}$$

or

$$\vec{\delta x} = -A'^{-1}\vec{R'_x}. \tag{1.2}$$

Since A' is upper triangular, its inverse can be easily calculated, and singularity can be trivially detected. Furthermore, the condition number of the inverted matrix is proportional to $\kappa(A)$, as opposed to $\kappa(A)^2$ in the NEM case.

Finally, note that $A^\intercal WA$ is never calculated, which, as mentioned in section 1.3, is a computationally intensive calculation.

1.4 Additions to SRIF

1.4.1 Optimizations

The number of operations necessary to generate the Householder matrix H grows as $\mathrm{O}(n^2(m-n))$, where the number of observations m always exceeds the number of parameters n. Although this growth profile is favorable with respect to m when compared to that of NEM ($\mathrm{O}(m^2n)$), it becomes problematic for high resolution models (large n). To maintain good performance in large n situations, we have implemented three main optimizations to the standard SRIF.

Our first addition is to run the matrix triangularization simultaneously on multiple cores, which results in a significant speed-up. Note that although Householder matrices are generated iteratively, any given iteration k requires $n - k$ column-wise operations, and each of these operations are independent from each-other. Therefore, the Householder matrix calculations can be done in a thread-safe manner.

The second addition we made to the standard SRIF is the inclusion of a secondary χ^2 minimization for the scaling of $\vec{\delta x}$, so that

$$Q' = Q(\vec{x} + \alpha\vec{\delta x})$$

is minimized over α. This minimization is done with an eleven point grid search for α, from $\alpha = 10^{-3}$ to $\alpha = 10^{3.5}$. The additional minimization adds a trivial additional computation cost to the overall minimization of χ^2, but allows for faster convergence, and the possibility of skipping over local minima in the χ^2-space.

The final change we made to the underlying SRIF algorithm also granted the largest speed improvement. Even with the optimizations described above, the $\mathrm{O}(n^2(m-n))$ nature of the triangularization algorithm scales the computational cost drastically with increased model complexity. Furthermore, the need to store a derivative matrix for each iteration results in sizeable memory overhead when working with large datasets. To mitigate this problem, we modified the SRIF algorithm to select a subset of the nominal free parameters during each parameter vector adjustment, and to only fit for that subset. We tried a variety of subset selection methods, and concluded after testing that a "semi-random" mode was the most effective. During each parameter vector adjustment, this mode randomly selects a fixed number, b, of parameters from the nominal set of parameters $\{x_s\}$ for which the condition

$$k_s \leq \lfloor i * \frac{b}{n} \rfloor$$

is satisfied, where k_s is the total number of times parameter x_s has been considered

over the course of the entire fit, i is the total number of times that the parameter vector has been adjusted, n is the total number of nominal free parameters, and $\lfloor\ \rfloor$ is the round down operator.

When fitting for both shape and spin state simultaneously (Section 1.5.3), the spin axis orientation parameters were always included in the fit at each parameter vector adjustment step.

1.4.2 Penalty functions

The SPF routine can currently fit models to data while taking into account a suite of "penalty functions" that favor models with desirable properties. In a way, these penalty functions serve to make the fit operate in a more global context – there may be a local minimum in χ^2-space towards which the fitting algorithm would want to tend, but that minimum can be ruled out *a priori* thanks to physical considerations. These penalty functions include limits on ellipsoid axis ratios to avoid absurdly elongated or flattened shapes, constraints on shape concavities to avoid unrealistic surface topographies, and limits on the model center of mass distance from the image center, to name a few. We have implemented these penalty functions in the SRIF framework by redefining the residual vector as

$$\vec{R}'' = \begin{pmatrix} \vec{z} - \vec{f}(\vec{x}) \\ \vec{p_w} \end{pmatrix},$$

where

$$\vec{p_w} = \begin{pmatrix} p_1 \times w_1 \\ \vdots \\ p_N \times w_N \end{pmatrix}$$

for which $\{p_i\}$, $\{w_i\}$ are the set of penalty functions and penalty weights, respectively, and

$$A'' = \frac{\partial \vec{R}''}{\partial \vec{x}}.$$

The algorithm then progresses as described in section 1.3.1, with $\vec{R}''$ replacing $\vec{R}$ and A'' replacing A'.

1.5 Results

We tested our implementation with three different types of data. First, we generated simple spherical harmonic shapes and simulated images with Gaussian noise. Second, we used existing shape models of asteroids and simulated images with χ^2-distributed errors, the appropriate model for radar noise. Third, we used an actual asteroid radar data set. In all cases, we fit the images to recover the shapes using SRIF, SPF, and a third-party Levenberg-Marquardt algorithm (LM), a standard optimizing algorithm which is used across a wide variety of fields and applications (Press et al., 1992). Except where otherwise noted, our tests did not involve adjustments to parameters controlling the radar scattering law, ephemeris corrections, or spin axis orientation.

1.5.1 Simulated data with artificial shapes

These tests consisted of generating an initial basic shape (either spherical, oblate ellipsoid, or prolate ellipsoid), and randomly perturbing the spherical harmonic representation of this shape to get a new, non-trivial object.

Simulated range-Doppler images of this object were generated, and these images were fit for using the three aforementioned algorithms. This test serves as a good absolute test of a fitting method, because a solution is guaranteed to exist within the framework used (namely, a spherical harmonic representation). Figure 1.2 shows an example of the resulting shape when starting with a prolate ellipsoid. Three randomly generated objects were created for each of the three basic shapes, for a total of nine test cases.

a) 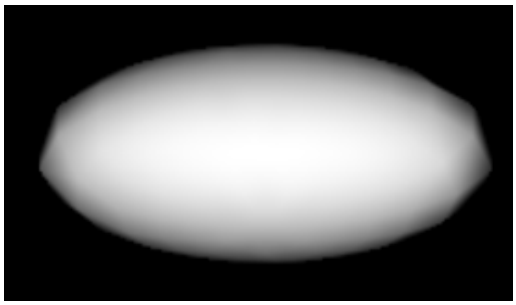 b) 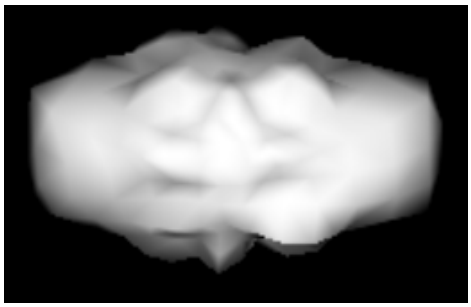

Figure 1.2: Example of artifical shape used as a test object to be fitted for. a) The initial shape, a prolate ellipsoid, before any of the spherical harmonic parameters have been changed. b) A perturbed prolate ellipsoid.

For each test case, we then generated between 20 and 30 simulated radar images and added Gaussian noise such that pixel values on the target exceed the root-mean-square (rms) deviations of the noise by an average factor of ~ 5 and a peak factor of ~ 150. These images were used to attempt to reconstruct the perturbed shape, with the original basic shape (sphere, prolate ellipsoid, or oblate ellipsoid) given as the initial condition. This process was repeated for each of the nine test cases.

The three fitting algorithms shared the same starting conditions for each test. For each fit, the models comprised 121 free parameters (corresponding to the coefficients of a ten-degree spherical harmonic representation), and the simulated images contained a total of 2.4 million data points. Stopping criteria were also normalized for the three different test types – a fit was considered finished if the χ^2 statistic had not changed to within three significant digits after one hour, or twelve hours had passed since the fit began, whichever occurred first. Time-based stopping criteria – as opposed to iteration-based – were chosen in order to account for fundamental differences between the algorithms with respect to the definition of a single iteration. In addition, fits were allowed to run past the criteria stopping point, and the criteria were analyzed and applied afterwards. This was to avoid missing a drop-off in χ^2 in one test type that might not appear in another. All

times are wall clock time.

The results of these tests (Figure A.1) indicate that SRIF consistently performs better than the currently-used SPF algorithm. In addition, SRIF appears to ultimately converge on a lower chi-squared than LM in all cases.

SRIF also converged on a reduced chi-squared (χ^2_{red}) of less than 1.3 (indicating a reasonable approximation of the correct model parameters had been found) in eight out of the nine tests, while SPF was only able to do so in one out of the nine tests.

1.5.2 Simulated data with existing asteroid shape models

We conducted another set of tests using existing shape models of asteroids. Three cases were tested - Itokawa, the 1999 KW4 primary, and 2000 ET70 (Figure A.2). As opposed to the previous set of tests, these shapes are not guaranteed to be well approximated with a spherical harmonic representation. However, a best-fit spherical harmonic representation can still be found.

For this set of images we used χ^2-distributed errors, which is the correct noise model for individual images of radar echo power. We chose a noise model such that the pixel values on the target exceed the rms deviations of the noise by an average factor of ~ 2 and a peak factor of ~ 60. When multiple images are summed, one can often rely on the fact that errors approach normality by the central limit theorem, hence the choice of Gaussian noise for the images tested in section 1.5.1.

The results of these tests are illustrated in Figure A.3, and an example comparison of a fit synthetic image to the simulated image is shown in Figure A.4. Our implementation of SRIF clearly performs faster and with higher accuracy than both SPF and LM.

1.5.3 Spin state

Jointly solving for spin state and shape is typically challenging and time-consuming with the traditional implementation of `shape` . A common approach is to estimate the spin state as best as possible with rudimentary shapes (e.g., ellipsoids or low-order spherical harmonic models) in a basic grid search. One can then use the most favorable trial values of the spin state to fit a model for the physical shape to the observed radar images. Experience with traditional `shape` indicates that the algorithm rarely deviates much from the initial conditions given on the spin state, probably as a result of the one-parameter-at-a-time fitting approach.

Our tests indicate that SRIF is capable of fitting a reasonable asteroid shape, even when the initial shape and spin state parameters are far away from their optimal values. This advantage likely results from the joint estimation of shape and spin parameters.

For example, Figure A.5 shows the best-fit spherical harmonics shape, as determined by SRIF, for a set of simulated images of the asteroid Itokawa. The initial conditions for the shape parameters were a sphere with a radius 10% larger than the longest axis of the actual shape model. In addition, the initial spin axis was 30 degrees off from the spin axis with which the data were simulated. We repeated these experiments with a variety of starting conditions, as well as several different shape models, with similar results.

SRIF's capacity to fit for both shape and spin state parameters can drastically cut down on the total time required to obtain an accurate asteroid shape model.

1.5.4 Real data: 2000 ET70

We have run `shape` with all three fitting algorithms on actual radar images of the asteroid 2000 ET70 (Naidu et al., 2013). `shape` was run initially with an ellipsoid model. The starting conditions for this model were such that the ellipsoid axes

Table 1.1: Run statistics for SPF and SRIF fits for 2000 ET70 data.

Model	$\chi^2_{initial}$	χ^2_{final}			Runtime (hours)		
		SPF	LM	SRIF	SPF	LM	SRIF
2000 ET70: Ellipsoid	3.70	2.80	2.70	2.40	0.02	0.84	0.13
2000 ET70: Sph. Harm.	2.40	2.10	2.37	2.10	2.98	0.17	1.36

were all equal. The best fit ellipsoid model ($a/b = 1.16, b/c = 1.13$) was then converted into a spherical harmonic model with 122 model components (corresponding to the coefficients of a ten-degree spherical harmonic representation, as well as one overall size scaling factor), which was then fit again to the data. This process resulted in a final spherical harmonic model (Figure A.6) for the asteroid with a χ^2_{red} of 2.1. The stopping criterion was a reduction in χ^2_{red} less than 0.01 between two consecutive iterations.

For the first stage, SRIF fit a substantially better ellipsoid than SPF did, although it took about eight minutes longer (Table 1.1). For the second stage, SRIF converged on a final solution more than two times faster than SPF. This further corroborates the results obtained from our tests with simulated data.

1.6 Future changes

The addition of SRIF to `shape` has improved fitting performance, but additional changes can still be made to allow `shape` to function optimally with real-world data.

1.6.1 Global vs local variable partitioning

The fits discussed in this paper were performed on global parameters only – namely, parameters that are valid across all data sets associated with the object

in question. When performing a high-fidelity fit on multiple data sets, however, it is necessary to take into account local parameters as well. These are model arguments which apply only at specific points in time. For example, while the mean radius and rotation rate of an asteroid is a global parameter, the system temperature and ephemeris correction parameters on the third day of observations are local to the data taken on the third day of observations.

Processing local parameters is less computationally intensive than processing global parameters. The gradients of any observables not within a local parameter's timeframe are known *a priori* to be zero. This greatly reduces the number of modelling function calls that must be made when considering local parameters. In addition, the triangularization of a derivative matrix scales with the number of non-zero elements. This means that while the total number of additional parameters scales like the product of the number of datasets with the average number of local parameters per dataset, the additional computation time only scales with the average number of local parameters per data set. Because of this, adding the capacity for processing local parameters will only increase runtime by $\sim$20%. We plan on adding this functionality in a future version of `shape` .

1.6.2 Additional fitting methods

Tests that we have run with the simulated and real data have indicated that the χ^2-space for shape-models is not smooth. Figure A.7 shows a two-dimensional slice of the χ^2-space for a spherical harmonic model against 2000 ET70 data. The multi-valleyed nature of this space makes it difficult for local fitting methods to find the global minimum. In light of this, global fitting mechanisms such as simulated annealing or Markov Chain Monte Carlo may be better suited for this problem. These methods can be supplemented by a gradient descent method like SRIF. In fact, utilizing a hybrid of these methods may prove to be the optimal solution for this class of problem. Until such methods are implemented, convergence on

a global minimum will be dependent on a good choice of starting conditions. This often forces shape modelers to explore a variety of initial conditions, and identifying such starting conditions is not always practical.

1.6.3 Additional shape representations

There are serious drawbacks to using spherical harmonics to represent the radius of an object at each latitude-longitude grid point. Many asteroid shapes are poorly approximated by this representation (e.g., the 1999 KW4 primary) and there are entire classes of shapes (e.g., banana) that can not be described at all in this fashion. Traditionally, this problem has been solved by the use of vertex models, but these shape representations typically involve a large number of parameters (i.e., the coordinates of three vertices per facet). We are currently looking into new representation methods, some of which may allow for a greater range of shapes, while at the same time cutting down on the number of free parameters.

1.7 Conclusions

We have added new optimization procedures into the asteroid shape modeling software `shape` , enabling the use of a Levenberg-Marquardt algorithm or a Square Root Information Filter. We implemented several optimizations to the SRIF algorithm to increase performance in shape inversion problems. Tests on both simulated and actual data indicate that our additions allow shape inversion to proceed more quickly and with better fidelity than was previously possible. The SRIF implementation also facilitates simultaneous fits of the spin axis orientation and shape.

CHAPTER 2

Yarkovsky Drift Detections for 159 Near-Earth Asteroids

2.1 Introduction

The Yarkovsky effect is a small force that results from the anisotropic thermal emission of small celestial bodies. Over the past decade, there has been increasing awareness that the Yarkovsky effect plays an important role in the evolution of asteroid orbits and the delivery of meteorites to Earth (Bottke et al., 2006). Several authors have published Yarkovsky effect detections for dozens of asteroids: Chesley et al. (2008, 12 detections), Nugent et al. (2012, 54 detections), Farnocchia et al. (2013b, 47 detections, of which 21 are deemed reliable).

Here, we provide the largest collection of Yarkovsky detections to date and introduce several improvements to previous studies. Nugent et al. (2012) and Farnocchia et al. (2013b) relied on the debiasing of star catalogs proposed by Chesley et al. (2010). Our current model uses the more up-to-date and accurate debiasing algorithm of Farnocchia et al. (2015). Previous works have traditionally relied on a signal-to-noise (S/N) metric and the quantity and quality of the observational data to distinguish between detections and non-detections (Chesley et al., 2008; Farnocchia et al., 2013b), or by augmenting these criteria with an explicit sensitivity metric (Nugent et al., 2012). Here, we further refine the detection criterion with a precise formulation based on an analysis of variance (Greenberg et al., 2017). Some of the previous formulations (e.g., Nugent et al., 2012) included a

finite increment in semi-major axis at each time step irrespective of the asteroid's distance from the Sun. Here, we use a $1/r^2$ dependence of the solar flux. The Nugent et al. (2012) results were based on astrometry obtained as of January 31, 2012. The current work benefits from more than 5 years of additional astrometry, including more than 100 additional ranging observations with the Arecibo and Goldstone radars. Finally, the numbers of known NEAs and numbered NEAs have both nearly doubled since the Nugent et al. (2012) study. The number of detections is now sufficiently large that ensemble properties can be refined, such as the ratio of retrograde to prograde rotators, and the physical theory can be tested, such as the dependence of the Yarkovsky drift magnitude as a function of asteroid size.

2.2 Data preparation

Optical astrometry was automatically downloaded from the Minor Planet Center (MPC) on Mar 8, 2017 (Minor Planet Center, 2017). Astrometry taken from non-stationary (generally, space-based) observatories was discarded. Radar astrometry was downloaded from the JPL Radar Astrometry Database (JPL Solar System Dynamics, 2017a) and was discarded from MPC records to avoid duplication. In a few instances, previously unpublished radar data obtained by the authors were also used.

2.2.1 Weighting and debiasing

Optical astrometry was weighted following the methods described by Farnocchia et al. (2015). To summarize, this method involved weighting measurements based on the observatory, type of measurement, star catalog, and date. We also used the "batched weighting" scheme described by Farnocchia et al. (2015), wherein measurements taken from the same observatory on the same night were given

a smaller weight. Star catalog debiasing was also performed according to the approach of Farnocchia et al. (2015).

Radar astrometry was weighted according to observer-reported uncertainties.

2.2.2 Outlier rejection

Outlier rejection was performed via an iterative fit-drop-add scheme. All available data were used during the initial gravity-only orbital fit. Then all optical measurements with weighted residuals beyond a fiducial threshold were rejected. Radar data were excluded from outlier rejection. This threshold was defined as

$$\frac{(O_{i,RA} - C_{i,RA})^2}{\sigma_{i,RA}^2} + \frac{(O_{i,DEC} - C_{i,DEC})^2}{\sigma_{i,DEC}^2} < 8, \tag{2.1}$$

where O and C stand for observed and computed values, respectively, RA and DEC stand for right ascension and declination, respectively, σ represent observational uncertainty, and the index i represents the i^{th} observation.

As the fit iterated, previously discarded measurements were re-evaluated with respect to this threshold, and included in subsequent iterations, as appropriate. Outlier rejection was disabled after three fit-drop-add iterations gave identical results.

Initially, outlier rejection was performed with a gravity-only model. After the Yarkovsky component of the dynamical model was estimated, outlier rejection was performed once more with the additional Yarkovsky component included (Section 2.4).

2.3 Orbit determination

Orbit determination was performed using our Integration and Determination of Orbits System (IDOS, see Greenberg et al. (2017)). At its core, this software utilizes the Mission analysis, Operations, and Navigation Toolkit Environment

(MONTE), a set of tools developed by the Jet Propulsion Laboratory (JPL) for a variety of space-related science and aeronautical goals (Evans et al., 2016). The MONTE orbital integrator can account for gravitational perturbations from any set of masses – for the analyses performed in this paper, we considered the eight known planets and 24 of the most massive minor planets (Folkner et al., 2014) as gravitational perturbers. During close Earth approaches, the integrator considers a detailed model of the planetary gravitational field. MONTE also accounts for general relativistic effects during orbital integration. Further details concerning the internal operations of IDOS were described by Greenberg et al. (2017).

In gravity-only solutions, we estimated the six parameters (three position and three velocity components) of the state vector simultaneously. In Yarkovsky solutions, we estimated an additional parameter describing the strength of the Yarkovsky drift. We assigned one-standard-deviation uncertainties (σ) to our Yarkovsky estimates such that a 1-σ change to the drift rate results in an increase of one in the sum of squares of weighted residuals, similar to the approach of Nugent et al. (2012). This approach yields values that match the formal uncertainties derived from a covariance matrix, which was the approach of Farnocchia et al. (2013b).

2.4 Yarkovsky force model

We utilized the Yarkovsky force model described by Greenberg et al. (2017), where the magnitude and direction of the thermal acceleration, $\ddot{r}$, is calculated and applied at every integration time step of the dynamical model. The acceleration is calculated as

$$\ddot{\vec{r}} = \zeta \, \frac{3}{8\pi} \, \frac{1}{D\rho} \, \frac{L_\odot}{c} \, \frac{X_{\hat{p}}(\phi)\vec{r}(t)}{||\vec{r}(t)||^3}, \tag{2.2}$$

where $\vec{r}(t)$ is the heliocentric radial vector for the object at time t, $\hat{p}$ is the unit spin-axis vector , ϕ is the phase lag, $L_\odot$ is the luminosity of the Sun, c is the speed

of light, and $X_{\hat{p}}(\phi)$ is the rotation matrix about p. D and ρ are the diameter and density of the object, respectively, while ζ is an efficiency factor. The phase lag ϕ describes the longitude on the surface from which photons are re-emitted, relative to the sub-Solar longitude. In Equation 2.2, we assume a perfect absorber, i.e., a Bond albedo of zero.

For the objects analyzed in this work, specific values for ϕ and $\hat{p}$ were not known. Therefore, these values were fixed at $-90°$ and parallel to the orbit normal vector, respectively , which maximizes the magnitude of the orbital perturbation. As we discuss in the next paragraph, these assumptions do not affect the estimated value of the semi-major axis drift.

With knowledge of the orbit semi-major axis, a, and eccentricity, e, the orbit-averaged drift in semi-major axis, $\langle da/dt \rangle$, can be determined from this acceleration model with

$$\langle da/dt \rangle = \pm \, \xi \frac{3}{4\pi} \frac{1}{\sqrt{a}} \frac{1}{1-e^2} \frac{L_\odot}{c\sqrt{GM_\odot}} \frac{1}{D\rho}, \tag{2.3}$$

which is equivalent to Greenberg et al. (2017)'s equation (8) and corrects Nugent et al. (2012)'s equation (1). Here, ξ is the Yarkovsky efficiency, and depends on ζ, spin pole obliquity γ (i.e., the angle between the spin pole vector $\hat{p}$ and the orbit normal vector), and phase lag ϕ. We always take the Yarkovsky efficiency to be positive. Any incorrect assumption about Bond albedo, diameter, obliquity, and phase lag are absorbed in this efficiency factor such that the $\langle da/dt \rangle$ value, which is dictated by the astrometry, is not affected by these assumptions (Section 2.14.3).

With numerical values, we find

$$\begin{aligned} \langle da/dt \rangle = \pm 1.45 \left(\frac{\xi}{0.01} \right) \left(\frac{1 \text{ au}}{a} \right)^{\frac{1}{2}} \left(\frac{1}{1-e^2} \right) \times \\ \left(\frac{1 \text{ km}}{D} \right) \left(\frac{1000 \text{ kg m}^{-3}}{\rho} \right) \times \frac{10^{-4} \text{ au}}{\text{My}}. \end{aligned} \tag{2.4}$$

2.5 Candidate selection

2.5.1 Initial selection

We considered three sets of Yarkovsky detection candidates. Two sets of candidates, the `Nugent12` set and the `Farnocchia13` set, represent Yarkovsky detections reported by Nugent et al. (2012) and Farnocchia et al. (2013b), respectively. For these objects, we performed our analysis in two ways – first, by using the same observational data as that used by the authors, and second, by using all currently available data (Section 2.5.2). The `Nugent12` set features 54 objects, while the `Farnocchia13` set contains 47 objects.

The third data set, `UCLA17`, contains objects that had not previously been considered by the other two works but that we determined to be Yarkovsky detection candidates. For the most part, these objects had either not yet been discovered, or had small observation intervals prior to 2012 or 2014. We identified the new candidates as follows. First, we downloaded the list of 15,595 known NEAs from the MPC on March 7, 2017. Second, for each one of the 2,348 numbered NEAs, we computed the Yarkovsky sensitivity metric (S_Y) described by Nugent et al. (2012). This root-mean-square quantity provides an excellent assessment of the relative sensitivity of selected data sets to drifts in semimajor axis. We used the threshold determined by Nugent et al. (2012) of $S_Y > 2$. Only 376 NEAs met this condition. Third, we computed preliminary estimates of $\langle da/dt \rangle$ and associated uncertainties for these 376 NEAs. We defined a signal-to-noise (S/N) metric as the ratio of the best-fit $\langle da/dt \rangle$ to its one-standard-deviation uncertainty. We selected the 200 NEAs that have both $S_Y > 2$ and S/N > 1. Of these, 59 had been previously considered by Nugent et al. (2012) or Farnocchia et al. (2013b).

Nugent et al. (2012) rejected Yarkovsky detections for which there were fewer than 100 astrometric measurements, or for which the observation interval was less than 15 years. However, we reviewed the detections that were discarded due to

these criteria in 2012 and found that 90% of them were reliable, i.e., their $\langle da/dt \rangle$ values are consistent with values presented in this work, even after the addition of post-2012 data. In this work, we flag objects that Nugent et al. (2012) would have discarded because of data span or quantity, but we do not discard the detections.

Among the three sets of objects (`Nugent12`, `Farnocchia13`, and `UCLA17`), there are 231 distinct Yarkovsky candidates.

2.5.2 Selection refinement

After candidate selection, we performed a six-parameter fit to the astrometry using a gravity-only model, followed by a seven-parameter fit which included a Yarkovsky force model. We then performed an *analysis of variance* (Mandel, 1964) to determine whether the data warrants the use of the Yarkovsky model.

Specifically, we calculated the test-statistic

$$F = \frac{\kappa_\delta}{\kappa_Y} \tag{2.5}$$

where

$$\kappa_\delta = \frac{\sum_{i=0}^{N} (\frac{O_i - C_{0,i}}{\sigma_i})^2 - \sum_{i=0}^{N} (\frac{O_i - C_{Y,i}}{\sigma_i})^2}{m_Y - m_0} \tag{2.6}$$

and

$$\kappa_Y = \frac{\sum_{i=0}^{N} (\frac{O_i - C_{Y,i}}{\sigma_i})^2}{N - m_Y}. \tag{2.7}$$

Here, $C_{0,i}$ is the i^{th} computed value assuming gravity only, $C_{Y,i}$ is the i^{th} computed value assuming our best-fit Yarkovsky model, O_i is the i^{th} observation and σ_i is the measurement uncertainty for that observation, N is the number of observations, and m_Y, m_0 are the number of free parameters in the Yarkovsky model ($m_Y = 7$) and gravity-only model ($m_0 = 6$), respectively.

We then calculated the value

$$p = \int_{x=F}^{x=\infty} f(m_Y - m_0, N - m_Y, x) dx, \tag{2.8}$$

where $f(m_Y - m_0, N - m_Y, x)$ is the F-distribution probability density function with $m_Y - m_0$ and $N - m_Y$ degrees of freedom. The p-value serves as a metric for testing the null hypothesis — namely, that the additional degree of freedom introduced by the Yarkovsky force model is superfluous.

Our initial selection refinement step consisted of discarding those objects for which $p > 0.05$, which approximately corresponds to a 2-standard-deviation detection threshold. This step rejected 60 objects, leaving 171 objects for further consideration.

We also followed the procedure of Nugent et al. (2012), and determined those objects for which there were fewer than 10 measurements in the first 10 years of observations. This check is necessary because isolated, erroneous astrometry can result in spurious detections. For these objects, we re-fit the Yarkovsky model with the sparse observations removed, and rejected any objects for which the resulting $\langle da/dt \rangle$ value changed significantly from that of the nominal fit. This step rejected 12 objects, leaving 159 objects remaining. These 159 asteroids make up our final set of Yarkovsky detections (Table 2.1).

Finally, because pre-CCD astrometry can lead to spurious detections (Section 2.13.7) even with proper weights, we re-analyzed 27 Yarkovsky candidates for which pre-1965 astrometry exists. Specifically, we discarded the pre-1965 astrometry, fit for $\langle da/dt \rangle$ values with the shortened observation intervals, and recomputed p-values. Objects that no longer met the $p \leq 0.05$ criterion were flagged. About a dozen objects are in this category and their Yarkovsky rates require additional verification.

2.6 Comparison with previous works

Many of the objects considered for this work had been previously reported as Yarkovsky detections (Section 2.5). It is useful to compare our Yarkovsky deter-

minations to these previous works, for two reasons. First, because our results were determined independently of the previous works, a comparison serves as a check on both sets of results. Second, new astrometry has been reported for many of these objects. Therefore, we can study how the results and uncertainties changed in light of new data.

We performed two comparisons with the previous works. In each case, we compared both our absolute Yarkovsky measurements and their associated uncertainties to those of the original works. We first created data sets that roughly matched the observational intervals reported by previous authors, to the nearest calendar year. In doing so, we expect there to be good agreement between our Yarkovsky detections and those of the original works. We do anticipate slight differences introduced by our use of improved debiasing and weighting algorithms (Section 2.2.1) and by our use of observation sets that are not identical to those used in the original works (e.g., observations at beginning or end of intervals matched to the nearest calendar year, precovery observations, or observations that were re-measured). For our second comparison, we included all available data for all objects. In this case, we expect an overall lower level of agreement because of our use of additional astrometry, which sometimes represent a significant fraction of the available astrometry.

Because we are interested in whether our results match those previously published, it is useful to quantify what we mean by a "match". We used a metric inspired by mean-comparison tests. Namely, for each object i in the dataset, we calculated

$$z_i = \frac{|Y_{t,i} - Y_{p,i}|}{\sqrt{\sigma_{t,i}^2 + \sigma_{p,i}^2}}, \tag{2.9}$$

where $Y_{t,i}, Y_{p,i}$ are this work's estimated drift rate for object i and the previous work's estimated drift rate for object i, respectively, and $\sigma_{t,i}, \sigma_{p,i}$ are this work's uncertainty for object i and the previous work's uncertainty for object i, respec-

tively. The quantity z therefore represents a significance score. By choosing a threshold value for z, we can signal our confidence that our measurement is consistent with that of the original work. We chose a significance threshold of 2.0, i.e., detection i was considered a match if

$$z_i < 2.0. \tag{2.10}$$

In other words, we concluded that the two measurements matched if we could not reject the hypothesis that the two measurements were drawn from the same distribution at the 95% confidence level.

2.7 Yarkovsky drift rates

We measured semi-major axis drift rates and calculated Yarkovsky efficiency values for 159 NEAs, shown in Table 2.1 and ordered by object number. We present drift rates derived from optical measurements, as well as optical plus radar astrometry. An online, machine-readable file containing the data in this table can be found at `http://escholarship.org/uc/item/0pj991hd`.

Table 2.1: Yarkovsky drift measurements for 159 Near-Earth Asteroids. The semi-major axis, a, is in au. e is orbital eccentricity. Asteroid diameter D is in km. Diameters inferred from H-magnitude via Equation 2.14 are flagged with a *. N_o, N_r are the number of optical measurements and radar measurements, respectively. $\langle da/dt \rangle$, σ, the semi-major axis drift and associated uncertainty, are in au/My. For objects with radar astrometry ($N_r > 0$), we also report $\langle da/dt \rangle_r$ and σ_r, which incorporate those radar measurements. p and p_r are the p-values used in distinguishing between a gravity-only dynamical model and a Yarkovsky dynamical model using optical data only and optical plus radar data, respectively. s_Y is the Yarkovsky sensitivity parameter of Nugent et al. (2012). ξ indicates the Yarkovsky efficiency, which was computed with a bulk density that was inferred from the spectral type, if available (Section 2.10). Yarkovsky detections determined to be weaker because of the time span or quantity of astrometry (Section 2.5.1) are flagged with †, whereas objects with anomalously high ξ values ($\xi > 0.5$) are flagged with §. Objects which yield a drift rate detection with pre-1965 data but not without it (Section 2.5.2) are flagged with $^{\mathrm{C}}$.

Name	a	e	D	N_o	N_r	$\langle da/dt \rangle$	σ	p	$\langle da/dt \rangle_r$	σ_r	p_r	s_Y	ξ	Arc
(433) Eros$^{\mathrm{C}}$	1.46	0.22	16.84	7951	2	-0.58	0.2	1e-15	-0.58	0.2	1e-15	67.4	0.21	1900 – 2017
(719) Albert$^{\mathrm{C}}$	2.64	0.55	*2.82	1144	0	-5.73	5.1	5e-03	–	–	–	4.6	0.34	1911 – 2017
(1036) Ganymed§	2.66	0.53	37.67	5087	1	-5.02	1.3	1e-16	-5.02	1.3	1e-16	7.0	4.12	1924 – 2017
(1566) Icarus	1.08	0.83	1.00	1221	23	-4.61	0.5	1e-16	-4.45	0.5	1e-16	36.8	0.02	1950 – 2015
(1685) Toro	1.37	0.44	3.40	2290	9	-1.45	0.4	3e-14	-1.55	0.4	1e-16	34.8	0.09	1948 – 2016
(1862) Apollo$^{\mathrm{C}}$	1.47	0.56	1.50	1548	17	-0.26	0.9	6e-01	-1.78	0.2	1e-16	30.7	0.04	1930 – 2017
(1864) Daedalus§	1.46	0.61	3.70	1713	1	-9.28	6.2	3e-03	-11.27	6.0	3e-04	3.1	0.59	1970 – 2017
(1915) Quetzalcoatl$^{\dagger\mathrm{C}}$	2.54	0.57	0.50	52	1	-42.38	23.0	3e-02	-45.19	22.7	2e-02	4.0	0.41	1952 – 2005
(2059) Baboquivari$^{\S\mathrm{C}}$	2.65	0.53	*2.24	416	0	16.14	8.5	1e-03	–	–	–	4.9	0.72	1963 – 2016
(2061) Anza$^{\S\mathrm{C}}$	2.27	0.54	2.60	345	0	13.23	7.5	3e-03	–	–	–	5.2	0.63	1960 – 2016

Table 2.1, continued.

Name	a	e	D	N_o	N_r	$\langle da/dt \rangle$	σ	p	$\langle da/dt \rangle_r$	σ_r	p_r	s_Y	ξ	Arc
(2062) Aten	0.97	0.18	1.10	905	7	-6.06	0.9	1e-16	-5.32	0.7	1e-16	24.9	0.10	1955 – 2017
(2063) Bacchus	1.08	0.35	*1.23	666	12	-6.96	2.1	2e-09	-6.22	1.9	1e-08	17.3	0.13	1977 – 2016
(2100) Ra-Shalom	0.83	0.44	2.30	1477	6	-3.71	1.0	1e-12	-2.25	0.8	1e-08	18.6	0.05	1975 – 2017
(2101) Adonis	1.87	0.76	0.60	116	5	-30.27	14.4	6e-03	-20.08	13.0	4e-02	4.6	0.12	1935 – 2013
(2102) Tantalus	1.29	0.30	1.65	671	0	-2.14	2.1	3e-02	–	–	–	12.1	0.06	1975 – 2017
(2340) Hathor	0.84	0.45	0.30	421	7	-16.92	0.8	1e-16	-17.30	0.7	1e-16	28.4	0.07	1976 – 2015
(3200) Phaethon	1.27	0.89	5.10	3693	1	-8.83	3.5	1e-07	-7.80	3.4	1e-06	3.4	0.15	1983 – 2017
(3361) Orpheus	1.21	0.32	0.30	647	0	6.28	1.6	1e-11	–	–	–	18.0	0.03	1982 – 2014
(3362) Khufu	0.99	0.47	0.70	271	0	-17.88	11.8	1e-02	–	–	–	2.9	0.16	1984 – 2005
(3551) Verenia	2.09	0.49	0.90	410	0	-14.12	9.9	3e-02	–	–	–	3.6	0.24	1983 – 2016
(3753) Cruithne	1.00	0.51	2.07	591	0	-8.06	4.2	2e-04	–	–	–	6.7	0.21	1973 – 2017
(3908) Nyx	1.93	0.46	1.00	1670	16	6.70	2.6	4e-07	7.20	1.6	1e-16	6.4	0.10	1980 – 2016
(4015) Wilson-H.[C]	2.64	0.63	4.00	897	0	-7.45	3.1	2e-04	–	–	–	10.7	0.50	1949 – 2016
(4034) Vishnu	1.06	0.44	0.42	488	1	-38.74	9.2	2e-16	-33.14	7.9	6e-16	4.9	0.20	1986 – 2015
(4179) Toutatis	2.54	0.63	5.40	5834	55	-14.50	3.7	1e-16	-2.67	0.5	1e-16	2.1	0.26	1933 – 2017

Table 2.1, continued.

Name	a	e	D	N_o	N_r	$\langle da/dt \rangle$	σ	p	$\langle da/dt \rangle_r$	σ_r	p_r	s_Y	ξ	Arc
(4197) Morpheus[§]	2.30	0.77	1.80	694	6	30.64	11.3	8e-07	29.16	11.1	2e-06	2.9	0.60	1954 – 2016
(4581) Asclepius	1.02	0.36	*0.26	202	4	-30.78	16.8	4e-04	-19.69	5.6	4e-11	2.9	0.08	1988 – 2016
(4660) Nereus	1.49	0.36	0.33	527	32	5.25	5.4	7e-02	8.61	3.9	4e-05	6.1	0.04	1981 – 2015
(4688) 1980 WF	2.24	0.51	0.60	215	0	-7.00	5.5	5e-02	–	–	–	9.6	0.06	1980 – 2011
(4769) Castalia	1.06	0.48	1.40	298	15	-5.10	3.0	8e-03	-6.14	2.8	8e-04	10.5	0.12	1989 – 2016
(5011) Ptah	1.64	0.50	*1.86	582	0	-14.77	6.5	6e-05	–	–	–	6.2	0.45	1960 – 2016
(5693) 1993 EA	1.27	0.59	*1.62	1310	0	-8.67	4.5	4e-04	–	–	–	2.9	0.18	1983 – 2017
(6037) 1988 EG	1.27	0.50	*0.65	407	8	-6.97	5.0	4e-03	-9.07	4.5	1e-04	9.3	0.08	1987 – 2016
(6239) Minos	1.15	0.41	*0.71	892	3	6.79	3.7	3e-04	7.98	3.5	1e-05	7.0	0.09	1982 – 2016
(6489) Golevka	2.49	0.61	0.53	980	40	-13.45	12.1	6e-02	-5.17	0.7	1e-16	1.8	0.05	1991 – 2016
(6611) 1993 VW	1.70	0.48	*1.48	1076	0	-5.06	4.2	4e-02	–	–	–	4.1	0.10	1982 – 2016
(7336) Saunders	2.31	0.48	*0.62	592	0	11.68	8.1	7e-03	–	–	–	3.5	0.16	1982 – 2011
(7341) 1991 VK	1.84	0.51	*1.62	1403	13	-4.41	3.5	7e-03	-2.44	0.8	3e-11	3.6	0.07	1981 – 2017
(7350) 1993 VA[C]	1.36	0.39	2.36	1185	0	-5.27	2.7	2e-04	–	–	–	4.6	0.21	1963 – 2016
(7822) 1991 CS	1.12	0.16	1.60	1151	4	8.03	5.6	4e-03	6.57	5.5	2e-02	3.7	0.20	1990 – 2016

Table 2.1, continued.

Name	a	e	D	N_o	N_r	$\langle da/dt \rangle$	σ	p	$\langle da/dt \rangle_r$	σ_r	p_r	s_Y	ξ	Arc
(10302) 1989 ML	1.27	0.14	*0.49	418	0	29.66	5.1	1e-16	–	–	–	6.7	0.20	1989 – 2016
(10563) Izhdubar	1.01	0.27	*1.55	541	0	18.94	7.9	1e-04	–	–	–	3.4	0.46	1991 – 2016
(11054) 1991 FA[C]	1.98	0.45	*1.41	1183	0	-1.23	1.1	1e-02	–	–	–	16.6	0.03	1937 – 2016
(11405) 1999 CV3[§]	1.46	0.39	*3.24	2130	0	9.79	5.8	7e-04	–	–	–	2.7	0.61	1978 – 2016
(13651) 1997 BR	1.34	0.31	0.56	824	2	-12.18	9.9	3e-02	-17.54	8.5	5e-04	2.4	0.19	1979 – 2017
(14402) 1991 DB	1.72	0.40	0.60	451	0	-8.57	5.5	2e-03	–	–	–	6.9	0.05	1990 – 2017
(29075) 1950 DA	1.70	0.51	2.00	521	12	-3.91	1.8	2e-05	-2.60	0.5	1e-16	13.7	0.09	1949 – 2016
(31221) 1998 BP26	1.72	0.26	*1.29	842	0	-17.85	6.1	7e-09	–	–	–	2.7	0.48	1997 – 2016
(33342) 1998 WT24	0.72	0.42	*0.93	1722	17	-10.46	9.2	1e-02	-16.32	2.5	1e-16	2.1	0.18	1998 – 2016
(37638) 1993 VB[†]	1.91	0.52	*0.49	99	0	38.32	32.9	5e-02	–	–	–	2.3	0.32	1993 – 2015
(37655) Illapa	1.48	0.75	*0.93	422	2	-11.72	3.6	4e-12	-10.86	3.4	7e-12	10.0	0.09	1994 – 2015
(41429) 2000 GE2	1.59	0.56	0.20	332	0	-31.28	14.9	1e-03	–	–	–	2.5	0.09	1997 – 2017
(53550) 2000 BF19	1.50	0.42	*0.56	212	0	-40.20	27.3	4e-02	–	–	–	2.5	0.39	1991 – 2016
(54509) YORP[†]	1.00	0.23	*0.10	548	5	-19.17	47.6	3e-01	-33.69	13.3	3e-09	0.7	0.06	2000 – 2005
(55408) 2001 TC2	1.10	0.22	0.46	136	0	-13.87	10.6	3e-02	–	–	–	6.7	0.11	1979 – 2017

Table 2.1, continued.

Name	a	e	D	N_o	N_r	$\langle da/dt \rangle$	σ	p	$\langle da/dt \rangle_r$	σ_r	p_r	s_Y	ξ	Arc
(65679) 1989 UQ	0.92	0.26	0.92	411	0	-18.51	5.8	5e-08	–	–	–	6.9	0.25	1954 – 2017
(65690) 1991 DG	1.43	0.36	*0.54	252	0	-32.34	13.2	5e-05	–	–	–	3.5	0.31	1990 – 2016
(65717) 1993 BX3	1.39	0.28	*0.25	100	0	28.55	21.3	1e-02	–	–	–	2.7	0.13	1992 – 2016
(65733) 1993 PC	1.15	0.47	*0.74	382	0	-18.75	9.9	2e-03	–	–	–	3.0	0.20	1992 – 2015
(66400) 1999 LT7	0.86	0.57	0.41	241	0	-40.12	8.2	1e-15	–	–	–	4.2	0.17	1987 – 2014
(67399) 2000 PJ6[C]	1.30	0.35	*0.81	249	0	-12.47	8.2	2e-02	–	–	–	7.4	0.17	1951 – 2016
(85770) 1998 UP1	1.00	0.35	*0.28	494	0	-17.35	5.7	2e-07	–	–	–	5.2	0.07	1990 – 2017
(85953) 1999 FK21	0.74	0.70	0.59	946	0	-10.34	2.5	1e-13	–	–	–	4.4	0.05	1970 – 2016
(85990) 1999 JV6	1.01	0.31	0.45	1032	15	-11.83	4.0	3e-07	-14.14	1.0	1e-16	3.9	0.07	1999 – 2017
(99907) 1989 VA	0.73	0.59	1.40	571	0	11.69	3.8	1e-07	–	–	–	7.4	0.17	1989 – 2016
(101955) Bennu[†]	1.13	0.20	0.49	569	29	-12.41	7.8	6e-05	-19.03	0.1	1e-16	4.9	0.16	1999 – 2013
(136582) 1992 BA	1.34	0.07	*0.36	167	0	-17.07	7.2	2e-04	–	–	–	4.5	0.12	1991 – 2017
(136770) 1996 PC1	1.84	0.45	*0.28	248	0	-7.98	5.1	1e-02	–	–	–	8.5	0.04	1996 – 2017
(136818) Selqet	0.94	0.35	*0.59	483	0	7.90	3.3	3e-05	–	–	–	8.8	0.07	1997 – 2016
(136993) 1998 ST49	2.31	0.59	*1.02	437	7	24.86	15.0	9e-04	29.07	14.9	1e-04	2.2	0.50	1998 – 2013

Table 2.1, continued.

Name	a	e	D	N_o	N_r	$\langle da/dt \rangle$	σ	p	$\langle da/dt \rangle_r$	σ_r	p_r	s_Y	ξ	Arc
(137924) 2000 BD19	0.88	0.89	0.97	530	5	-22.53	13.7	1e-03	-25.86	10.5	1e-06	1.8	0.08	1996 – 2017
(138175) 2000 EE104	1.00	0.29	*0.31	844	3	-31.66	7.6	1e-12	-32.33	7.6	3e-13	2.6	0.16	1998 – 2017
(138852) 2000 WN10	1.00	0.30	*0.32	853	0	16.46	4.2	2e-13	–	–	–	4.8	0.08	2000 – 2017
(138911) 2001 AE2	1.35	0.08	*0.51	491	0	-14.36	9.4	7e-03	–	–	–	4.0	0.15	1984 – 2015
(152563) 1992 BF	0.91	0.27	0.27	330	0	-13.08	1.3	1e-16	–	–	–	14.0	0.04	1952 – 2017
(152671) 1998 HL3	1.13	0.37	0.30	305	0	-35.10	9.6	4e-12	–	–	–	3.8	0.16	1998 – 2017
(152754) 1999 GS6	1.19	0.50	0.41	275	0	-20.88	16.3	6e-03	–	–	–	2.2	0.12	1999 – 2016
(153201) 2000 WO107	0.91	0.78	0.51	423	0	-22.36	13.2	3e-03	–	–	–	2.1	0.05	2000 – 2017
(154590) 2003 MA3[†]	1.11	0.40	*0.16	87	0	-38.28	19.2	3e-04	–	–	–	3.4	0.09	1997 – 2012
(162004) 1991 VE	0.89	0.66	*0.81	794	2	18.83	3.5	1e-16	21.84	2.8	1e-16	4.9	0.16	1954 – 2015
(162080) 1998 DG16	0.90	0.36	0.78	136	0	-18.25	7.1	1e-05	–	–	–	3.1	0.20	1980 – 2015
(162082) 1998 HL1	1.25	0.19	*0.59	267	0	-43.06	17.9	4e-05	–	–	–	2.1	0.46	1998 – 2016
(162117) 1998 SD15	0.93	0.34	*0.54	496	0	-9.07	1.7	1e-16	–	–	–	14.7	0.07	1998 – 2017
(162142) 1998 VR	0.88	0.32	*0.62	415	0	9.07	3.0	4e-07	–	–	–	9.8	0.09	1998 – 2017
(162162) 1999 DB7	1.21	0.19	*0.37	224	0	20.23	12.3	6e-03	–	–	–	3.7	0.13	1998 – 2016

Table 2.1, continued.

Name	a	e	D	N_o	N_r	$\langle da/dt \rangle$	σ	p	$\langle da/dt \rangle_r$	σ_r	p_r	s_Y	ξ	Arc
(162173) Ryugu	1.19	0.19	*0.49	729	0	-15.99	6.7	2e-07	–	–	–	3.6	0.08	1986 – 2016
(162181) 1999 LF6	1.41	0.28	0.73	1297	2	-11.86	3.3	1e-12	-9.77	3.1	1e-09	5.0	0.13	1979 – 2017
(162361) 2000 AF6	0.88	0.41	*0.32	303	0	20.04	8.8	3e-05	–	–	–	4.0	0.09	1990 – 2014
(162463) 2000 JH5[§]	1.15	0.24	1.05	484	0	-32.47	12.9	7e-07	–	–	–	2.2	0.58	2000 – 2016
(162783) 2000 YJ11	1.31	0.23	*0.25	125	0	-49.32	16.3	2e-08	–	–	–	3.5	0.22	2000 – 2015
(162911) 2001 LL5	1.20	0.34	*0.51	233	0	19.39	13.0	8e-03	–	–	–	3.1	0.16	2001 – 2017
(163023) 2001 XU1	0.80	0.55	*0.49	316	0	34.39	9.0	1e-16	–	–	–	2.9	0.18	2001 – 2017
(164202) 2004 EW[†]	0.99	0.28	*0.25	426	0	27.84	13.6	6e-04	–	–	–	2.4	0.11	2003 – 2015
(164206) 2004 FN18[C]	1.70	0.41	*1.07	489	0	-4.96	4.0	2e-02	–	–	–	9.1	0.10	1954 – 2017
(164207) 2004 GU9	1.00	0.14	0.16	192	0	-32.12	11.8	6e-06	–	–	–	2.3	0.09	2001 – 2017
(174050) 2002 CC19[§]	1.28	0.11	*1.12	363	0	60.23	20.5	3e-06	–	–	–	2.3	1.29	1985 – 2015
(188174) 2002 JC	0.82	0.39	*1.18	286	3	-19.53	12.2	2e-03	-12.08	10.5	3e-02	3.0	0.19	1991 – 2017
(190758) 2001 QH96[§]	1.75	0.36	*0.78	196	0	49.52	27.3	1e-04	–	–	–	3.0	0.75	1994 – 2017
(192563) 1998 WZ6	1.45	0.41	*1.23	670	0	-19.56	7.9	1e-05	–	–	–	2.5	0.32	1998 – 2015
(203471) 2002 AU4	0.86	0.37	*0.47	356	0	-13.71	7.5	9e-04	–	–	–	6.5	0.09	1993 – 2017

Table 2.1, continued.

Name	a	e	D	N_o	N_r	$\langle da/dt \rangle$	σ	p	$\langle da/dt \rangle_r$	σ_r	p_r	s_Y	ξ	Arc
(208023) 1999 AQ10	0.93	0.24	*0.30	329	3	-24.89	7.1	6e-14	-23.77	6.0	1e-16	4.7	0.12	1998 – 2017
(215442) 2002 MQ3[†]	0.91	0.27	1.07	328	0	-20.40	12.0	4e-04	–	–	–	2.2	0.33	2002 – 2016
(216523) 2001 HY7	0.91	0.41	*0.27	288	0	30.74	6.0	1e-16	–	–	–	6.1	0.11	2001 – 2016
(230111) 2001 BE10	0.82	0.37	*0.54	746	3	-15.38	6.2	1e-07	-13.98	5.9	6e-07	4.7	0.10	2000 – 2016
(234341) 2001 FZ57	0.94	0.60	0.34	205	0	-26.41	20.2	5e-02	–	–	–	3.3	0.10	1991 – 2013
(235756) 2004 VC[§]	1.13	0.26	1.14	201	1	-32.67	15.6	2e-04	-32.36	15.6	2e-04	2.7	0.62	1992 – 2016
(249886) 2001 RY11[§]	1.48	0.28	1.20	337	0	35.16	22.9	6e-03	–	–	–	2.4	0.80	1992 – 2015
(252399) 2001 TX44[†]	0.87	0.55	0.29	132	0	-57.07	26.2	2e-03	–	–	–	2.2	0.19	2001 – 2014
(252558) 2001 WT1	1.09	0.40	0.53	206	0	-58.28	15.7	2e-07	–	–	–	2.8	0.46	2001 – 2017
(256004) 2006 UP[†]	1.59	0.30	*0.09	167	0	-65.21	19.5	2e-08	–	–	–	2.4	0.11	2002 – 2017
(267759) 2003 MC7[C]	1.37	0.18	*0.62	300	0	-10.83	3.5	2e-08	–	–	–	14.4	0.13	1953 – 2017
(283457) 2001 MQ3[C]	2.23	0.46	*0.54	310	0	-13.72	4.9	2e-07	–	–	–	14.1	0.15	1951 – 2012
(297418) 2000 SP43	0.81	0.47	0.41	672	1	-16.34	7.9	8e-07	-16.36	7.9	7e-07	2.9	0.08	2000 – 2017
(306383) 1993 VD	0.88	0.55	*0.18	101	0	-11.41	6.6	5e-03	–	–	–	7.1	0.02	1993 – 2017
(307070) 2002 AV31	1.31	0.25	*0.26	233	0	-22.98	11.5	2e-03	–	–	–	3.4	0.11	2001 – 2017

Table 2.1, continued.

Name	a	e	D	N_o	N_r	$\langle da/dt \rangle$	σ	p	$\langle da/dt \rangle_r$	σ_r	p_r	s_Y	ξ	Arc
(310442) 2000 CH59	0.86	0.42	*0.37	340	0	28.82	6.8	3e-13	–	–	–	4.5	0.14	1999 – 2017
(326354) 2000 SJ344[†]	1.14	0.17	*0.11	37	0	-43.98	42.9	5e-04	–	–	–	2.3	0.08	2000 – 2012
(326683) 2002 WP[†]	1.45	0.22	0.52	767	0	11.80	5.5	9e-06	–	–	–	4.6	0.12	2002 – 2017
(330659) 2008 GG2[†]	1.59	0.28	*0.09	169	0	23.85	11.2	4e-04	–	–	–	4.7	0.04	2003 – 2016
(344074) 1997 UH9	0.83	0.47	*0.65	325	0	31.18	10.8	8e-07	–	–	–	3.0	0.27	1997 – 2017
(348306) 2005 AY28[†]	0.87	0.57	*0.19	221	2	-76.16	23.2	1e-07	-79.90	23.1	4e-08	2.4	0.16	2004 – 2017
(350462) 1998 KG3	1.16	0.12	*0.14	170	0	-26.27	7.8	4e-10	–	–	–	5.2	0.06	1998 – 2013
(350523) 2000 EA14[†]	1.12	0.20	*0.21	145	0	43.85	20.4	9e-04	–	–	–	2.4	0.16	1999 – 2013
(358453) 2007 EH88	1.12	0.44	*0.39	117	0	-41.28	25.2	2e-02	–	–	–	2.2	0.23	1993 – 2014
(363505) 2003 UC20[C]	0.78	0.34	1.90	400	5	-4.24	0.9	1e-16	-4.41	0.9	1e-16	31.6	0.11	1954 – 2017
(363599) 2004 FG11[†]	1.59	0.72	0.15	246	8	-33.78	7.9	2e-13	-37.35	7.2	1e-16	5.0	0.06	2003 – 2016
(364136) 2006 CJ[†]	0.68	0.75	*0.32	241	11	-25.18	11.2	1e-04	-38.38	1.8	1e-16	1.5	0.07	2005 – 2017
(373393) 1972 RB[†C]	2.15	0.49	*0.54	65	0	5.56	5.5	4e-02	–	–	–	22.5	0.06	1950 – 2016
(385186) 1994 AW1	1.11	0.08	*1.02	1589	3	4.10	2.8	3e-04	4.12	2.7	2e-04	6.3	0.08	1986 – 2017
(388189) 2006 DS14[†]	0.86	0.34	0.32	197	0	-23.38	12.7	6e-03	–	–	–	3.5	0.10	2001 – 2014

Table 2.1, continued.

Name	a	e	D	N_o	N_r	$\langle da/dt \rangle$	σ	p	$\langle da/dt \rangle_r$	σ_r	p_r	s_Y	ξ	Arc
(390522) 1996 GD1[†]	1.19	0.35	*0.27	92	0	-29.07	16.9	7e-03	–	–	–	3.0	0.13	1996 – 2014
(399308) 1993 GD	1.10	0.24	*0.26	113	0	44.26	9.6	3e-12	–	–	–	5.7	0.19	1993 – 2015
(401885) 2001 RV17[†]	0.91	0.34	*0.28	181	0	-19.09	8.8	4e-04	–	–	–	5.4	0.08	2001 – 2016
(412976) 1987 WC	1.36	0.23	*0.37	155	0	42.09	17.9	1e-04	–	–	–	3.2	0.29	1987 – 2015
(412977) 1990 UO	1.26	0.77	*0.45	115	0	44.74	25.7	7e-03	–	–	–	2.4	0.15	1990 – 2015
(415711) 1998 WT7[§]	1.15	0.11	*0.56	169	0	50.30	24.7	5e-04	–	–	–	2.1	0.51	1998 – 2015
(416151) 2002 RQ25[†]	1.11	0.31	*0.26	230	6	16.71	12.9	5e-02	19.52	9.6	1e-03	3.4	0.08	2002 – 2017
(433953) 1997 XR2	1.08	0.20	*0.25	407	8	14.78	9.7	9e-03	11.65	7.7	9e-03	3.3	0.05	1997 – 2017
(437844) 1999 MN	0.67	0.67	*0.19	141	4	37.93	3.9	1e-16	37.42	3.8	1e-16	9.6	0.05	1999 – 2015
(441987) 2010 NY65[†]	1.00	0.37	0.23	257	16	12.89	29.9	5e-01	-18.44	1.9	1e-16	1.0	0.06	2010 – 2017
(443837) 2000 TJ1	1.16	0.08	0.25	355	0	-9.71	7.1	2e-03	–	–	–	5.7	0.04	2000 – 2016
(452389) 2002 NW16	1.11	0.03	0.85	1107	0	-9.67	5.4	7e-04	–	–	–	2.9	0.15	2001 – 2017
(455146) 1993 FS	2.23	0.42	*0.43	103	0	38.44	17.9	7e-04	–	–	–	3.4	0.34	1992 – 2016
(455176) 1999 VF22	1.31	0.74	*0.27	134	0	-64.33	13.4	4e-12	–	–	–	4.4	0.15	1999 – 2016
(461353) 1999 LS7	1.01	0.30	*0.25	134	0	-48.53	22.9	4e-04	–	–	–	2.0	0.19	1999 – 2016

Table 2.1, continued.

Name	a	e	D	N_o	N_r	$\langle da/dt \rangle$	σ	p	$\langle da/dt \rangle_r$	σ_r	p_r	s_Y	ξ	Arc
(467336) 2002 LT38†	0.85	0.31	*0.28	307	0	11.67	6.2	2e-03	–	–	–	5.9	0.05	2002 – 2016
(468468) 2004 KH17†	0.71	0.50	0.20	211	1	-43.87	5.4	1e-16	-43.86	5.4	1e-16	5.8	0.09	2004 – 2016
(469445) 2002 LT24†	0.72	0.50	0.14	185	0	-26.83	19.7	4e-02	–	–	–	2.3	0.04	2002 – 2016
(470975) 2009 SC15†	1.27	0.18	*0.19	241	2	-63.61	21.2	5e-07	-55.31	20.2	5e-06	2.1	0.19	2002 – 2016
(474158) 1999 FA	1.08	0.13	*0.26	225	0	-41.26	9.2	1e-16	–	–	–	2.2	0.20	1978 – 2017
(474163) 1999 SO5	1.09	0.07	*0.23	255	0	-28.61	11.5	2e-04	–	–	–	3.1	0.12	1999 – 2017
(480808) 1994 XL1	0.67	0.53	*0.23	186	0	-31.77	3.5	1e-16	–	–	–	16.0	0.07	1994 – 2017
(480883) 2001 YE4	0.68	0.54	*0.26	349	7	-47.11	2.1	1e-16	-50.06	0.6	1e-16	9.9	0.13	2001 – 2017
(481442) 2006 WO3	0.80	0.45	*0.17	291	0	-42.51	9.0	1e-16	–	–	–	3.7	0.09	2001 – 2017
(483656) 2005 ES70†	0.76	0.39	*0.06	137	0	-72.82	5.1	1e-16	–	–	–	10.3	0.06	2004 – 2017
2004 SC56†	0.77	0.43	0.29	180	0	-42.90	27.8	2e-03	–	–	–	1.7	0.15	2004 – 2010
2004 BG41†	2.51	0.61	*0.05	90	0	-51.24	30.0	8e-03	–	–	–	1.9	0.04	2003 – 2016
2007 PB8†	0.88	0.45	*0.23	80	0	-50.05	33.7	2e-02	–	–	–	1.5	0.15	2002 – 2012
2009 BD†	1.06	0.05	*0.01	190	0	-497.62	99.3	6e-13	–	–	–	0.6	0.07	2008 – 2011

2.8 Comparison with Nugent et al. (2012)

2.8.1 Using matching observation intervals

We analyzed the 54 Yarkovsky objects described by Nugent et al. (2012) by constructing observation intervals whose calendar years matched those listed in Table (3) of that work. We compared (Section 2.6) our results with their findings (Figure 2.1). We agreed with all $\langle da/dt \rangle$ values save one, (4179) Toutatis, for which we found a z-score of 2.68. We examine this object in more detail in Section 2.13.5.

However, we also found that 23 objects that Nugent et al. (2012) identified as detections did not pass our detection threshold (Section 2.5.2). Much of this discrepancy is explained by this work's higher threshold for detection — a p-value of 0.05 approximately corresponds to an S/N of 2, while Nugent et al. (2012) considered possible detections for objects with S/N > 1. Indeed, all but five of the 23 objects exhibit $1 <$ S/N < 2 in Nugent et al. (2012)'s table.

2.8.2 Using all available data

When using all available data (including data that were not available for use by Nugent et al. (2012)), we found good agreement (Figure 2.2), except for two objects — (4179) Toutatis and (1620) Geographos — for which our drift rates do not match those of Nugent et al. (2012).

2.9 Comparison with Farnochhia et al. (2013)

2.9.0.1 Using matching observation intervals

We analyzed the 47 Yarkovsky objects found by Farnocchia et al. (2013b) using matching observation intervals (to the nearest calendar year) and compared (Section 2.6) our results with their findings. We found agreement on all $\langle da/dt \rangle$ values

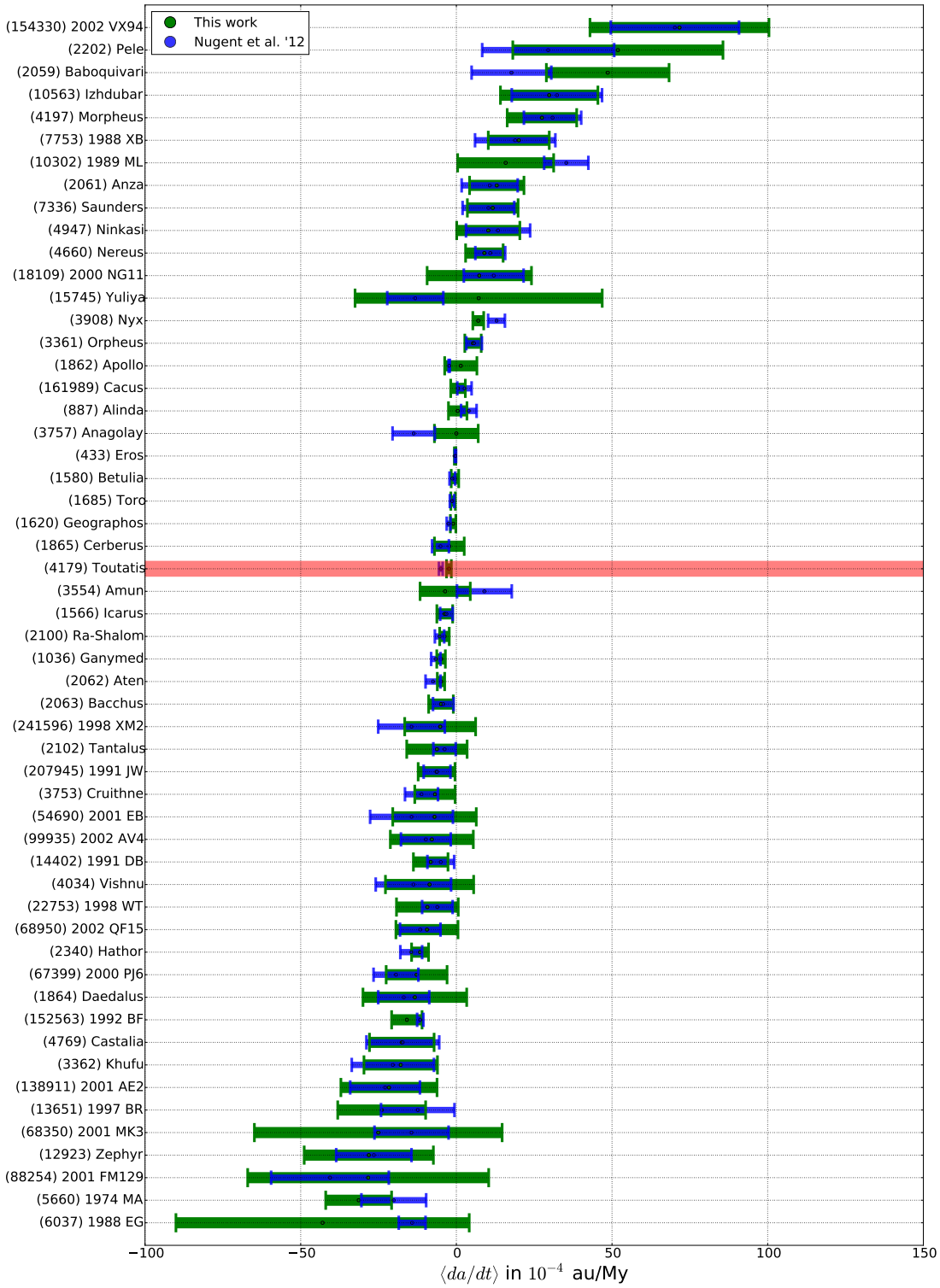

Figure 2.1: A comparison of our Yarkovsky detections (green) and those determined by Nugent et al. (2012) (blue), when we used only matching data. Measurements that disagreed (i.e., $z_i > 2$, Section 2.6) are highlighted in red. Objects are ranked from most positive to most negative Yarkovsky drift rate.

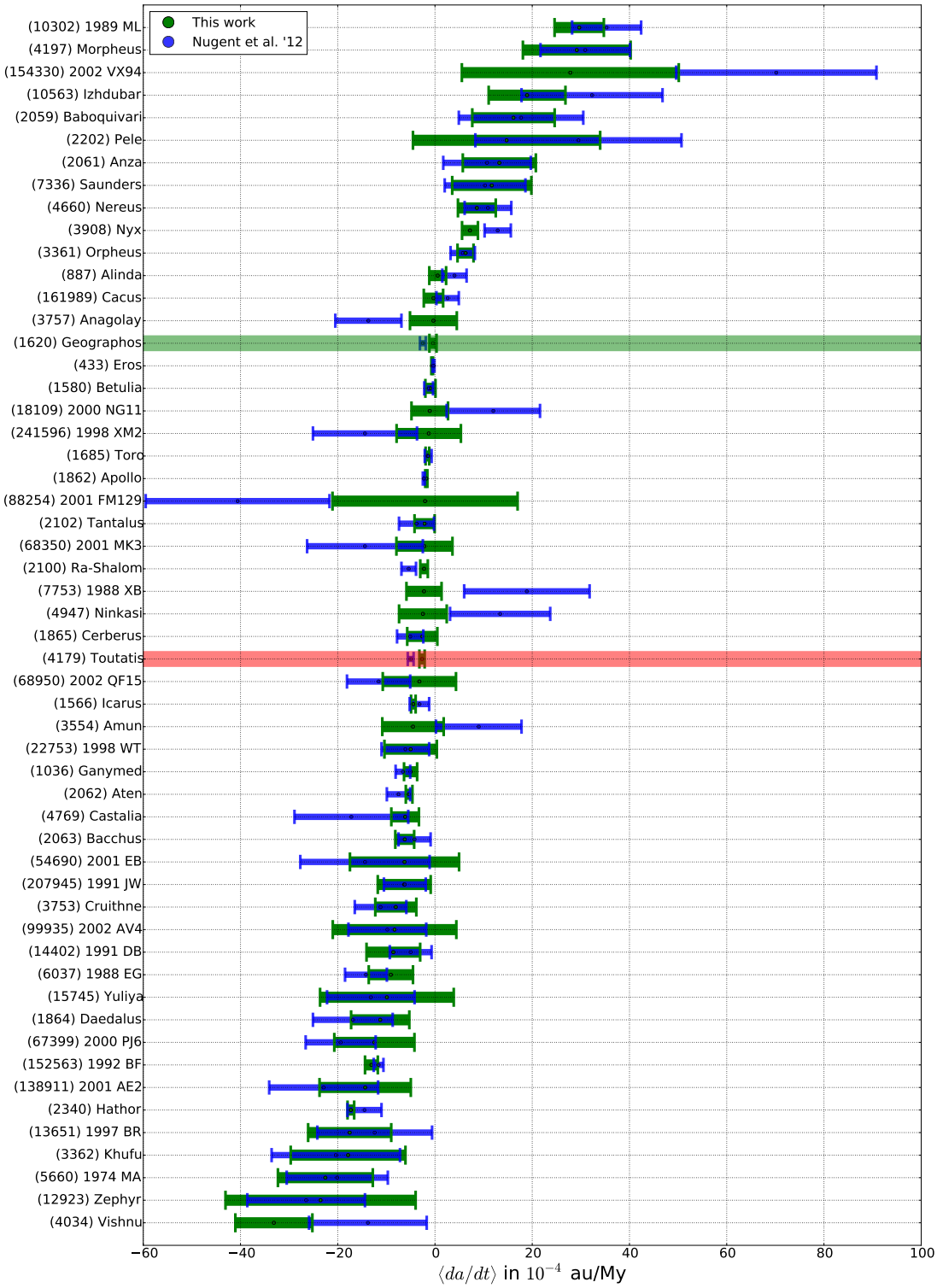

Figure 2.2: A comparison of our Yarkovsky detections (green) and those determined by Nugent et al. (2012) (blue), when we used all available data. Measurements that disagreed (i.e., $z_i > 2$, Section 2.6) only when using all available data are highlighted in green, while those that also disagreed when matching observational intervals are highlighted in red. Objects are ranked from most positive to most negative Yarkovsky drift rate.

(Figure 2.3).

We found four objects – (105140) 2000 NL10, (326290) Akhenaten, (339714) 2005 ST1 , and 2003 XV – that were considered to be detections by Farnocchia did not pass our detection thresholds (Section 2.5.2). However, all four of these discrepant objects are listed in Tables 3 and 4 of Farnocchia et al. (2013b), indicating that they are either "less reliable" detections or have low S/N values.

2.9.1 Using all available data

When using all available data, we found relatively good agreement (Figure 2.4). However, we found three objects — (2100) Ra-Shalom, (326290) Akhenaten, and (6239) Minos — for which our drift rates do not match those of Farnocchia et al. (2013b). We discuss these special cases in Section 2.13.6.

2.10 Yarkovsky efficiency distribution

Equations 2.3 and 2.4 provide a mechanism to interpret the drift in semi-major axis $\langle da/dt \rangle$ in terms of physical parameters of the measured object. In particular, $\langle da/dt \rangle$ can be described in terms of the Yarkovsky efficiency, ξ, where $0 < \xi < 1$. However, the relationship between $\langle da/dt \rangle$ and ξ depends on density and diameter, and thus determination of ξ requires estimation of these physical parameters.

Diameters were extracted from the Small Body Database (SBDB) (JPL Solar System Dynamics, 2017b, see also Section 2.12). Densities were assigned according to SMASS II taxonomic types, which we also extracted from the SBDB, using the mean densities reported by Carry (2012). Objects of unknown taxonomic type were assigned a density equal to the mean density (2470 kg/m^3) for the objects in our sample with known type.

We analyzed the distribution of ξ values and found a median Yarkovsky effi-

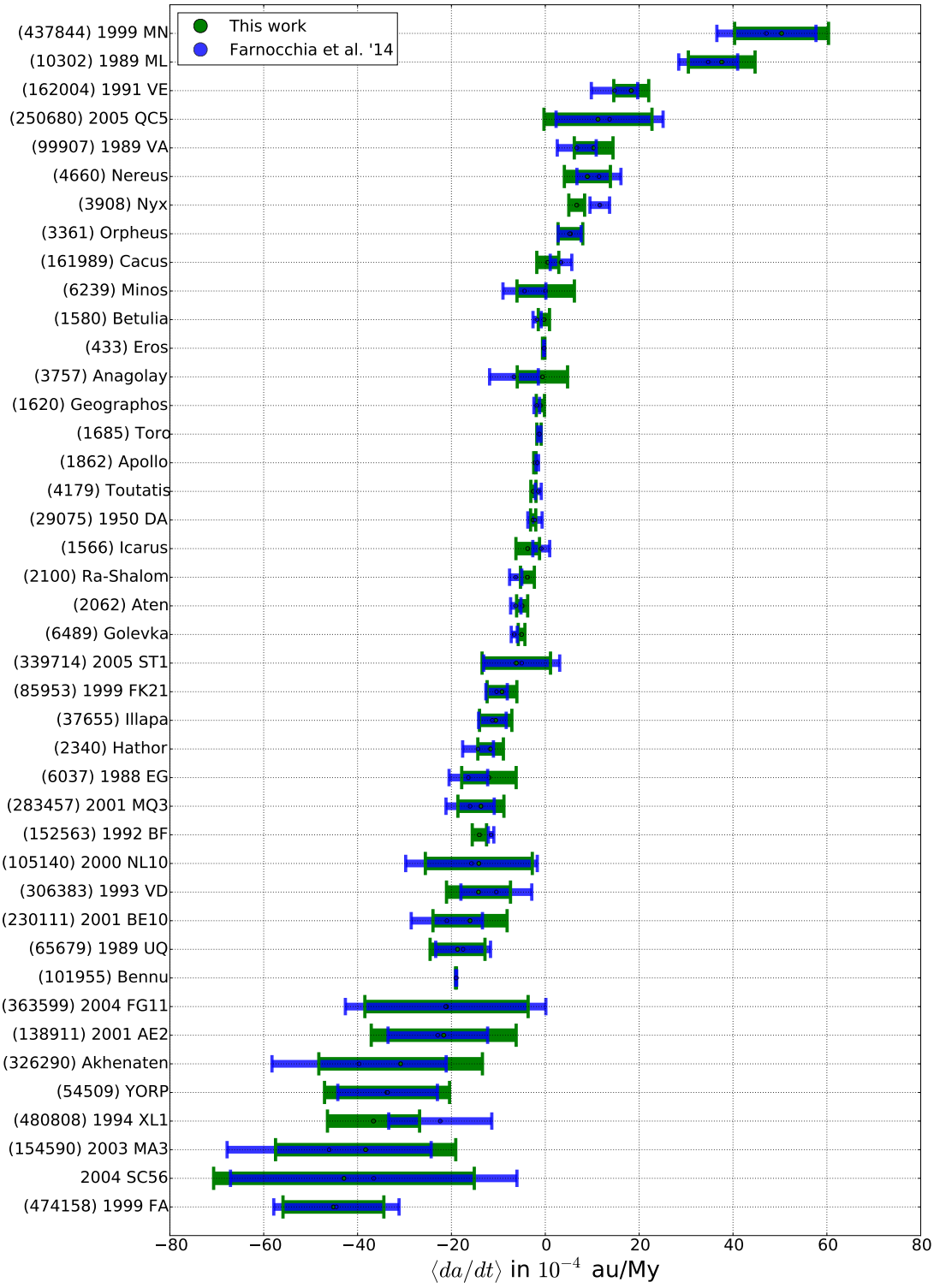

Figure 2.3: A comparison of our Yarkovsky detections (green) and those determined by Farnocchia et al. (2013b) (blue), when we used matching data arcs. Measurements that disagreed (i.e., $z_i > 2$, Section 2.6) are highlighted in red. Some objects (2009 BD, 2004 BG41, 2007 PB8, 2003 XV, (483656) 2005 ES70) were not included in this plot for display purposes, but all of them have $z_i <= 2$. Objects are ranked from most positive to most negative Yarkovsky drift rate.

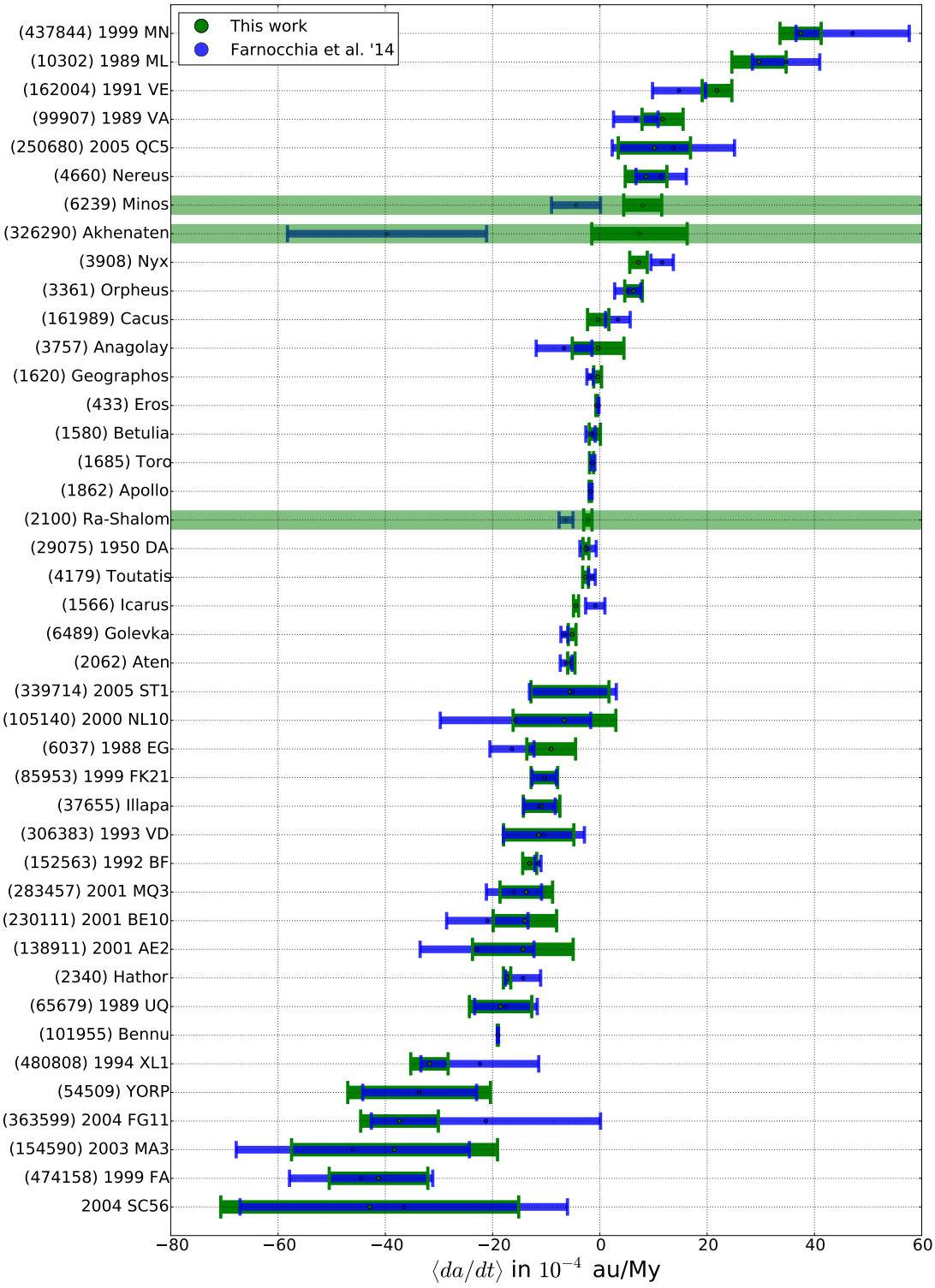

Figure 2.4: A comparison of our Yarkovsky detections (green) and those determined by Farnocchia et al. (2013b) (blue), when we used all available data. Measurements that disagreed (i.e., $z_i > 2$, Section 2.6) are highlighted in green. Some objects (2009 BD, 2004 BG41, 2007 PB8, 2003 XV, (483656) 2005 ES70) were not included in this plot for display purposes, but all of them had $z_i <= 2$. Objects are ranked from most positive to most negative Yarkovsky drift rate.

ciency of $\xi = 0.12^{+0.17}_{-0.06}$ (Figure 2.5). Note that a bias in this estimate stems from our inability to report near-zero drift rates as Yarkovsky detections. Therefore, the true distribution of efficiencies is presumably shifted toward lower values than presented here.

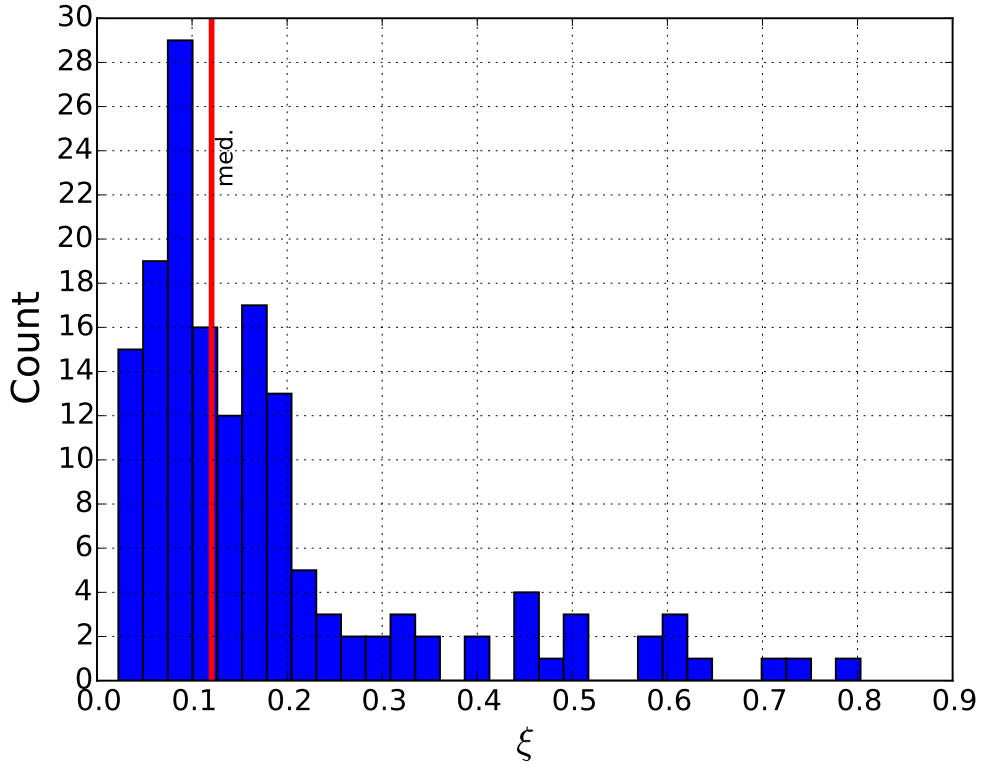

Figure 2.5: The distribution of Yarkovsky efficiencies ξ measured with our sample of 159 objects. Diameter and density assumptions are described in the text. The median efficiency, $\xi = 0.12$, is shown with a red vertical line. For clarity, we did not plot two objects with unphysical (>1) efficiencies (Section 2.13.7).

Several objects exhibit Yarkovsky efficiencies that substantially exceed the median value of $\xi = 0.12$. For these objects, the non-gravitational influence, if real, may be unrelated to Yarkovsky (e.g., sublimation). It is also possible that some of the high-efficiency detections are fictitious (e.g., faulty astrometry). For these reasons, we added a cautionary flag to a dozen objects with Yarkovsky efficiencies above 0.5 in Table 2.1. We discuss two unphysical detections in Section 2.13.7.

2.11 Spin orientation distribution

La Spina et al. (2004) provided an estimate of the ratio of retrograde to prograde rotators ($N_R/N_P = 2^{+1}_{-0.7}$) in the NEA population from a survey of spin vectors.

Measurements of the Yarkovsky drift rate can also be used to infer N_R/N_P, because objects with a positive $\langle da/dt \rangle$ are almost certain to be prograde rotators, while objects with a negative $\langle da/dt \rangle$ are almost certain to be retrograde rotators.

However, given a population of objects with estimated $\langle da/dt \rangle$ values, the best estimate of N_R/N_P is *not* equal to the ratio R of the number of objects with negative $\langle da/dt \rangle$ to the number with positive $\langle da/dt \rangle$. A bias occurs because each estimated $\langle da/dt \rangle$ value has an associated uncertainty, and there is thus a non-zero probability that an object with a measured positive $\langle da/dt \rangle$ value in fact has a negative $\langle da/dt \rangle$ value (and vice versa). Because there are more retrograde rotators than prograde rotators, this process will bias observers towards measuring a lower observed ratio, R_O, than is actually present.

This point can be illustrated with a simple (albeit exaggerated), analytic example. Consider four objects: A, B, C, and D. Objects A, B, and C all have $\langle da/dt \rangle$ values of $-10 \pm 25 \times 10^{-4}$ au/My, while object D has a $\langle da/dt \rangle$ value of $+10 \pm 25 \times 10^{-4}$ au/My. In this example, the true ratio, R_T, of the number of objects with negative $\langle da/dt \rangle$ to the number of objects with positive $\langle da/dt \rangle$ is $R_T = 3.0$. However, when an observer attempts to measure, for example, $\langle da/dt \rangle_A$, there is a $\sim$34% chance that she will erroneously conclude that A has a positive $\langle da/dt \rangle$ value. In fact, we can calculate the probabilities associated with each of the five possible ratios that can be observed (Table 2.2) and demonstrate that one is most likely to observe $R_O = 1.0$. If 10,000 observers independently took measurements of objects A, B, C, and D, a plurality would conclude that $R_O = 1.00$, while a majority would agree that R_O lies between 0.0 and 1.0 — even though the true ratio is $R_T = 3.0$.

Table 2.2: The probability (P, rightmost column) of measuring a given ratio (R_O) of number of objects with $\langle da/dt \rangle < 0$ ($N_{<0}$) to number of objects with $\langle da/dt \rangle > 0$ ($N_{>0}$) for a sample of objects with true ratio $R_T = 3.0$ (Section 2.11). The true ratio is not the most likely result for an observer to measure.

$N_{<0}$	$N_{>0}$	R_O	P
4	0	∞	10%
3	1	3.00	34%
2	2	1.00	37%
1	3	0.33	17%
0	4	0.00	3%

Our data suggest that out of 159 objects, 114 have $\langle da/dt \rangle < 0$, for an observed ratio of $R_O = \frac{114}{159-114} = 2.53$. To approximate the true ratio R_T, we assumed that the nominal ratio we measured was the most likely ratio for any observer to measure. Determining the true ratio is then a matter of simulating a universe with a set of simulated $\langle da/dt \rangle$ values that are consistent with our measured values, and also yield $R_O = 2.53$.

To find the value of R_T that corresponds to our measured R_O value, we ran a set of nested Monte Carlo simulations, using the following procedure:

1. Create a new 'universe', U_i.

    (a) Within U_i, generate a set of 159 $\langle da/dt \rangle$ values, pulled from distributions consistent with our measurements. This set of $\langle da/dt \rangle$ values are the true values for the 159 objects in universe U_i. Therefore, R_T can be calculated (exactly) for this universe.

    (b) Simulate what 10^4 independent observers in universe U_i would measure as an observed ratio, R_O.

(c) Determine the mean and standard deviation in observed ratio (R_O and σ_R, respectively) in universe U_i (Figure 2.6).

2. Repeat step 1 over many ($\sim 10^3$) universes, and record the set of resulting distinct R_T values, and corresponding R_O, σ_R values.

3. Determine the set of R_T values for which $R_O \pm \sigma_R$ encompasses our observed ratio of $R_O = 2.53$.

The resulting simulations suggest that the most likely true ratio for our observed 159 objects is $R_T = 2.9 \pm 0.4$.

If we wish to relate the ratio of retrograde-to-prograde rotators in our data to the corresponding ratio amongst the entire population of NEAs, we must also account for sampling errors, which will further broaden the uncertainties on R. The sampling uncertainty σ_S on a measured ratio of R from a sample of N objects can be calculated directly from the standard deviation of the binomial distribution, and is given by

$$\sigma_S \approx \sqrt{NR} \times \frac{R+1}{N-R}. \tag{2.11}$$

The sampling uncertainty for R is therefore $\sigma_S = 0.5$, which suggests a Yarkovsky-based estimate for the ratio of retrograde-to-prograde NEAs of

$$N_R/N_P = 2.9 \pm 0.7. \tag{2.12}$$

The ratio of retrograde-to-prograde rotators can in principle provide bounds on the fraction of NEAs that enter near-Earth space through the ν_6 resonance (Nugent et al., 2012; Farnocchia et al., 2013b). The inference is complicated by observational bias, namely an over-representation of Atens in the observed sample compared to their expected fraction in a debiased population. If we attempt to account for this bias in a manner similar to that described by Farnocchia et al. (2013b), we find

$$N_R/N_{P\ \text{(debiased)}} = 2.1 \pm 0.7, \tag{2.13}$$

which gives a probability of ν_6 provenance of $0.35^{+0.12}_{-0.18}$.

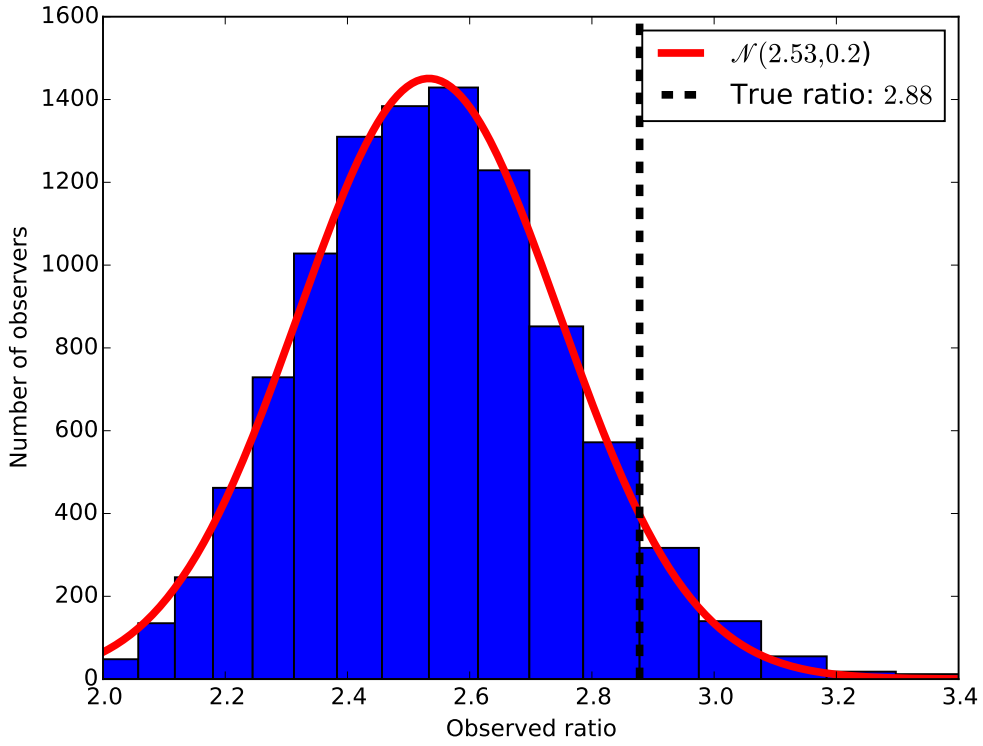

Figure 2.6: The number of observers measuring a given ratio R_O, for 10^4 independent observers measuring 159 simulated objects with $\langle da/dt \rangle$ values consistent with what we measured (Section 2.11). For a true ratio of $R_T = 2.9$, most observers will measure a ratio near $R_O = 2.53$. This bias must be corrected for when estimating the ratio of retrograde-to-prograde rotators from Yarkovsky observations.

2.12 Yarkovsky effect's diameter dependence

Equations 2.3 and 2.4 illustrate the relationship between the magnitude of the Yarkovsky effect and the affected object's physical parameters. In particular, the theoretical formulation of this effect predicts a $D^{-1.0}$ dependence. Verifying this dependence with our data serves as a check on the theoretical underpinnings of the effect, and also validates our results.

We obtained diameter estimates for objects in our sample from JPL's SBDB

(JPL Solar System Dynamics, 2017b). For those objects with no listed diameter, we estimated the diameter from the object's H-magnitude using

$$D = \frac{10^{-0.2H}}{\sqrt{p_V}} 1329 \text{ km}, \tag{2.14}$$

with an assumed geometric albedo, p_V, of 0.14 (Stuart & Binzel, 2004). If the uncertainty in diameter was available in the SBDB, we used it, otherwise we set the uncertainty to a third of the diameter.

Here we note that while the analytical formulation of our Yarkovsky force model includes parameters that are dependent on the physical properties of the affected object (Section 2.4), the actual fit itself is dependent *only* on dynamics. In other words, our fits measure only the overall magnitude of the Yarkovsky acceleration, and are entirely agnostic about physical parameters such as diameter. Therefore, we can examine the Yarkovsky drift's dependence on diameter independently from the determination of the magnitude of the drift itself, and be confident that we are not committing a *petitio principii*.

We fit a power-law of the form

$$\langle da/dt \rangle = C \times D^p, \tag{2.15}$$

to describe the relationship between the magnitude of the Yarkovsky effect and the object diameter. We used an Orthogonal Distance Regression (ODR) (Jones et al., 2001–) algorithm to perform this fit, due to the potential errors present in both the dependent ($\langle da/dt \rangle$) and independent (D) variables (Figure 2.7). The resulting fit gave a best-fit power-law slope of $p = -1.05 \pm 0.06$. We verified the robustness of this result against the choice of diameter uncertainties, with values ranging from a fourth to two thirds of the diameter, and found consistent results. We also verified this result against different starting conditions on p. We discuss this result further in Section 2.14.4.

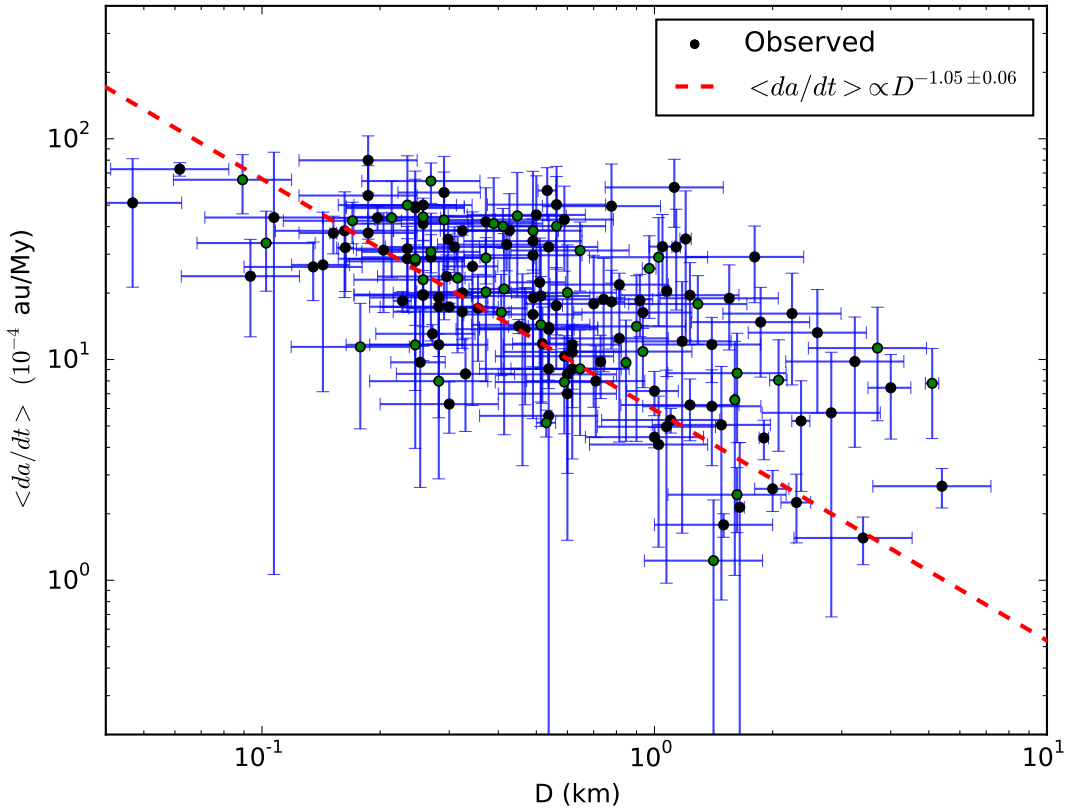

Figure 2.7: Drift rate $\langle da/dt \rangle$ as a function of object diameter, D. Diameters were either estimated from an H-magnitude (black) or extracted from the SBDB (green). Our analysis yields a diameter dependence of $D^{-1.05 \pm 0.06}$, consistent with the theoretical expectation for the Yarkovsky effect of $D^{-1.0}$.

2.13 Objects of interest

2.13.1 (152563) 1992 BF

The 1992 BF astrometry includes four optical measurements taken in 1953. Vokrouhlický et al. (2008) showed that these points suffered from systematic errors due to faulty catalog debiasing, and re-analyzed these measurements to determine more accurate values. We used these corrected data, and determined $\langle da/dt \rangle = -13.1 \pm 1.3 \times 10^{-4}$ au/My, which has a z-score of 1.62 with respect to Vokrouhlický et al. (2008)'s determination. The 1992 BF Yarkovsky drift was also measured

with these points from 1953 discarded, which yielded $\langle da/dt \rangle = -14.0 \pm 2.4 \times 10^{-4}$ au/My.

2.13.2 2009 BD

Farnocchia et al. (2013b) found a drift rate for 2009 BD of $\langle da/dt \rangle = -493.4 \pm 58.8 \times 10^{-4}$ au/My. Following the work of Micheli et al. (2012), Farnocchia et al. (2013b) also fit for a Solar Radiation Pressure (SRP) model for this object – which introduces a radial acceleration as a function of Area-to-Mass Ratio (AMR) – and found AMR=$(2.72 \pm 0.39) \times 10^{-4}$ m^2/kg. Micheli et al. (2012) found AMR=$(2.97 \pm 0.33) \times 10^{-4}$ m^2/kg with a solution that did not include Yarkovsky.

We also included an SRP component in our force model for 2009 BD, and found an area-to-mass ratio of $(2.21 \pm 0.40) \times 10^{-4}$ m^2/kg, with a Yarkovsky drift rate of $\langle da/dt \rangle = -497.6 \pm 40.5 \times 10^{-4}$ au/My. The drastic improvement in goodness-of-fit when both Yarkovsky and SRP models are included (Table 2.3) strongly supports the presence of these forces. We note that while our uncertainties on the drift rate appear to be around 20% better than those of Farnocchia et al. (2013b), this may be due to the method by which we fit for $\langle da/dt \rangle$, which was performed as a secondary minimization after fitting for the dynamical state vector. Therefore, our uncertainties in $\langle da/dt \rangle$ do not account for correlation between parameters, and may be an underestimate because two related, non-gravitational effects are present.

2.13.3 (483656) 2005 ES70

The drift in semi-major axis for 2005 ES70 is $\langle da/dt \rangle = -72.8 \pm 5.1 \times 10^{-4}$ au/My. Not only is this a strong effect, but it is also an unusually strong detection, with a p-value less than 10^{-16}, and an S/N greater than 14. Farnocchia et al. (2013b) found $\langle da/dt \rangle = -55.6 \pm 16.7 \times 10^{-4}$ au/My using pre-2013 astrometry, which

Table 2.3: Goodness-of-fit (χ^2) for 2009 BD, using various non-gravitational dynamical models, with 190 total observations prior to outlier rejection. The inclusion of both Yarkovsky forces and Solar Radiation Pressure (SRP) yields both a significantly lower χ^2, as well as a decrease in the number of outliers, $N_{\rm out}$.

Model	χ^2	$N_{\rm out}$
Gravity-only	109	7
Yarkovsky	95	7
SRP	90	7
Yarkovsky+SRP	75	4

is consistent with our re-analysis of this object using the same arc ($\langle da/dt \rangle = -54.1 \pm 17.7 \times 10^{-4}$ au/My).

The drop in uncertainty by over a factor of three in four years is likely due to the increase in data coverage. This object has a total of 132 optical and no radar observations since its discovery in 2005. Of these points, 48 were measured after 2011, and were therefore not included in the analysis performed by Farnocchia et al. (2013b). This means that the dataset has increased in size by over 50% since 2011, and the arc has grown by 100%, which likely explains the drop in uncertainty.

The strength of this effect appears to be anomalous – however, when we account for this object's small size, we find that its drift rate is reasonable. Specifically, the diameter of 2005 ES70 is ∼60 m, as calculated from an H-magnitude 23.8 (Equation 2.14), which corresponds to a Yarkovsky efficiency of $\xi = 0.06$, assuming a density of 2470 kg/m^3.

2.13.4 (480883) 2001 YE4, (364136) 2006 CJ & (437844) 1999 MN

2001 YE4 has among the largest drift rates in this data set, while also having amongst the smallest uncertainties, with $\langle da/dt \rangle = -50.1 \pm 0.6 \times 10^{-4}$ au/My. The small uncertainty is largely explained by the seven radar measurements over three ranging apparitions — an analysis of the drift that does not include these points yields $\langle da/dt \rangle = -47.1 \pm 2.1 \times 10^{-4}$ au/My, which means that the radar astrometry reduced the uncertainty by 70%. The drift rate, while large, corresponds to a Yarkovsky efficiency of $\xi = 0.13$, which is close to the median efficiency for the objects we analyzed.

Like 2001 YE4, 2006 CJ represents a strong Yarkovsky detection with $\langle da/dt \rangle = -38.4 \pm 1.8 \times 10^{-4}$ au/My, and similarly, the relatively small uncertainty on this rate is largely due to radar observations. Our analysis includes 11 range and Doppler measurements of 2006 CJ from 2012 to 2017, and these points reduced the uncertainty on this detection by ∼85%.

With a drift rate of $\langle da/dt \rangle = 37.4 \pm 3.8 \times 10^{-4}$ au/My, 1999 MN is notable not only for the high drift rate and S/N, but also for having a semi-major axis that is increasing rather than decreasing. This object's small semi-major axis ($a = 0.67$ au), combined with a large eccentricity ($e = 0.67$), means that this object has a drift that is over twice as large as that of an asteroid at 1 au with low eccentricity with the same size and density. The Yarkovsky efficiency for 1999 MN is $\xi = 0.05$.

All three objects are part of an observational program designed to test general relativity and measure the oblateness of the Sun (Margot & Giorgini, 2010; Verma et al., 2017). Their Yarkovsky drift rates will be taken into account in future analyses.

2.13.5 (4179) Toutatis

(4179) Toutatis is the only object in our sample for which our rate disagreed with a previous work's result when using similar observation intervals – namely, our rate of $\langle da/dt \rangle = -2.4 \pm 0.8 \times 10^{-4}$ au/My has a z-score of 2.7 when compared to Nugent et al. (2012)'s rate of $\langle da/dt \rangle = -5.0 \pm 0.6 \times 10^{-4}$ au/My. Our rate when using all available data, $\langle da/dt \rangle = -2.7 \pm 0.5 \times 10^{-4}$ au/My, is also not consistent with the previous work's result.

Our rates do agree with Farnocchia et al. (2013b), who found $\langle da/dt \rangle = -1.5 \pm 0.6 \times 10^{-4}$ au/My. Farnocchia et al. (2013b) suggest that this object's passage through the Main Belt may make its orbit particularly sensitive to the number and mass of gravitational perturbers.

Another curiosity surrounding Toutatis is the drastic change in drift rate that we found when including radar observations, compared to using only optical observations – including radar observations results in an apparent ∼80% drop in the calculated drift rate.

We found that the difference $\langle da/dt \rangle_o - \langle da/dt \rangle_{r+o}$ between Toutatis's optical-only drift rate and the radar+optical drift rate is a strong function of the mass of the 24 Main Belt perturbing objects included in our force model. The perturbers included in our integration account for only ∼50% of the total mass of the Main Belt. Artificially increasing the overall mass of these perturbers brings the $\langle da/dt \rangle_o$ value into closer agreement with the $\langle da/dt \rangle_{r+o}$ value. An incomplete dynamical model may therefore explain the discrepancy between Toutatis's optical-only rate and radar+optical rate.

A final peculiarity about Toutatis is that its orbit can be determined without any optical astrometry. We fit our gravity-only and Yarkovsky models to the 55 radar measurements obtained over 5 apparitions. The solutions are almost exactly the same as the solutions that include optical astrometry (Table 2.4).

Furthermore, a trajectory fit using only radar data is consistent with optical data – the radar-only trajectory yields a goodness-of-fit of $\chi^2_{\rm opt} = 1775$ with 11,580 degrees-of-freedom, when compared with optical data.

These results suggest that the 55 radar observations over 5 apparitions are enough data to obtain a trajectory that is better than one inferred from over 11,000 distinct optical measurements.

Table 2.4: Toutatis's orbital elements at epoch 01-JAN-2000 00:00:00 UTC, as determined from radar+optical data, and differences in orbital element values obtained between the optical-only and radar+optical Yarkovsky solutions ($\Delta_{\rm o\text{-}only}$), and between the radar-only and radar+optical Yarkovsky solutions ($\Delta_{\rm r\text{-}only}$). The tiny deviations in the last column suggest that optical astrometry is not necessary to determine Icarus's orbit. Orbital elements include i, inclination with respect to J2000.0 ecliptic frame, Ω, longitude of the ascending node, ω, argument of pericenter, and M, mean anomaly at epoch.

Orb. element	radar+optical	$\Delta_{\rm o\text{-}only}$	$\Delta_{\rm r\text{-}only}$
a (au)	2.51055095174	1.6e-09	1.7e-10
e	0.63428478950	2.8e-10	6.6e-10
i (deg)	0.46970438367	6.6e-07	5.4e-08
Ω (deg)	128.36720962273	4.2e-05	2.2e-05
ω (deg)	274.68317363284	3.7e-05	2.2e-05
M (deg)	-76.29635453165	8.7e-07	6.4e-08

2.13.6 (2100) Ra-Shalom, (326290) Akhenaten, and (6239) Minos

These objects are those for which we found statistically different results for the drift rate when comparing between our analysis with modern data, and the analysis performed by Farnocchia et al. (2013b) using pre-2013 data. Our drift rates

do match Farnocchia et al. (2013b)'s rates when using the same observational intervals (Section 2.9).

We find a drift rate of Ra-Shalom $\langle da/dt \rangle = -2.25 \pm 0.77 \times 10^{-4}$ au/My, while Farnocchia et al. (2013b) found $\langle da/dt \rangle = -6.31 \pm 1.3 \times 10^{-4}$ au/My using pre-2013 data. 264 new optical observations have been added since 2013, resulting in a $\sim$20% increase in the size of the data set. While this is not a very large increase, the observations since 2013 also include the longest continuous set of observations ever taken for Ra-Shalom, of around five months, or $\sim$1/2 of an orbit (here we define a set of observations as continuous if there is no period spanning more than two weeks without at least one measurement within the set). Characterization of the Yarkovsky effect is aided by greater orbital coverage – therefore, we expect this modern set of observations to provide better constraints for this object than was previously possible.

For Akhenaten, we found a drift rate of $\langle da/dt \rangle = 7.38 \pm 8.9 \times 10^{-4}$ au/My, while Farnocchia et al. (2013b) found $\langle da/dt \rangle = -39.7 \pm 18.6 \times 10^{-4}$ au/My using pre-2013 data. Not only do these rates differ drastically in both magnitude and direction, but we also do not consider Akhenaten a Yarkovsky detection ($p = 0.11$). There have been fewer than 20 new observations of this object since 2012 (a $\sim$7% increase).

A clue for the sudden change in apparent drift rate for Akhenaten can be found by examining the goodness-of-fit metric using pre-2013 data, χ^2_{old}, and comparing with the metric when using all data, χ^2_{new} . In particular, after outlier rejection, the pre-2013 fit had $\chi^2_{\text{old}} = 171$ for 273 data points, while the fit using all data had $\chi^2_{\text{new}} = 151$ for 287 data points. In other words, with the additional data, χ^2 dropped significantly. This is a strong indicator that the difference in results between the two fits may be due to outlier rejection – namely, that a small number of points were found to be faulty measurements with the addition of new data. If this were the case, one would expect these points to fall near the outlier re-

jection threshold when fitting using pre-2013 data. We expect that these faulty observations may have been responsible for producing a false Yarkovsky detection.

We indeed found three observations of Akhenaten, taken on the same night from the same observatory (644 Palomar), that were rejected from the modern analysis, but avoided rejection in the analysis using pre-2013 data. The three points had residuals of 2.1σ, 1.9σ, and 2.7σ, respectively. Other than 8 observations from the prior night, they were the only measurements of Akhenaten over a ten year period. Removing these three points from the pre-2013 data and refitting resulted in a new goodness-of-fit of $\chi^2_{\text{old}} = 135$ (a $\sim$10% decrease), and resulted in a Yarkovsky drift rate of $\langle da/dt \rangle = 0.91 \pm 18.28 \times 10^{-4}$ au/My, which is consistent with a non-detection. Temporally isolated observations can have a disproportionate effect on a calculated drift rate. When these observations are also few in number, they render the perceived rate particularly susceptible to faulty astrometry.

Finally, for Minos we find a rate of $\langle da/dt \rangle = 7.98 \pm 3.54 \times 10^{-4}$ au/My, while Farnocchia found $\langle da/dt \rangle = -4.45 \pm 4.57 \times 10^{-4}$ au/My using pre-2013 data. The number of observations for this object has increased by over 50% since 2011, while the length of the observation interval has increased by 25%. The much larger data set explains our low p-value ($p = 10^{-5}$), and the shift in the measured effect.

2.13.7 (174050) 2002 CC19 and (1036) Ganymed

(174050) 2002 CC19 and (1036) Ganymed are the only two objects in our data set with unphysical ($\xi > 1$) Yarkovsky efficiency, with efficiencies of $\xi = 1.29$ and $\xi = 4.12$, respectively.

2002 CC19's high efficiency may be due to an incorrect diameter or density assessment – this object's spectral type is not known, so it was assigned a density of 2470 kg/m^3 (Section 2.10). If this object had a lower density, perhaps closer to

that typical of C-types, it would drive the ξ value to realistic levels.

Ganymed, however, is a different story. This object's high Yarkovsky efficiency is far too high to be explained by an uncertain density. However, the data for Ganymed stand out for several reasons. This object has measurements starting in 1924, and thus has one of the longest observational arcs we considered. It also has one of the largest sets of observations ($N = 5252$). Nugent et al. (2012) found $\langle da/dt \rangle = -6.6 \pm 1.5 \times 10^{-4}$ au/My, consistent with ours ($\langle da/dt \rangle = -5.0 \pm 1.3 \times 10^{-4}$ au/My), and devoted a section in their article to this anomalous case. Farnocchia et al. (2013b) determined a drift rate ($\langle da/dt \rangle = -6.1 \pm 1.6 \times 10^{-4}$ au/My) consistent with Nugent et al. (2012)'s and ours, but marked it as a potentially spurious detection, due to the unexpected strength of the drift rate relative to asteroid Bennu's rate scaled for diameter. Both Nugent et al. (2012) and Farnocchia et al. (2013b) suggested that this detection may be due to older, potentially faulty measurements introducing a false signal. Nugent et al. (2012) also explored the impact of an incorrect size or mass determination.

To examine the possibility that some of the Ganymed astrometry is faulty, we re-ran our Yarkovsky determination process after discarding observations prior to successively later starting dates (Figure 2.8). We found that the detected drift rate abruptly disappears if data prior to 1951 are discarded. This fact, combined with the unphysically large Yarkovsky efficiency required for Ganymed to have a drift rate $|\langle da/dt \rangle| > 1.5 \times 10^{-4}$ au/My, leads us to believe that this object represents either a false Yarkovsky detection, or a drift rate that has been artificially magnified by poor, early astrometry.

2.13.8 Binary asteroids

Our sample of objects include four confirmed binary asteroids – (1862) Apollo, (136993) 1998 ST49, (363599) 2004 FG11, and (385186) 1994 AW1. Binaries

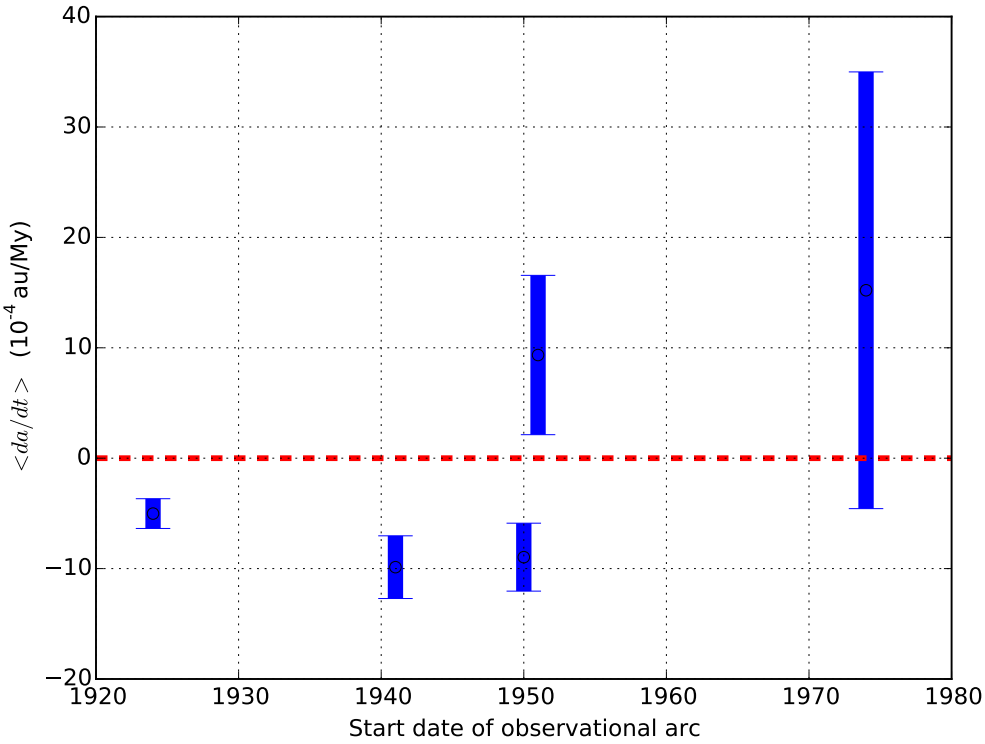

Figure 2.8: With a drift rate of $\langle da/dt \rangle = -5.0 \pm 1.3 \times 10^{-4}$ au/My, (1036) Ganymed appears to have an unphysical Yarkovsky efficiency of $\xi = 4.12$. We find that if observations prior to 1950 are discarded, the Yarkovsky effect for this object appears to abruptly disappear. Ganymed may have an unreliably determined drift rate due to faulty older astrometry.

present an opportunity to infer thermal properties from a Yarkovsky measurement, because tight constraints can be placed on both mass and obliquity for these objects (Section 2.14.3, Margot et al., 2015).

2.14 Discussion

2.14.1 Population-based detection verification

We have presented a statistical test which can be used to verify that a Yarkovsky detection is valid. However, one might still make the argument that the detections presented herein are merely due to statistical fluctuations. After all, the

Yarkovsky effect often results in extremely small variations in an orbit. Perhaps the detections we present are really just a side effect of adding an extra degree of freedom to the gravity-only dynamical model.

Given the number of objects in our samples, we can address these concerns by looking for verifications of our detections on a population level, in addition to object-by-object. One such verification is the correspondence between the measured $\langle da/dt \rangle$-vs-D inverse relationship, and the relationship predicted by the Yarkovsky theory (Section 2.12). It seems unlikely that a process which is merely fitting for statistical noise would generate the $1/D$ behavior that we expect *a priori*.

Another population-level analysis considers the distribution of spin poles of NEAs. We have already discussed how we measured the ratio of retrograde-to-prograde rotators in our sample (Section 2.11). We can also use the raw number of negative $\langle da/dt \rangle$ values compared to positive $\langle da/dt \rangle$ values to test the "statistical noise hypothesis". Namely, we can ask the following question: if our dynamical model, purportedly measuring a non-gravitational force, were instead merely overfitting for statistical noise, what would be the probability that we would have measured the number of retrograde rotators that we saw in our sample? In other words, what is the probability P of achieving a particular number m (or more) negatively-signed $\langle da/dt \rangle$ values in a population of N objects?

This question can be rephrased in terms of the probability P of of observing at least m heads after N coin flips, for a coin weighted with probability p. This can be answered using the binomial distribution,

$$P = 1 - B(m-1, N, p). \tag{2.16}$$

In our sample, we have $m = 114$ objects with a negative $\langle da/dt \rangle$ out of $N = 159$ objects total. To determine p, we first assume that the non-gravitational dynamical model *is* in fact overfitting for noise. In that case, the extraneous

parameter would not favor one sign or another – in other words, the distribution of $\langle da/dt \rangle$ values that are measured should have a median of 0, which would suggest $p = 0.5$.

Putting these values into Equation 2.16, we find $P = 2.2 \times 10^{-8}$. In other words, if the model were merely measuring statistical noise, the odds of finding the ratio of negatively-signed to positively-signed drift rates observed in our data set (or a ratio more extreme) is approximately 1 in 46 million. This extremely low value provides an *ab absurdo* refutation of the hypothesis that we are fitting for noise. Note that this probability was calculated with minimal assumptions about the nature of the underlying statistical noise – we need only assume some distribution with a median of $\langle da/dt \rangle = 0$.

2.14.2 The viability of Yarkovsky measurements

For those objects with previous Yarkovsky detections, we have compared results from two previous works (namely, Nugent et al. (2012) and Farnocchia et al. (2013b)) and found excellent agreement (Section 2.6). The general strength and consistency of the agreement when using roughly similar observation intervals (where we found disagreement on drift rates for only a single object) serves as a validation of the methods employed by all three groups. The agreement when we used all data available to us (where we found disagreement on drift rates for only five objects) speaks to the viability of measuring this small effect from astrometric measurements, because the measured rates are stable, even with the addition of new data.

Among this work and the two previous studies, at least three different orbital integration packages were used to perform the analyses, indicating robustness of the results against numerical implementations.

2.14.3 Interpreting ξ

We have found that within our sample of objects, typical Yarkovsky efficiencies lie between $0.06 - 0.29$ (Section 2.10). An in-depth interpretation of these values would require a full thermal model of each object. However, we can still provide insights by making the simplifying assumption that all absorbed photons are re-emitted equatorially. Then the ξ values can be interpreted relative to the obliquity and thermal properties of the object in one of three ways:

1. If all the reradiated photons were emitted at the same phase lag of $\phi = 90°$, then the obliquity would be $\gamma \sim \arccos \xi$. With these assumptions, our typical ξ values suggest a range of obliquities $73° < \gamma < 87°$ or $93° < \gamma < 107°$.

2. If the obliquity, γ, were $0°$ or $180°$, and all the reradiated photons were emitted at the same phase lag, then the phase lag would be $\phi \sim \arcsin \xi$. With these assumptions, typical efficiencies of $0.06 < \xi < 0.29$ imply phase lags of $3° < \phi < 17°$.

3. If the obliquity were $\gamma = 0°$ or $\gamma = 180°$, and the phase lag were $\phi = 90°$, then ξ could be interpreted as a measure of the distribution of photons that are emitted around ϕ.

Item (1) seems unlikely, given that we expect most of these objects to have obliquities near $0°$ or $180°$ – Hanuš et al. (2013) found that among a sample of 38 NEAs, more than 70% had $\gamma < 30°$ or $\gamma > 150°$. Item (2) is more palatable, and its applicability is protected by the cosine function's slow dropoff, which means that assuming very high or very low spin pole latitudes will introduce errors of less than 10% for those objects with $\gamma < 30°$ or $\gamma > 150°$.

Rubincam (1995) derived an expression for phase lag as a function of thermal inertia Γ of a body rotating at frequency ν, and found

$$\phi = \arctan\left(\frac{\Gamma\sqrt{\nu}}{\Gamma\sqrt{\nu} + \sqrt{32}\sigma T_0^3}\right), \tag{2.17}$$

where σ is the Stefan-Boltzmann constant, and T_0 is the temperature of the body when it is at a distance a from the Sun.

With a typical thermal inertia of $\Gamma = 200$ J m^{-2} s$^{-\frac{1}{2}}$ K^{-1} (Delbo et al., 2007), Equation 2.17 yields a phase lag of $\phi = 8.7°$ for a body orbiting at a distance of 1 au and rotating with a period of 4.5 hours. Assuming $\gamma = 0°$ or $\gamma = 180°$, our median Yarkovsky efficiency of $\xi = 0.12$ suggests $\phi = 7°$, which is in good agreement with the phase lag derived from thermal properties. With a more complete thermal model, it should be possible to relate any of the differences between these two determinations to the distribution of re-emitted photons (Item (3) above).

Better knowledge of γ and ξ will yield tighter constraints on thermal properties of NEAs. In particular, the obliquity and mass of binaries can be accurately determined through dynamical measurements of the system. Therefore, binaries with Yarkovsky estimates (Section 2.13.8) will likely provide the best constraints on thermal properties in the future.

2.14.4 Expected diameter dependence

Delbo et al. (2007) suggested that, due to a dependence between thermal inertia, Γ, and diameter, one might expect a flatter $\langle da/dt \rangle$ diameter dependence than predicted by a theory that disregards correlation between these parameters. In particular, they found that

$$\Gamma \propto D^{-p}, \tag{2.18}$$

where $p \sim 0.4$.

Delbo et al. (2007), citing Vokrouhlický (1999), wrote

$$\langle da/dt \rangle \propto D^{-1} \frac{\Theta}{1 + \Theta + 0.5\Theta^2}, \tag{2.19}$$

where

$$\Theta = \frac{\Gamma}{\epsilon\sigma(\sqrt{2}T_0)^3} \sqrt{\frac{2\pi}{P}}, \tag{2.20}$$

where σ is the Stefan-Boltzmann constant, P is the rotation period, ϵ is the thermal emissivity, and T_0 is the temperature of the body when it is at a distance a from the Sun.

Delbo et al. (2007) suggested that because the asymptotic behavior (i.e., $\Theta \gg 1$) of Equation 2.19 gives

$$\langle da/dt \rangle \propto D^{-1}\Theta^{-1}, \tag{2.21}$$

then, by relating Equations 2.18, 2.20, and 2.21, one would find

$$\langle da/dt \rangle \propto D^{-1+p} \propto D^{-0.6}. \tag{2.22}$$

However, few objects yield values for Θ such that Equation 2.21's pre-requisite of $\Theta \gg 1$ is appropriate. For example, typical objects in our sample have $P = 4.5$ hours and $T_0 = 300$ K. With typical thermal inertias in the range $\Gamma \sim 200 - 400$ J m^{-2} s$^{-0.5}$ K^{-1}, Equation 2.20 yields $\Theta \sim 1 - 2$. In fact, because Equation 2.19 peaks at $\Theta = 1.4$, the slope of the function with respect to Θ near $\Theta = 1 - 2$ is nearly 0, which suggests $\langle da/dt \rangle \propto D^{-1}\Theta^0 \propto D^{-1}$.

We find $\langle da/dt \rangle \propto D^{-1.05\pm0.06}$ (Section 2.12), which is consistent with the nominal theory.

2.14.5 Drift determination and radar ranging

While the Yarkovsky effect can be measured for objects with no radar ranging data, range astrometry aids greatly in improving the accuracy of drift determination. In particular, the number of distinct radar apparitions with range data correlates strongly with reduced uncertainty in an object's drift rate.

Of the 159 objects we analyzed, 53 had radar astrometry. Of these, 46 objects had range measurements. We examined the improvement in the Yarkovsky determination – quantified by $\sigma_{\rm o}/\sigma_{\rm r+o}$, or the ratio of the drift uncertainty without radar to that with radar – compared to the number of radar range apparitions for that object (Figure 2.9). We found that on average, each additional radar range apparition corresponds to an improvement in the precision by a factor of $\sim$1.6.

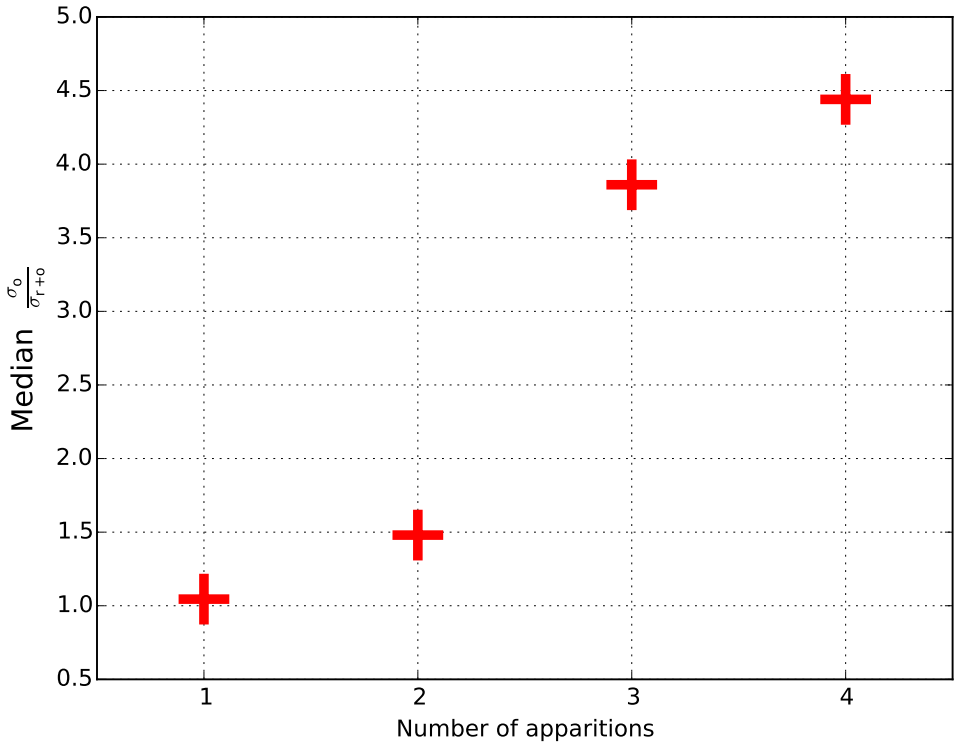

Figure 2.9: The ratio of the drift uncertainty without radar to that with radar, $\sigma_{\rm o}/\sigma_{\rm r+o}$, as a function of the number of radar apparitions during which ranging data were taken. The number of objects with radar range measurements were 24, 12, 7, and 3, for 1, 2, 3, and 4 apparitions, respectively.

2.15 Conclusion

With new astrometry and improved methods, we found a set of 159 NEAs with a measurable Yarkovsky drift. We found generally good agreement with previous

studies. Most NEAs exhibit Yarkovsky efficiencies in a relatively small (0–0.2) range. We verified the Yarkovsky drift rate's inverse dependence on asteroid size, and we estimated the ratio of retrograde-to-prograde rotators in the NEA population. In addition, we provided an estimate of the improvement in Yarkovsky determinations with the availability of radar data at multiple apparitions. Our results provide compelling evidence for the existence of a non-gravitational influence on NEA orbits.

2.16 Acknowledgements

We are grateful for the help and insights provided by Alec Stein regarding the statistical analyses of our data.

AHG and JLM were funded in part by NASA grant NNX14AM95G and NSF grant AST-1109772. Part of the work done here was conducted at Arecibo Observatory, which is operated by SRI International under a cooperative agreement with the National Science Foundation (AST-1100968) and in alliance with Ana G. Méndez-Universidad Metropolitana (UMET), and the Universities Space Research Association (USRA). The Arecibo Planetary Radar Program is supported by the National Aeronautics and Space Administration under Grant Nos. NNX12AF24G and NNX13AQ46G issued through the Near-Earth Object Observations program. This work was enabled in part by the Mission Operations and Navigation Toolkit Environment (MONTE). MONTE is developed at the Jet Propulsion Laboratory, which is operated by Caltech under contract with NASA. The material presented in this article represents work supported in part by NASA under the Science Mission Directorate Research and Analysis Programs.

CHAPTER 3

Asteroid 1566 Icarus's size, shape, orbit, and Yarkovsky drift from radar observations

3.1 Introduction

The first asteroid radar observations occurred at Haystack on June 13–15, 1968 (Pettengill et al., 1969) and Goldstone on June 14–16, 1968 (Goldstein, 1969), during a 16 lunar distance (LD) close approach of the object 1566 Icarus. Icarus' highly elliptical orbit (a = 1.08 au, e = 0.83, i = 22.8°) has it passing within radar detection range of the Earth only once every few decades. In modern times, the radar apparitions occurred in 1968, 1996, and 2015. Following the 1996 radar observations, Mahapatra et al. (1999) described Doppler spectra but did not report a detection in delay-Doppler images. Here, we report results from the 2015 Arecibo and Goldstone observations.

Although Icarus has only come within radar range of the Earth on three occasions in modern times, the long temporal separation of these events is invaluable for accurately constraining the orbit of the asteroid, as well as measuring long term variations in the orbit, such as those caused by the Yarkovsky effect. This is of particular importance because of Icarus' status as a Potentially Hazardous Asteroid (PHA), although the current Earth Minimum Orbit Intersection Distance (MOID) is 0.0344 astronomical units (au) or 13 LD.

In the following sections we describe the first radar-derived shape model for this object. We also discuss Icarus' unusual radar scattering profile, along with

potential explanations for its scattering behavior, and compare these radar-derived results to previous thermal and lightcurve results. In addition, we present a new orbit determination program which is capable of generating observational ephemerides for NEOs and detecting the Yarkovsky effect for both radar and optically observed objects. We use this program to derive the magnitude of long-term non-gravitational forces acting on Icarus.

3.2 Observations of 1566 Icarus

Table 3.1: Pre-observational information generated for 1566 Icarus. Signal-to-noise ratio (SNR) calculations assume nominal transmitter power, but equipment problems reduced the available transmitter power at Arecibo Observatory (see text).

Date (UTC)	RA (deg)	Dec (deg)	Distance (au)	SNR/run	Observatory	Band
2015-06-13 13:14-06:01	106	+63	0.072	8	Goldstone	X
2015-06-14 14:34-07:58	137	+64	0.061	13	Goldstone	X
2015-06-16 20:00-09:06	190	+42	0.054	22	Goldstone	X
2015-06-17 22:52-01:18	200	+29	0.059	475	Arecibo	S
2015-06-18 23:04-01:50	207	+17	0.068	290	Arecibo	S
2015-06-19 23:31-01:50	211	+8	0.080	165	Arecibo	S
2015-06-21 00:08-01:30	215	+1	0.093	98	Arecibo	S

Table 3.2: Radar observations of asteroid 1566 Icarus. The first column indicates the telescope: Arecibo (A) or Goldstone (G). UT Date is the universal-time date on which the observation began. MJD is the corresponding modified Julian date. Eph is the ephemeris solution number used. RTT is the round-trip light time to the target. P_{tx} is the transmitter power. Baud is the length of each code element of the pseudo-random code used for imaging; it dictates the range resolution. Spb is the number of complex samples per baud giving a pixel height of baud/spb; cw data are typically sampled at a rate of 12.5 kHz. Res is the frequency resolution of the processed data. Code is the length (in bauds) of the pseudo-random code used. The timespan of the received data is listed by the UT start and stop times. Runs is the number of completed transmit-receive cycles.

Tel	UT Date	MJD	Eph	RTT	P_{tx}	Baud	Spb	Res	Code	Start-Stop	Runs
	yyyy-mm-dd			s	kW	μs		Hz		hhmmss-hhmmss	
G	2015 Jun 13	57186	s82	70	411	cw		2.0	none	234028-235826	8
			s82		412	10	1	24.6	127	000615-001914	6
			s82		408	11	1	22.4	127	002354-004359	9
			s84		416	11	1	22.4	127	004605-005642	5
			s84		408	1	1	1.0	1023	010105-013038	13
G	2015 Jun 14	57187	s90	61	410	cw		0.5	none	232137-234306	11
			s90		410	10	1	24.6	127	234643-235146	3
			s90		394	0.5	1	3.8	255	235736-001047	7

Table 3.2, continued

Tel	UT Date	MJD	Eph	RTT	P_{tx}	Baud	Spb	Res	Code	Start-Stop	Runs
	yyyy-mm-dd			s	kW	μs		Hz		hhmmss-hhmmss	
G	2015 Jun 16	57189	s92	54	335	10	1	24.6	127	224941-225410	3
			s92		397	0.5	1	0.5	255	230029-232821	16
			s92		404	cw		0.5	none	233236-014530	73
			s92		396	0.5	1	0.5	255	014958-032952	55
A	2015 Jun 17	57190	u01	59	273	cw		0.3	none	233700-235711	7
			u01		249	0.1	2	0.3	65535	000256-002248	10
			u01		519	0.2	4	0.3	65535	004135-005943	6
A	2015 Jun 18	57191	u01	67	596	cw		0.4	none	232250-233726	7
			u01	68	634	0.5	1	0.5	8191	234128-013824	52
A	2015 Jun 20	57193	u01	80	622	cw		1.0	none	002652-004924	9
			u01		664	1	2	1.0	8191	005857-013453	14
A	2015 Jun 21	57194	u01	93	642	cw		1.5	none	004449-010517	7

Observations of Icarus were conducted from 2015 June 13 to June 16 at the Goldstone Observatory in California, and from 2015 June 17 to June 21 at the Arecibo Observatory in Puerto Rico. During the Arecibo observations, the signal-to-noise ratio (SNR) decreased by roughly a factor of 2 each day (Table 3.1).

At the Arecibo Observatory, continuous wave (CW) and delay-Doppler data were taken at the S-band transmitter's nominal frequency of 2380 MHz. CW data were taken on each day of observations. Delay-Doppler data were taken on the first three days of observations. The baud length of the delay-Doppler data, which controls the range resolution, was adjusted each day as the Icarus–Earth distance increased, with 0.1 μs and 0.2 μs bauds (corresponding to 15 m and 30 m range resolution, respectively) used on June 17, 0.5 μs (75 m) on June 18, and 1.0 μs (150 m) on June 19. The CW data were reduced with frequency resolutions ranging from 0.25 to 1.5 Hz, depending on that day's SNR. The delay-Doppler data were reduced with frequency resolutions ranging from 0.30 Hz to 1 Hz.

During data-taking, transmission power was limited to $\sim$25% of nominal (278 kW) on the first day and $\sim$60% (600 kW) on the remaining days, due to problems with the transmitter klystrons (Table 3.2). This power limitation reduced the overall data quality taken at Arecibo.

At Goldstone, CW and delay-Doppler data were taken at the X-band transmitter's nominal frequency of 8560 MHz. Each day began with CW observations, followed by coarse (10 or 11 μs baud) ranging and 1 μs or 0.5 μs imaging. The primary purpose of coarse ranging observations is to improve the quality of an object's ephemeris. The ranging measurements taken at Goldstone were the first ever ranging observations of Icarus. The CW data were reduced with frequency resolutions ranging from 0.5 to 2 Hz, depending on that day's SNR. The delay-Doppler data were reduced with frequency resolutions ranging from 0.50 Hz to 3.8 Hz.

3.3 Methods

3.3.1 Shape analysis

3.3.1.1 Radar scattering properties

In order to determine a shape from radar images, one must simultaneously fit for the shape, spin, and radar scattering properties of the surface and sub-surface of the object. Radio waves incident on the surface of an object will scatter over a variety of angles with a range of associated powers, and the relationship between scattering angle and back-scattered power determines the object's specularity. This scattering behavior can be described by $\frac{d\sigma}{dA}(\theta)$, or the differential radar cross section per surface element area, as a function of the incidence angle θ (Evans & Hagfors, 1968).

The `shape` software package (Hudson & Ostro, 1994; Magri et al., 2007c) can estimate $\frac{d\sigma}{dA}$ by fitting for the parameters of this function along with an object's surface shape. We found that the Icarus data were well fit by either a two-component cosine scattering law (Appendix D) or a 'hagfors' scattering law. For the analysis performed in this paper, we chose to use a 'hagfors' scattering law, which is defined as

$$\frac{d\sigma}{dA} = H(\theta_0 - |\theta|) \times \frac{RC}{2}(\cos^4\theta + C\sin^2\theta)^{-\frac{3}{2}} \tag{3.1}$$

where R and C are tunable parameters of the scattering law, $H(x)$ is the Heaviside step function, and θ_0 is a fixed angular cutoff value. This scattering law is the standard Hagfors Law (Hagfors, 1964) with an angular cutoff.

3.3.1.2 Shape and spin pole determination

Shape analysis was performed using the `shape` software package with the fitting algorithm described in Greenberg & Margot (2015). The shape was modeled

with a triaxial ellipsoid during all stages of the fitting process. Attempts to utilize a more complex model (e.g., a spherical harmonic model) resulted in no changes being applied during the minimization process when starting from a best-fit ellipsoid, which suggests that the data quality is not high enough to support a more complex model. The spin period was fixed at 2.273 hours (Harris, 1998; Gehrels et al., 1970).

Our analysis used both continuous-wave and imaging data. Initial tests showed that including imaging data taken after the first night of Arecibo observations (June 17) had no effect on the fit. This result is to be expected because the lower SNR (Table 3.1 and Figure 3.2) for the later nights necessitated relatively low-resolution images to be taken. Therefore, all subsequent fits were performed only with imaging data taken at 0.1 μs and 0.2 μs resolution on the first night of Arecibo observations. Similarly, the Goldstone delay-Doppler images were not included in the fits due to low resolution and SNR. All CW data from both Arecibo and Goldstone were used.

The initial shape model was chosen as the ellipsoid representation of a sphere with a radius of 0.63 km (Harris, 1998). We explored a variety of initial conditions for the spin pole using a grid of evenly spaced positions, with neighboring points $\sim$15° apart. During this grid search, the spin pole positions were allowed to float along with the axial ratios of the ellipsoid and scattering parameters. Simultaneous fitting of both size and spin pole parameters was made possible due to previous modifications made to the `shape` software (Greenberg & Margot, 2015).

We performed a χ^2 analysis to place constraints on the possible spin pole orientations. χ^2 is the element-wise sum of squared differences between a model's predicted CW power or delay-Doppler image pixel value, and the corresponding measurement. Specifically, after running the grid search described above, we

calculated the quantity $\Delta\chi_i$ for each of the initial grid positions, where

$$\Delta\chi_i \equiv \frac{\chi_i^2 - \chi_{\rm min}^2}{\sqrt{2k}}, \tag{3.2}$$

where χ_i^2 is the χ^2 associated with the $i^{\rm th}$ grid position after convergence, $\chi_{\rm min}^2$ is the lowest χ^2 achieved across all grid positions, and k is the number of degrees-of-freedom for the fit. $\Delta\chi_i$ can be thought of as the distance in χ^2-space between the $i^{\rm th}$ grid position and that of the best fit, in units of standard deviations of the χ^2 distribution. Grid positions with $\Delta\chi_i < 1$ yield results that are statistically indistinguishable from those of the best fit, and thus represent positions with potentially valid shape, spin pole, and scattering behavior solutions.

3.3.2 Orbit Determination

Smearing of radar images in the range dimension occurs when the object's range drift is not properly taken into account. Provided that the direction and magnitude of the target's motion is known prior to taking data, this range drift can be compensated for entirely at the data-taking stage by delaying the sampling clock appropriately. If there are residual errors due to imperfect knowledge of the object's orbit, additional image corrections at the pixel level are necessary before summing individual images, which is suboptimal (Ostro, 1993). For this reason, radar observers place a high priority on securing an accurate knowledge of the object's trajectory before the observations or during the first few minutes of the observations.

Therefore, radar observations require the generation of ephemerides that encode the knowledge of the object's position and velocity. Traditionally we have used the On-site Orbit Determination Software (OSOD) (Giorgini et al., 2002) to generate ephemerides for radar observations. For observations of Icarus, AHG, JLM, and AKV wrote a new ephemeris-generating program called the Integration and Determination of Orbits System (IDOS). Central to IDOS' operation is the

Mission analysis, Operations, and Navigation Toolkit Environment (MONTE), a powerful tool developed by the Jet Propulsion Laboratory (JPL) for a variety of space-related science and aeronautical goals (Evans et al., 2016). MONTE has been used as an integral tool for trajectory design and spacecraft tracking of most modern NASA missions, and has therefore been thoroughly tested in this context. More recently, MONTE has also been tested as a scientific tool for mapping the internal structure of Mercury through gravitational field determination (Verma & Margot, 2016).

IDOS utilizes MONTE's built-in orbital integrator, DIVA. DIVA uses Adams's method with variable timesteps to integrate the differential equations of motion. DIVA can account for gravitational perturbations from any set of masses, as well as arbitrary accelerations, including non-gravitational forces. For the analyses performed in this paper, we considered the major planets and 24 of the most massive minor planets (Folkner et al., 2014) as gravitational perturbers. During close approaches, DIVA can take into account a detailed description of a perturber's gravitational field. DIVA also considers general relativistic effects during orbital integration.

IDOS also uses MONTE's built-in residual minimization capabilities. The underlying algorithm is based on a Kalman filter (Kalman, 1960) and the work of Bierman (1977).

IDOS can process both optical and radar astrometric measurements. Optical measurements are automatically downloaded from the Minor Planet Center (MPC) database (Minor Planet Center, 2017). Measurements are corrected for star catalog bias based on the reference catalog and sky location, and weighted based on the reference catalog, observatory, observation type, and date. Both debiasing and weighting are calculated using the methods described in Farnocchia et al. (2015).

3.3.3 Yarkovsky force model

The Yarkovsky effect (e.g., Peterson, 1976; Vokrouhlický & Farinella, 1998; Vokrouhlický et al., 2000; Rubincam, 2000) is a secular thermal effect that causes an affected object's semi-major axis to change over time, on the order of 10^{-4} au/My for a km-size object. By equating this thermal acceleration $\ddot{r}$ with the change in momentum per unit mass due to incident radiation (Appendix B), one finds that

$$\ddot{\vec{r}} = \xi \, \frac{3}{8\pi} \, \frac{1}{D\rho} \, \frac{L_\odot}{c} \, \frac{X_{\hat{p}}(\phi)\vec{r}(t)}{||\vec{r}(t)||^3}, \tag{3.3}$$

where $\vec{r}(t)$ is the heliocentric radial vector for the object at time t, $\hat{p}$ is the unit spin-axis vector, ϕ is the phase lag, $L_\odot$ is the luminosity of the sun, c is the speed of light, and $X_{\hat{p}}(\phi)$ is the rotation matrix about $\hat{p}$. ξ is an efficiency factor.

IDOS models the Yarkovsky effect by applying this acceleration at every integration time step. The diameter D and density ρ are assumed to be 1 km and 1 g cm^{-3} unless more specific values can be determined for the object. We note that these assumptions do not ultimately have any effect on the final reported value of $\langle da/dt \rangle$ (Section 3.3.4.1) —any inaccuracies in assumptions concerning ρ and D are absorbed by the efficiency factor ξ.

Icarus's semi-major axis exhibits substantial variations as a function of time due to close planetary encounters, including the 1968 and 2015 Earth encounters. Our modeling of the Yarkovsky effect considers all the gravitational dynamics but adds a non-gravitational acceleration to the dynamical model.

3.3.4 Yarkovsky determination

3.3.4.1 Measuring Yarkovsky drift

As discussed in Section 3.3.2, we used our orbit determination software to detect and determine the magnitude of the Yarkovsky effect on Icarus. Both positive and negative values for ξ were considered, allowing for the possibility that the object

is either a retrograde or prograde rotator, respectively.

We recorded a goodness-of-fit metric, χ^2, where

$$\chi^2 = \sum_{i=1}^{N} \frac{(E_i - O_i)^2}{\sigma_i^2}, \tag{3.4}$$

where E_i, O_i is the expected and observed value, respectively, for the i^{th} astrometric measurement, and σ_i is the measurement uncertainty for that observation, and N is the number of observations. These measurements included both radar and optical astrometry.

We then identified the best-fit ξ value and assigned one-standard-deviation error bars corresponding to $\xi = \xi(\chi^2_{min} + 1)$, as described in Press et al. (1992).

3.3.4.2 Transverse acceleration to orbit-averaged drift

As discussed in Section 3.3.4.1, our orbit determination software provides the capability to model the magnitude of the instantaneous acceleration imparted on a rotating object due to anisotropic reradiation of absorbed sunlight. However, for the purpose of comparing our results with those extant in the literature, it is useful to convert between this quantity and the orbit-averaged change in semi-major axis, $\langle da/dt \rangle$.

We note that because there is an arbitrary scaling factor (ξ) in our Yarkovsky force model (Equation 3.3), we can select model parameters that maximize the transverse component of the acceleration without prejudice. Therefore, we set the spin pole orientation parallel to the orbital pole and the phase lag ϕ to $-90°$. Neither of these choices affect the final estimated value of $\langle da/dt \rangle$ (Section 3.4.5).

To find $\langle da/dt \rangle$, we first considered the instantaneous change in semi-major axis due to some small perturbing transverse force, as given by (Burns, 1976)

$$\frac{da}{dt} = \frac{2}{\sqrt{GM_\odot}} a^{\frac{3}{2}} (1 - e^2)^{-\frac{1}{2}} (1 + e \sin \theta_f) \frac{T}{m}, \tag{3.5}$$

where G is the gravitational constant, $M_\odot$ is the mass of the central body, e and a are the orbital eccentricity and semi-major axis, respectively, θ_f is the true anomaly at a specific epoch, T is the perturbing transverse force, and m is the mass of the orbiting body.

Substituting equation (3.3) for $\frac{T}{m}$, and expressing $r(t)$ in terms of $\theta_f(t)$ via

$$r(\theta_f) = \frac{a(1-e^2)}{1+e\cos\theta_f}, \tag{3.6}$$

gives the instantaneous change in semi-major axis as a function of orbital parameters and the Yarkovsky acceleration scaling parameter ξ

$$\frac{da}{dt} = \xi\frac{3}{4\pi}\frac{L_\odot}{c\sqrt{GM_\odot}}\frac{1}{D\rho}\frac{1}{\sqrt{a}}\frac{(1+e\sin\theta_f)(1+e\cos\theta_f)^2}{(1-e^2)^{\frac{5}{2}}}. \tag{3.7}$$

Averaging equation (3.7) over one full orbit yields

$$\langle da/dt\rangle = \xi\frac{\hat{\alpha}}{\sqrt{a}}\frac{3L_\odot}{4\pi c\sqrt{GM_\odot}}\frac{1}{D\rho}, \tag{3.8}$$

where

$$\hat{\alpha} = \frac{1}{2\pi}\int_0^{2\pi}\frac{(1+e\sin\theta_f)(1+e\cos\theta_f)^2}{(1-e^2)^{\frac{5}{2}}}dM \tag{3.9}$$

is a quantity that depends only on orbital parameters and the true anomaly θ_f is a function of the mean anomaly M.

Noting that $\hat{\alpha} = 1$ when $e = 0$, we can plug nominal values into equation (3.8), yielding

$$\begin{aligned}\langle da/dt\rangle = 1.45\ \times\ \hat{\alpha}&\left(\frac{1\text{ au}}{a}\right)^{\frac{1}{2}}\left(\frac{\xi}{0.01}\right)\\ &\left(\frac{1\text{ km}}{D}\right)\left(\frac{1\text{ g cm}^{-3}}{\rho}\right)\times\frac{10^{-4}\text{ au}}{\text{Myr}}.\end{aligned} \tag{3.10}$$

3.3.4.3 Detection verification

Once a $\langle da/dt\rangle$ has been estimated, it is necessary to verify whether the measured Yarkovsky effect signal is sufficiently strong to be considered a true detection.

To determine this, we performed an *analysis of variance* to compare our best-fit Yarkovsky model ($\xi = \xi_b$) to a model in which no Yarkovsky effect was present ($\xi = 0$).

The analysis of variance was designed to compare the goodness-of-fit between two models with different number of model parameters, a task which is otherwise not straightforward. We followed the methods described in Mandel (1964). Specifically, we calculated the test-statistic

$$F = \frac{\kappa_\delta}{\kappa_Y} \tag{3.11}$$

where

$$\kappa_\delta = \frac{\sum_{i=1}^{N}(\frac{E_{0,i}-O_i}{\sigma_i})^2 - \sum_{i=1}^{N}(\frac{E_{\xi_b,i}-O_i}{\sigma_i})^2}{m_Y - m_0} \tag{3.12}$$

and

$$\kappa_Y = \frac{\sum_{i=1}^{N}(\frac{E_{\xi_b,i}-O_i}{\sigma_i})^2}{N - m_Y}. \tag{3.13}$$

Here, $E_{0,i}$ is the simulated i^{th} observation assuming gravity only ($\xi = 0$), $E_{\xi_b,i}$ is the simulated i^{th} observation assuming a Yarkovsky model with $\xi = \xi_b$, O_i is the i^{th} observation and σ_i is the measurement uncertainty for that observation, N is the number of observations, and m_Y, m_0 are the number of free parameters in the Yarkovsky model ($m_Y = 7$) and gravity-only model ($m_0 = 6$), respectively.

We then calculate the value

$$p = \int_{x=F}^{x=\infty} f_{(m_Y-m_0,N-m_Y)}(x)dx, \tag{3.14}$$

where $f_{(m_Y-m_0,N-m_Y)}$ is the F-distribution probability density function with $m_Y - m_0$ and $N - m_Y$ degrees of freedom. The p-value serves as a metric for testing the null hypothesis that the ξ variable is superfluous. In other words, a small p-value indicates that it would be implausible for us to record the astrometry that was actually observed in a gravity-only universe. Small p-values suggest that a non-gravitational component to the acceleration is required. For instance, one could choose $p < 0.003$ as a threshold to reject the null hypothesis. This criterion

approximately corresponds to a 3-standard-deviation detection. We will see that we can reject the null hypothesis for Icarus with much higher confidence than $p < 0.003$.

3.4 Results

3.4.1 Cross-section and polarization properties

The circular polarization ratio $\mu_{\,\mathrm{C}}$ is defined as the ratio of the cross-section in the same sense circular polarization (SC) as that transmitted to that in the opposite sense circular polarization (OC). $\mu_{\,\mathrm{C}}$ serves as a measure of the surface roughness at size scales comparable to the wavelength of the transmitted light. The arithmetic average $\mu_{\,\mathrm{C}}$ for Icarus, as calculated from the Arecibo (S-Band) CW observations, was $\mu_{\,\mathrm{C}} = 0.18$ with a standard deviation of 0.05 (Figure 3.1 and Table 3.3). Some of the observed variations may be due to non-uniform scattering properties over the asteroid's surface.

Icarus' total radar cross-section ($\sigma_{\,\mathrm{T}}$), defined as the sum of the OC and SC cross-sections, was measured for each day of observations using CW data. The arithmetic average $\sigma_{\,\mathrm{T}}$ as calculated from the Arecibo CW observations is 0.030 km^2 with a standard deviation of 0.007 km^2.

The values for circular polarization ratio and total radar cross-section, as calculated from the Goldstone (X-band) CW observations, are $\mu_{\,\mathrm{C}} = 0.33$ (standard deviation 0.05) and $\sigma_{\,\mathrm{T}} = 0.069$ km^2 (standard deviation 0.041 km^2). Mahapatra et al. (1999) had previously reported $\mu_{\,\mathrm{C}} = 0.48 \pm 0.04$ at X-band.

There are two possible explanations for the discrepancies in polarization ratios at S-band and X-band. First, the low SNR of the Goldstone observations may affect the determination of the polarization ratios because receiver noise may inadvertently contribute to the SC cross-section estimates, artificially raising the

μ_C values. For this reason, we believe that the Arecibo values are more accurate due to the much higher SNR (Table 3.1 or Figure 3.2). Second, it is also possible that Icarus' cross-sections and polarization ratios have a wavelength dependence. If so, the difference between the Arecibo and Goldstone μ_C values would suggest that Icarus' surface is smoother at S-band wavelength (12.6 cm) size scales than at X-band wavelength (3.5 cm).

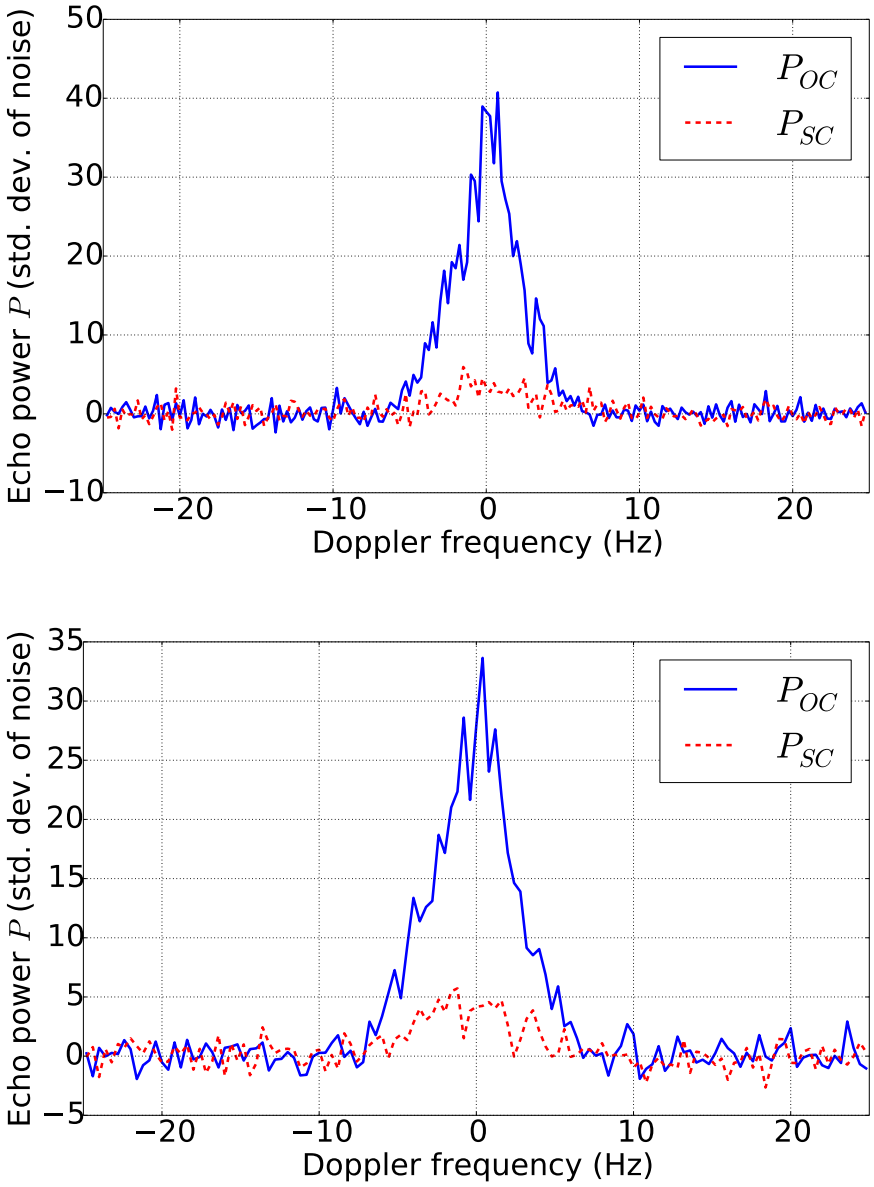

Figure 3.1: Echo spectra of 1566 Icarus obtained at Arecibo on 2015 June 17 at 0.25 Hz resolution (top) and June 18 at 0.4 Hz resolution (bottom).

Table 3.3: Observed radar cross-sections (σ) and corresponding radar albedos ($\hat{\sigma}$) calculated on the basis of projected areas derived using our best-fit model. The Arecibo S-band $\sigma_{\mathrm{OC,\,SC}}$ values have uncertainties of $\sim$ 20% due to uncertainties in the telescope gain and total power transmitted. Most of these absolute calibration errors cancel out when computing μ_{C}, for which we estimate uncertainties of $\sim$ 10%. One of us (SPN) calculated the Goldstone X-band $\sigma_{\mathrm{OC,\,SC}}$ and μ_{C} values. The Goldstone $\sigma_{\mathrm{OC,\,SC}}$ values have uncertainties of 35% due to uncertainties in telescope pointing and other calibration errors, whereas the μ_{C} uncertainty is $\sim$ 30%. Latitude (lat) and longitude (lon) indicate the location of the sub-radar point, given in body-centric coordinates at the midpoint of the observation arc, with a prime meridian defined by the body's long axis. The range of sub-radar point longitudes sampled over the duration of these observations, i.e., the rotational smear, is listed in the last column.

Date (UTC)	σ_{OC} (km^2)	σ_{SC} (km^2)	σ_{T} (km^2)	μ_{C}	$\hat{\sigma}_{\mathrm{T}}$	Band	lat (deg)	lon (deg)	rot. smear (deg)
2015 Jun 13 23:40-23:58	0.1151	0.0494	0.1645	0.429	0.111	X	-40.5	258	48
2015 Jun 14 23:22-23:43	0.0599	0.0192	0.0791	0.320	0.051	X	-44.3	94	55
2015 Jun 16 23:33-01:45	0.0361	0.0115	0.0476	0.318	0.031	X	-41.3	191	348
2015 Jun 17 23:37-23:56	0.0364	0.0054	0.0418	0.149	0.028	S	-33.5	81	50
2015 Jun 18 23:23-23:36	0.0218	0.0042	0.0260	0.194	0.018	S	-25.4	267	34
2015 Jun 20 00:27-00:48	0.0201	0.0051	0.0252	0.256	0.018	S	-18.5	246	55
2015 Jun 21 00:45-01:04	0.0224	0.0031	0.0255	0.137	0.018	S	-13.5	357	50

3.4.2 Bandwidth

The observed bandwidth, as measured from the CW data, reached a minimum on the second day of observations, which is consistent with the sub-radar latitude reaching an extremum on that date (Table 3.4) if the object is approximately spheroidal.

The predicted limb-to-limb bandwidth — which can be calculated from the expression

$$B_{LL} = \frac{4\pi D \cos\delta}{\lambda P}, \tag{3.15}$$

where P is the object's rotational period, δ is the latitude of the sub-radar point, and λ is the wavelength of the transmitted signal — does not appear to agree with observations. As we will discuss in detail in Section 3.5, this object's high specularity means that under certain observing conditions, the echo signal may contain very little power from surface regions with high incidence angles ($\theta_{inc} \gtrsim 45°$), a fact already alluded to by Pettengill et al. (1969) and Goldstein (1969). As a result, the calculated limb-to-limb bandwidth does not correspond to the observed bandwidth, but the bandwidth measured at a level 1-standard-deviation above the noise does correspond to the bandwidth calculated from the shape model at the same signal strength.

3.4.3 Shape and spin pole determination

In Figure 3.3, we report solutions for the spin pole orientations that satisfy $\Delta\chi_i \leq \frac{1}{3}$ (Section 3.3.1.2). After determining these solutions, we ran a clustering analysis based on the nearest-neighbor algorithm (Altman, 1992) to group solutions with spatially correlated spin pole positions. Figure 3.3 shows cluster membership with coloring. The mean three-dimensional Cartesian position of these clusters, projected onto the celestial sphere, are indicated with black crosses, and the 1- and 2-standard-deviation uncertainty regions in cluster mean position are indicated

Table 3.4: A comparison of the observed bandwidths at 1-standard-deviation above the noise ($B_{>1,O}$), to that predicted by our best-fit model ($B_{>1,P}$). We attribute the discrepancy between the observed $B_{>1,O}$ and the predicted limb-to-limb bandwidth (B_{LL}) to the highly specular surface of 1566 Icarus, which, at low SNR, prevents the observer from receiving sufficient signal from high-incidence-angle regions. On the other hand, the $B_{>1,P}$ as predicted by the model matches the observed $B_{>1,O}$, with the exception of June 16. Bandwidth uncertainty was calculated as three times the frequency bin size. All Goldstone bandwidths have been converted into S-band Hz for ease of comparison.

	Observed	**Predicted**	
Date (UTC)	$B_{>1,O}$ (Hz)	B_{LL} (Hz)	$B_{>1,P}$ (Hz)
2015 Jun 13 23:40-23:58	10.4±1.7	12.7	9.5
2015 Jun 14 23:22-23:43	7.8±0.4	11.9	8.5
2015 Jun 16 23:33-01:45	12.8±0.4	14.2	10.2
2015 Jun 17 23:37-23:56	11.8±0.8	16.5	12.0
2015 Jun 18 23:23-23:36	13.3±1.2	18.1	12.8
2015 Jun 20 00:27-00:48	14.2±0.8	19.0	14.0
2015 Jun 21 00:45-01:04	14.5±4.5	19.4	15.0

with dashed circles. Note that projection effects make these regions appear non-circular.

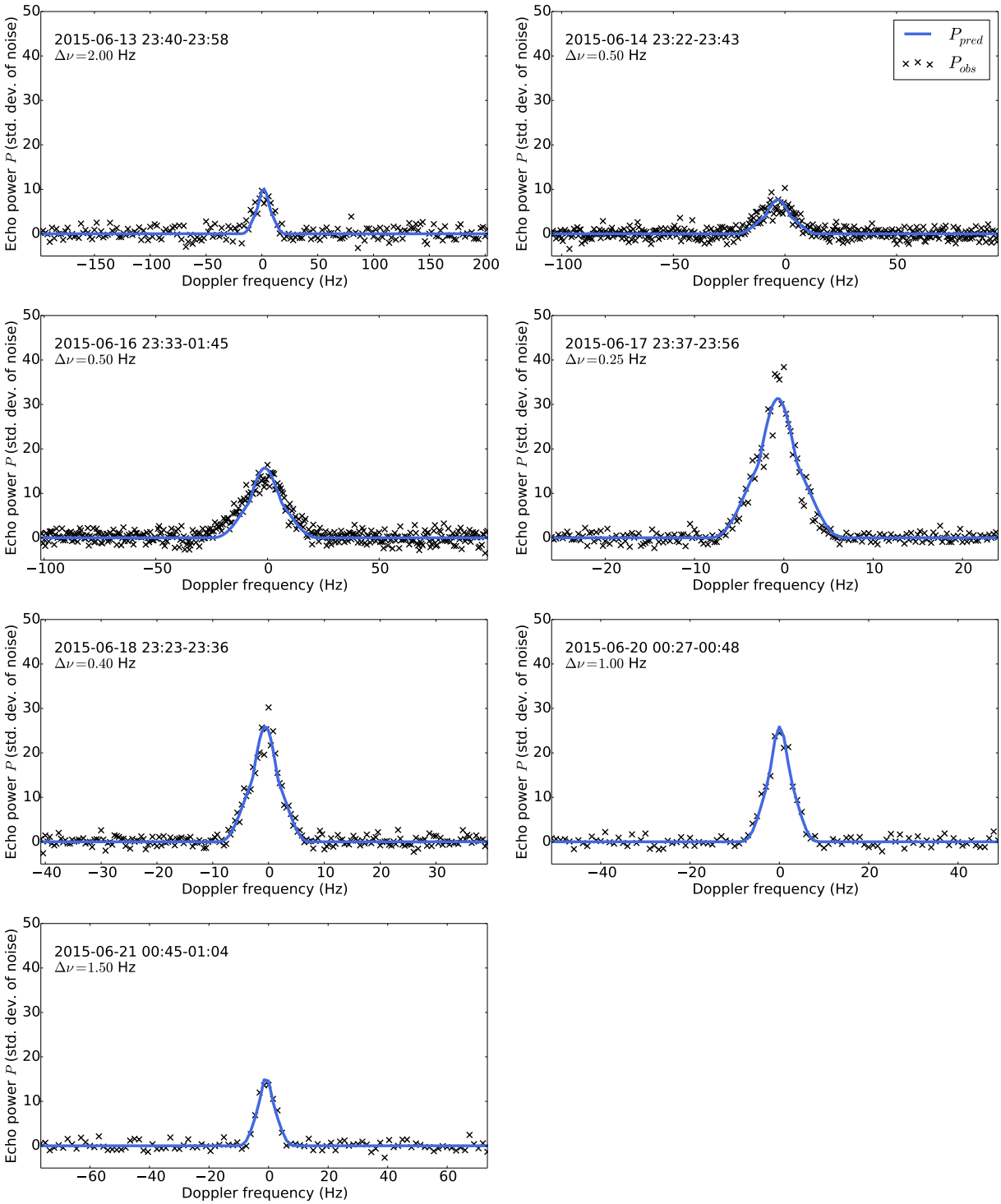

Figure 3.2: Continuous-wave observations of 1566 Icarus on each day of observation. The first three sets of data were taken from Goldstone in the X-band, while the remaining four sets were taken at Arecibo in the S-band. Each set represents the summed observed powers from the corresponding day, compared to the summed predicted powers from our best-fit model. $\Delta\nu$ is the frequency resolution.

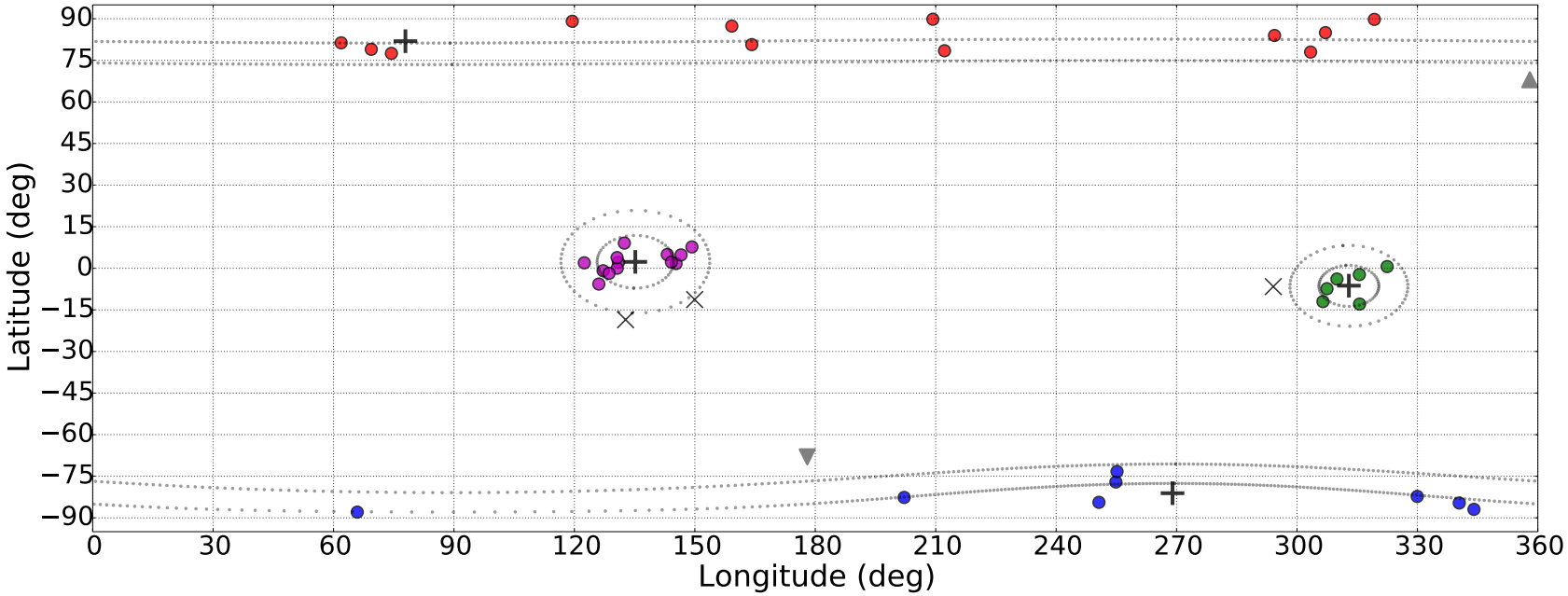

Figure 3.3: Results of our search for Icarus' spin axis orientation, in the ecliptic frame of J2000. We fit ellipsoids to the data with trial values of the spin axis orientation that were evenly distributed across the celestial sphere (Deserno, 2004) with an initial spacing of 15°. The spin pole location was allowed to float during these fits. Solutions with $\Delta\chi < \frac{1}{3}$ (Section 3.3.1.2) were plotted as circles and colored according to cluster membership. Black crosses indicate a cluster's mean position, whereas dotted lines show the 1- and 2-standard-deviation uncertainty region in mean cluster position. Black x's indicate solutions that did not fall within any cluster with more than one member. Triangles show the location of the orbital poles.

Table 3.5 shows the two possible pairs of spin pole positions, labeled by their color (as seen in Figure 3.3). Each pair's member clusters (the purple and green clusters, and the red and blue clusters) are approximate antipodes of their partner.

The associated ellipsoid axis diameters and scattering parameters (Section 3.3.1.1) are also listed in Table 3.5. The uncertainty given for each parameter was calculated as the standard deviation in said parameter among members of the corresponding cluster. Because the members of each cluster are not strictly independent samples, these standard deviations may be underestimates of true uncertainties, and do not account for potential systematic errors.

Table 3.5: Possible spin poles (ecliptic coordinates) and corresponding size and roughness values. Our adopted solution (Section 3.5) is shown in bold, and represents a moderately flattened spheroid.

Cluster color	**Spin pole**		**Specularity**	**Ellipsoid axis diameters**			**Equiv. diameter**
	λ	β	C	$2a$ (km)	$2b$ (km)	$2c$ (km)	$D_{\rm eq}$ (km)
Purple	$135^\circ \pm 10^\circ$	$4^\circ \pm 10^\circ$	12.9 ± 2.1	$1.49 \pm .15$	$1.53 \pm .16$	$1.18 \pm .13$	$1.39 \pm 10\%$
Green	$313^\circ \pm 10^\circ$	$-6^\circ \pm 10^\circ$	13.9 ± 0.7	$1.64 \pm .12$	$1.59 \pm .12$	$1.18 \pm .27$	$1.45 \pm 13\%$
Red	$78^\circ \pm 10^\circ$	$82^\circ \pm 10^\circ$	13.3 ± 2.0	$1.65 \pm .19$	$1.64 \pm .19$	$1.38 \pm .20$	$1.55 \pm 13\%$
Blue	$\mathbf{270^\circ \pm 10^\circ}$	$\mathbf{-81^\circ \pm 10^\circ}$	$\mathbf{13.8 \pm 1.4}$	$\mathbf{1.61 \pm .15}$	$\mathbf{1.60 \pm .17}$	$\mathbf{1.17 \pm .39}$	$\mathbf{1.44 \pm 18\%}$

The parameters listed in Table 3.5 show the specularity parameter C (Equation 3.1) for the two pairs of spin pole solutions. All solutions are consistent with a Hagfors C value of 13. The Hagfors formalism assumes that the surface roughness has been smoothed with a wavelength-scale filter. In this formalism, the C value corresponds to the root-mean-square slope (S_0) of a gently undulating surface at scales greater than the wavelength. From the expression

$$S_0 = \frac{1}{\sqrt{C}}, \tag{3.16}$$

we find that the surface of Icarus has RMS slopes of $\sim$16°. For comparison, Evans & Hagfors (1968) found S_0 for the lunar maria of 10.2° and 14.8° at wavelengths of 68 cm and 3.6 cm, respectively.

Figure 3.4 shows a series of delay-Doppler images obtained on the first day of Arecibo observations, the corresponding model images, and the residuals, while Figure 3.2 shows the observed Doppler spectra compared to those predicted by our adopted model. The simulated observations for this set of figures were generated from the average shape, spin pole, and scattering parameters of our adopted solution (Table 3.5, blue cluster).

As we will discuss in Section 3.5, this cluster's spin pole is our preferred solution because it is consistent with historical radar measurements and because of the sign of Icarus' semi-major axis drift.

3.4.4 Astrometry and orbit refinement

Our shape modeling allowed us to estimate the round-trip light times between Arecibo's reference position and the center of mass of Icarus with a fractional precision of $\sim 10^{-8}$. We used the blue cluster shape parameters for the purpose of computing radar astrometry (Table 3.6).

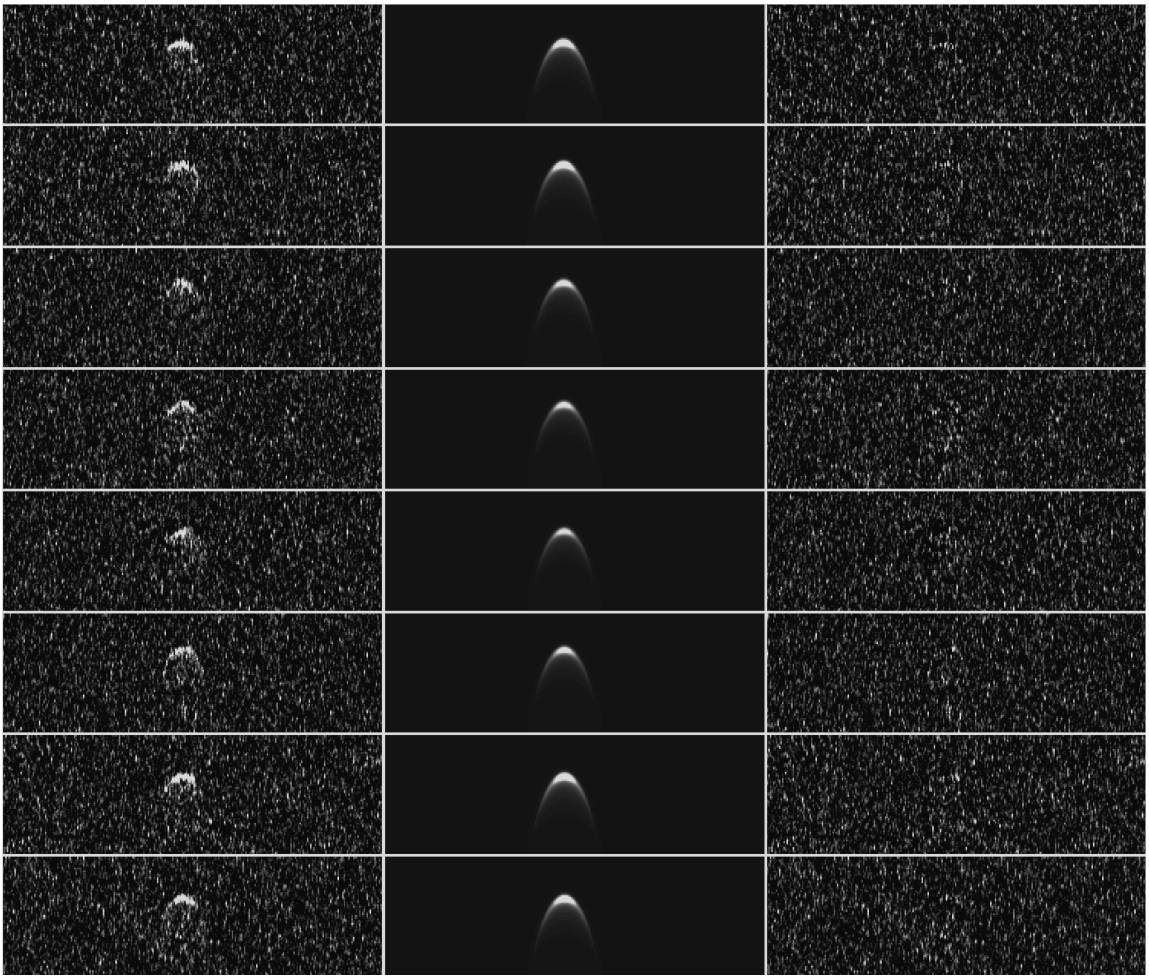

Figure 3.4: Delay-Doppler images of 1566 Icarus, showing (a) the observed data, (b) simulated images from the best-fit ellipsoid model, and (c) the residual images. The delay-Doppler observations of 1566 Icarus were taken from Arecibo Observatory on June 17. These data have a range resolution of 0.2 μs, corresponding to 30 m, with four samples per baud (i.e., each pixel represents 7.5 m), and reduced with a frequency resolution of 0.30 Hz. Each image includes 15 looks, or independent realizations. Images are separated by $\sim$2 minutes. Within each image, range increases from top to bottom and frequency increases from left to right.

Table 3.6: Arecibo radar astrometry. Round-trip light time measurements between Arecibo's reference position and the center of mass of 1566 Icarus at the receive times listed. Estimates of the COM positions are based on fits of our best-fit shape model to the radar images.

Time (UTC)	RTT (μs)	1-σ uncertainty (μs)
2015 Jun 18 00:02:00	58591220.06	0.4
2015 Jun 18 00:58:00	58866141.40	0.4
2015 Jun 18 23:41:00	67308377.46	1.0
2015 Jun 19 01:37:00	68163275.58	1.0
2015 Jun 20 00:58:00	79708409.31	2.0
2015 Jun 20 01:33:00	80022300.66	2.0

Despite a 60+ year arc of optical observations, the inclusion of the 2015 radar astrometry reduced uncertainties on orbital parameters by a factor of $\sim$3 (Table 3.7).

Table 3.7: Orbital elements and improvements in their formal uncertainties after inclusion of the 2015 radar astrometry. The elements are semi-major axis a, eccentricity e, inclination i, longitude of the ascending node Ω, argument of pericenter ω, and mean anomaly M. These orbital elements are valid at the epoch 2015 June 12 00:00:00 UT with our nominal Yarkovsky drift solution (Section 3.4.5).

Parameter	**Value**	**Uncertainty**		**Improvement factor**
		Without 2015 radar data	With 2015 radar data	
a (au)	1.077926624685	6.5e-11	2.6e-11	2.5
e	0.826967321289	3.0e-08	6.9e-09	4.3
i (deg)	22.828097364019	6.9e-06	2.5e-06	2.8
Ω (deg)	88.020929001348	1.6e-06	6.5e-07	2.5
ω (deg)	31.363864782557	3.4e-06	1.2e-06	2.8
M (deg)	34.015936514108	1.7e-06	4.3e-07	4.0

3.4.5 Yarkovsky drift

We calculated the $\hat{\alpha}$ value for Icarus' orbit ($e = 0.83$) of $\hat{\alpha} = 3.16$ (Equation 3.8). We then identified the best-fit efficiency factor ξ (Section 3.3.4.1). Assuming a density of $\rho = 2.7$ g cm^{-3} appropriate for Q-type asteroids (DeMeo et al., 2014) and our adopted effective diameter of $D = 1.44$ km, the best-fit efficiency factor is $\xi = (4.1 \pm 0.4)\%$.

The best-fit ξ value corresponds to a semi-major axis drift rate of $\langle da/dt \rangle = (-4.62 \pm 0.48) \times 10^{-4}$ au/My. This lies within one standard deviation of the value found by Nugent et al. (2012) of $\langle da/dt \rangle = (-3.2 \pm 2.0) \times 10^{-4}$ au/My. Farnocchia et al. (2013b) found a drift rate of $\langle da/dt \rangle = (-0.86 \pm 1.8) \times 10^{-4}$ au/My. Neither of these previous results incorporated the 2015 radar astrometry, nor the more than 300 optical observations taken of 1566 Icarus since 2012.

The p-value (Section 3.3.4.3) for a Yarkovsky drift model with $\langle da/dt \rangle = (-4.62 \pm 0.48) \times 10^{-4}$ au/My and 2312 degrees of freedom is less than 10^{-10}, leading to a confident rejection of the null hypothesis (Section 3.3.4.3), which we interpret as a Yarkovsky detection.

In addition to conducting an analysis of variance (Table 3.8), we performed a variety of analyses to test the rigor of our Yarkovsky result. A description of these tests can be found in Appendix E.

We note that while our analysis of the thermal acceleration acting on Icarus assumed a spin pole aligned with the orbital pole (Section 3.3.4.1), our final $\langle da/dt \rangle$ value is insensitive to this assumption. We performed numerical estimates (Figure 3.5) of the magnitude of the Yarkovsky effect for the four possible spin pole orientations (Section 3.4.3). The drift was calculated as the change in position between the best-fit Yarkovksy model and the best-fit model with no Yarkovksy effect. The $\langle da/dt \rangle$ value shown was calculated as the slope of a linear fit through these differences. All spin pole orientations gave consistent semi-major axis drifts.

Table 3.8: Yarkovsky measurement results for 1566 Icarus. The observational arc for these measurements was 1949–2015. The radar astrometry includes both Arecibo and Goldstone measurements from 2015. N_{opt} and N_{rad} indicate the number of optical (after outlier rejection) and radar measurements, respectively. F indicates the F-score, which serves as a measure of significance for the necessity of a non-gravitational force component in the dynamical model (Section 3.3.4.3). An F-score of 70 or above corresponds to a p-value of less than 10^{-15}, or a detection at the $\geq 8\sigma$ level. The rows labeled MPC indicate analysis done with the full MPC data, with basic outlier rejection (which discarded 80 optical observations), and observational weighting calculated using the methods described in Farnocchia et al. (2015). The rows labeled "Screened" indicate analysis done with a smaller data set from which astrometry deemed suspect on the basis of a gravity-only model was eliminated (Jon Giorgini, pers. comm.). A full description of the data and methods used can be found in Appendix E.

Data set used	N_{opt}	N_{rad}	$\langle da/dt \rangle$	F
MPC	1148	23	-4.6 ± 0.5	250
	1148	-	-4.9 ± 0.5	264
Screened	931	23	-4.0 ± 0.9	139
	931	-	-3.8 ± 1.1	107
Screened (JLM)	931	-	-3.6 ± 1.0	98

These drift rates are also consistent with the rate of $(-4.62 \pm 0.48) \times 10^{-4}$ au/My, determined semi-analytically using equation (3.8).

We plan on using our MONTE-based orbit determination software to measure the orbital perturbations affecting other NEOs in Icarus-like orbits (Margot & Giorgini, 2010). These measurements can in turn be used to put constraints on the β parameter in the post-Newtonian parametrization of general relativity (GR) and possibly the oblateness of the Sun. The GR and Yarkovsky perturbations are essentially orthogonal because Yarkovsky drift primarily affects the semi-major axis, whereas GR does not affect the semi-major axis but instead causes a precession of the perihelion. The cleanest separation between these perturbations will be obtained by solving for the orbits of multiple asteroids simultaneously (Margot & Giorgini, 2010).

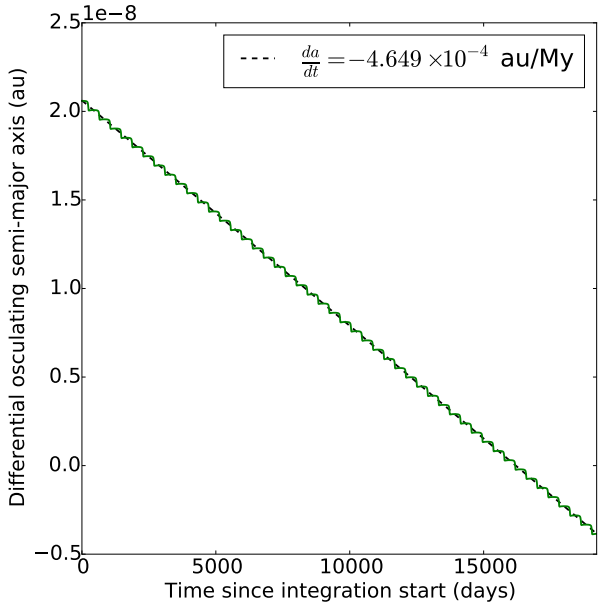

Figure 3.5: The difference in semi-major axis between a $\xi = 0$ Yarkovsky model and the best-fit ξ value for a Yarkovsky model with spin pole located at ecliptic coordinate $\lambda = 270°$, $\beta = -81°$, (the blue cluster). The differential semi-major axis is plotted over the time interval 1963–2015. The $\langle da/dt \rangle$ has been numerically estimated with a linear fit through these data. The estimated drift in semi-major axis is consistent with the result obtained when assuming a spin pole that is parallel to the orbital pole, albeit with a different value of the adjustable parameter ξ (Section 3.4.5).

3.5 Discussion

3.5.1 Spin pole

Table 3.9: A comparison of measured bandwidths from previous radar observations of 1566 Icarus and bandwidths predicted for a variety of spin pole estimates. Antipodal pairs of spin poles yield bandwidths that are identical within the margin of observing error, and thus only one of each pair is shown. Table elements with an asterisk indicate a direct match between that spin pole's bandwidth prediction and the corresponding bandwidth as reported by the authors. Bold-faced table elements indicate a match between that spin pole's bandwidth prediction and the estimated limb-to-limb bandwidth B_{LL}. The B_{LL} was estimated by adjusting for the decrease in apparent observed bandwidth caused by Icarus' highly specular surface, which results in an approximate halving of the observed bandwidth as compared to the nominal limb-to-limb bandwidth for very low SNR observations. The estimated B_{LL} also accounts for the fact that some authors reported the half-max bandwidth, rather than zero-crossing bandwidth. All bandwidth measurements and predictions have been converted to the Arecibo S-band frequency of 2380 MHz for ease of comparison. For observational details, see Appendix C.

Observer	**Pettengill et al.**		**Goldstein**	**Mahapatra et al.**	**This work**		
Year	1968			1996	2015		
Date	June 13	June 14–15	June 15–16	June 8–10	June 14	June 18	June 21
Reported by authors	19.0	4.0	7.0	9.8	10.4 ± 1.7	11.8 ± 0.8	14.5 ± 4.5
Estimated B_{LL}	37.6	12.4	17.5	19.6	12.7	16.5	19.4
This work, green (predicted)	*17.4	18.5	19.4	*12.1	**14.2**	**16.6**	**19.6**
This work, blue (predicted)	6.9	**12.0**	**16.3**	**19.8**	**13.4**	**17.0**	**19.9**
Gehrels et al. 1970 (predicted)	*19.9	20.0	18.9	**20.0**	17.7	16.3	7.8
De Angelis 1995 (predicted)	*20.1	19.3	**17.5**	**19.1**	19.5	12.9	3.4

As noted in Section 3.4, analysis of our radar data yields four possible sets of spin pole orientations for Icarus, and given their low $\Delta\chi$ values, these solutions are statistically indistinguishable from each other. Icarus' spin pole has also been measured in the past from lightcurve data, which gave three possible spin poles. Lightcurve observations of Icarus between 1968 June 14 and June 21 were analyzed by Gehrels et al. (1970) and re-analyzed by De Angelis (1995). Gehrels et al. (1970) reported a spin axis orientation of $\beta = 0^\circ \pm 3^\circ$, $\lambda = 223^\circ \pm 3^\circ$ or $49^\circ \pm 3^\circ$, whereas De Angelis (1995) found $\beta = 5^\circ \pm 5^\circ$, $\lambda = 214^\circ \pm 5^\circ$. These lightcurve-derived spin poles are not consistent with our 2015 radar data, which leaves two possibilities – either the lightcurve-derived spin poles are incorrect, or Icarus' spin pole has changed at some point since the 1968 apparition. We can determine which of these two possibilities is more likely by analyzing historical radar measurements of this object.

Table 3.9 lists Icarus' reported bandwidths from the three radar apparitions that garnered CW measurements – namely 1968 (Pettengill et al., 1969; Goldstein, 1969), 1996 (Mahapatra et al., 1999), and 2015 (this work) – along with the bandwidths that would have been measured at the corresponding dates, if Icarus' spin pole orientation were constant. We generated predictions for four possible spin poles – $\lambda = 313^\circ \pm 10^\circ, \beta = -6^\circ \pm 10^\circ$ (the green cluster), $\lambda = 270^\circ \pm 10^\circ, \beta = -81^\circ \pm 10^\circ$ (the blue cluster), $\beta = 0^\circ \pm 3^\circ, \lambda = 49^\circ \pm 3^\circ$ (Gehrels et al., 1970), and $\beta = 5^\circ \pm 5^\circ, \lambda = 214^\circ \pm 5^\circ$ (De Angelis, 1995) – and compared the predicted measurements for these poles to the reported values. A direct comparison suggests that no spin pole is consistent with measurements from more than one apparition. However, this interpretation is slightly misleading, as there were a variety of *types* of bandwidths reported in these articles. Pettengill et al. (1969) and Goldstein (1969) reported bandwidths at full-width half-max (FWHM), while Mahapatra et al. (1999) reported their best estimate of the limb-to-limb bandwidth (Appendix C). In this work, we reported the measured bandwidth at one standard

deviation above the noise ($B_{>1}$), as well as the limb-to-limb bandwidth calculated from our shape models. Therefore, to facilitate comparisons of these bandwidths, we have attempted to convert the historical measurements to limb-to-limb bandwidths by estimating the signal's zero-crossing point, as well as adjusting for the decrease in apparent bandwidth caused by Icarus' highly specular surface (Section 3.4.2). When comparing the predicted limb-to-limb bandwidths with these measured limb-to-limb bandwidths, we find that our red/blue cluster spin poles is consistent with all previous CW measurements of Icarus, save the first spectrum obtained by Pettengill et al. (1969) on 1968 June 13. However this measurement had a particularly low SNR, and was considered potentially problematic by the observers. Therefore, if we discard the first radar observation and assume that the lightcurve-derived spin poles are incorrect, we can find a principal axis rotation state (aligned with either the red or blue cluster solutions) that is consistent with the historical data. Furthermore, the slowly contracting orbit (Section 3.4.5) is indicative of a spin pole anti-aligned with the orbital pole. This suggests that, if Icarus is a principal axis rotator, it is likely to be a retrograde spinner, and thus aligned with the blue cluster solution at ecliptic coordinates

$$\lambda = 270^\circ \pm 10^\circ,$$

$$\beta = -81^\circ \pm 10^\circ.$$

However, if the lightcurve-derived spin poles are correct, then the spin axis orientation of Icarus would have had to have changed since the 1968 apparition. A difference in spin orientation may be caused by non-principal axis (NPA) rotation or the effect of torques due to anisotropic mass loss. Mass loss may occur due to thermal fracturing. NPA rotation may remain undetected in lightcurve or radar data if one of the fundamental periods is long compared to the span of observations in any given apparition or if the object is approximately spheroidal. NPA rotation requires a mechanism to excite the spin state on a time scale shorter

than the NPA damping time scale. The Burns & Safronov (1973) time scale for damping to principal axis rotation assuming silicate rock ($\mu Q = 5 \times 10^{12}$ Nm^{-2}, $\rho = 2.71$ g cm^{-3}) is ∼25 million years, during which Icarus experiences close planetary encounters that may excite its spin. However, if the material properties are closer to those reported by Scheirich et al. (2015) ($\mu Q = 1.3 \times 10^{7}$ Nm^{-2}), NPA rotation would require an excitation in the past 100 years, which we consider unlikely.

Three arguments favor the principal axis rotation solution: (1) the lightcurve-derived spin poles predict bandwidths that are inconsistent with observations (Table 3.9), (2) the bandwidths predicted by the blue cluster spin pole solutions can match observations over three separate apparitions, (3) damping to principal axis rotation would likely occur on short time scales. This conclusion suggests that interpreting the evolution of lightcurve amplitudes may not be sufficient in determining spin pole orientations accurately. Other considerations, such as knowledge of albedo variations and inhomogeneous scattering behavior, may be necessary to properly interpret lightcurve data.

3.5.2 Cross-section and size

Using the results of our analysis, we have found that 1566 Icarus' radar scattering behavior is consistent with a Hagfors specularity constant of $C = 13$. This level of specularity is unusual for NEOs (Appendix D), and helps to explain the lower-than-expected image quality. Diffusely-scattering surfaces can reflect power from high incidence angles – therefore, surface elements with normal vectors not aligned with the observer's line of sight can still contribute to the return signal. The surface elements of specular objects, on the other hand, reflect most of their incident power away from the observer unless they lie close to the sub-radar point (for ellipsoidal objects). The result is a very sharp drop-off in SNR for incidence angles greater than ∼20°. This effect can be seen in Figure 3.4.

Furthermore, the small amount of echo power returning from regions with high incidence angles ($\theta_{inc} \gtrsim 45°$) helps to resolve the difference between Icarus' observed bandwidth and the limb-to-limb bandwidth calculated from the object's shape and spin pole orientation (Table 3.4). The most highly red- and blue- shifted signals are reflected from these high-incidence regions, and the large attenuation of these signals reduces the span of the measured bandwidth. This effect may also explain a discrepancy noticed by Mahapatra et al. (1999), who measured Icarus' bandwidth during its previous radar apparition nearly two decades ago, and pointed out that the measured bandwidth corresponds to a diameter around half of the value found radiometrically by Harris (1998).

The results presented within this work suggest Icarus' surface and sub-surface properties are unusual amongst the known population of NEOs. The radar albedo $\hat{\sigma}_T$ (defined as the radar cross-section divided by the object's geometric cross-section) for an object with a diameter of ∼1.44 km and a measured radar cross-section of 0.03 km^2 is less than 2% (see Table 3.3), which we believe to be the lowest radar albedo ever measured (e.g., Magri et al., 1999; Magri et al., 2001, 2007a).

The radar albedo for a specular reflector provides an approximation to the Fresnel reflectivity, which is related to the dielectric constant (Evans & Hagfors, 1968). Our radar albedo measurement yields the surprising low dielectric constant of 1.8. Most non-volcanic rocks have dielectric constants above 5, unless they are in a powdered form with high porosity (Campbell & Ulrichs, 1969), in which case their dielectric constants are about 2. Our measurements suggest that Icarus may have a low surface density or, equivalently, a high surface porosity.

Furthermore, a radar specularity of $C = 13$ is unusually high compared to most radar-imaged NEOs. This high specularity and low radar albedo suggest an unusual surface structure. Due to its highly eccentric orbit ($e = 0.82$) and low semi-major axis ($a = 1.08$ au), Icarus approaches within 0.19 au of the Sun. At

that distance, the equilibrium sub-solar point temperature is expected to lie between 600 K and 900 K. Jewitt & Li (2010) found that at temperatures within this range, certain mineral compounds undergo extensive structural changes, possibly through the mechanism of thermal fatigue (Delbo et al., 2014). It is possible that a combination of cratering history, spin evolution, and repeated close approaches to the sun have modified the surface of Icarus in such a way as to substantially lower its radar albedo.

Finally, we point out that the equivalent diameter determined herein adds to the list of conflicting sizes estimates for Icarus in the literature. Using various thermal models, Harris (1998) found a diameter of anywhere between 0.88 km and 1.27 km. Mainzer et al. (2012) determined a diameter of 1.36 ± 0.43 km using NEOWISE data at 3.4μm, 4.6μm, and 12μm, and the Near-Earth Asteroid Model (NEATM) (Harris, 1998). Following their 1999 CW measurements of Icarus, Mahapatra et al. (1999) calculated a diameter between $0.6 - 0.8$ km, assuming the spin pole reported by De Angelis (1995). Finally, a diameter can be calculated from the expression (Fowler & Chillemi, 1992)

$$D = \frac{10^{-0.2H} 1329}{\sqrt{p_V}}, \tag{3.17}$$

which, coupled with the measured H-magnitude of 16.3 (Harris, 1998) and geometric albedo p_V of 0.14 (Thomas et al., 2011), yields a diameter of 1.95 km. More recent lightcurve measurements obtained at large phase angles yield $H = 15.5$ (Warner, 2015), which corresponds to a diameter of 2.80 km. We found an equivalent diameter of 1.44 km with 18% uncertainties.

3.6 Conclusions

In this work, we analyzed Arecibo and Goldstone radar observations of 1566 Icarus to estimate its size, shape, scattering properties, orbital parameters, and Yarkovsky drift. These results suggest that this object has unusual surface prop-

erties, and resolves long-standing questions about the object's size.

We presented the first use of our orbit-determination software and demonstrated its ability to generate accurate radar ephemerides and to determine the magnitude of subtle accelerations such as the Yarkovsky effect.

Acknowledgements

AHG and JLM were funded in part by NASA grant NNX14AM95G and NSF grant AST-1109772. Part of the work done here was conducted at Arecibo Observatory, which is operated by SRI International under a cooperative agreement with the National Science Foundation (AST-1100968) and in alliance with Ana G. Méndez-Universidad Metropolitana (UMET), and the Universities Space Research Association (USRA). The Arecibo Planetary Radar Program is supported by the National Aeronautics and Space Administration under Grant Nos. NNX12AF24G and NNX13AQ46G issued through the Near-Earth Object Observations program. Some of this work was performed at the Jet Propulsion Laboratory, which is operated by Caltech under contract with NASA. This work was enabled in part by the Mission Operations and Navigation Toolkit Environment (MONTE). MONTE is developed at the Jet Propulsion Laboratory. The material presented in this article represents work supported in part by NASA under the Science Mission Directorate Research and Analysis Programs.

APPENDIX A

Numerical Stability

Issues with numerical stability can arise when multiplying matrices with elements at or near the square root of the machine precision. This can lead to erroneous results, or singular matrices for which further calculations (such as the matrix inverse) are impossible.

For example (Bierman, 1977), consider the case when

$$A = \begin{pmatrix} 1 & 1-\epsilon \\ 1-\epsilon & 1 \\ 1 & 1 \end{pmatrix}$$

and

$$W = I.$$

Then

$$(A^{\intercal}WA) = \begin{pmatrix} 3-2\epsilon+\epsilon^2 & 3-2\epsilon \\ 3-2\epsilon & 3-2\epsilon+\epsilon^2 \end{pmatrix}$$

Thus, in the case that ϵ is equal to or less than the square root of the machine precision,

$$(A^{\intercal}WA) = \begin{pmatrix} 3-2\epsilon & 3-2\epsilon \\ 3-2\epsilon & 3-2\epsilon \end{pmatrix}.$$

This matrix is singular, and thus $(A^{\intercal}WA)^{-1}$ cannot be computed. This problem is particularly insidious because matrix singularity in higher dimensions can be difficult to detect.

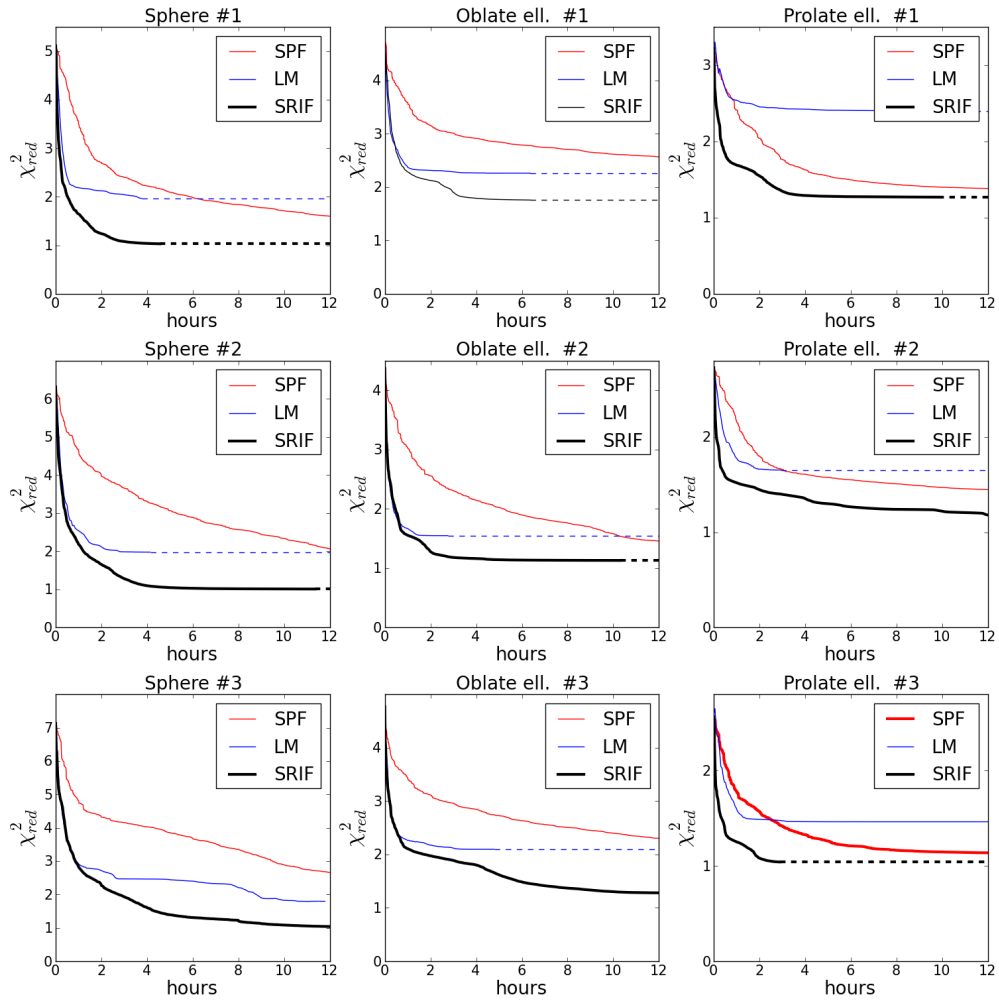

Figure A.1: Results of three fitting algorithms (Sequential Parameter Fit, Levenberg-Marquardt, and Square-Root Information Filter) with three artificial shapes (perturbed versions of a sphere, oblate ellipsoid, and prolate ellipsoid). Bold lines indicate fits which converged to a $\chi^2_{red} < 1.3$. Dashed lines indicate the assumed future state for fits that had converged on a solution before the 12-hour time frame.

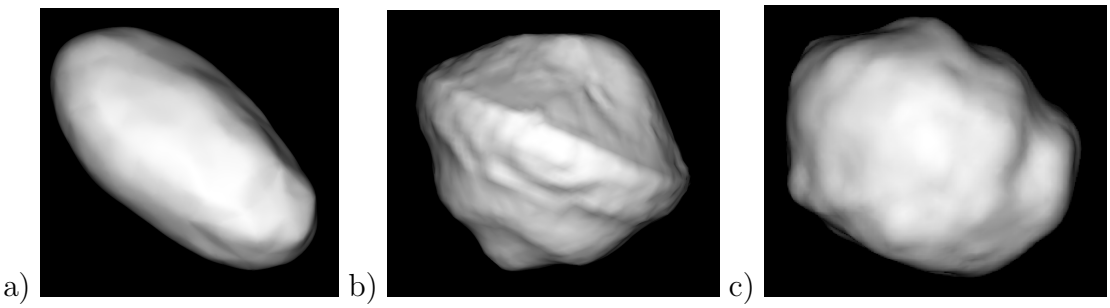

Figure A.2: Plane of sky representations of the radar-derived shape models of (a) Itokawa, (b) 1999 KW4, and (c) 2000 ET70 .

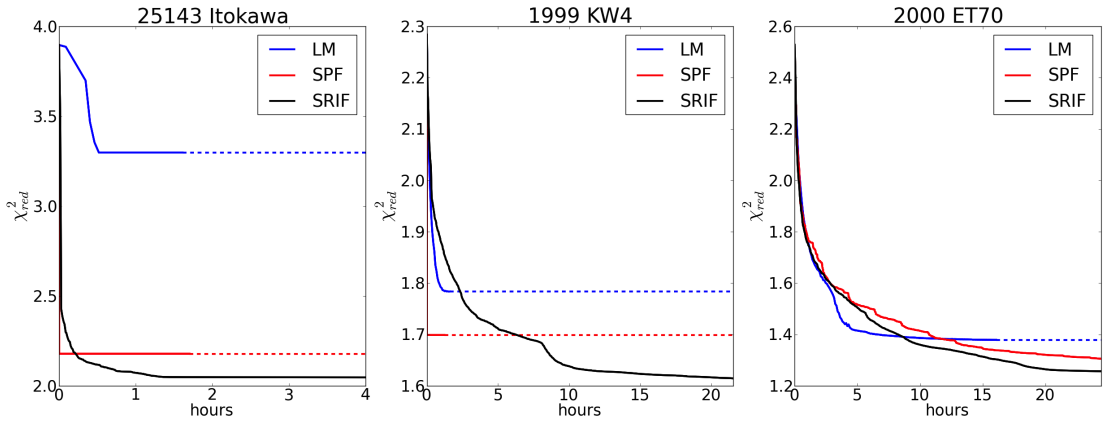

Figure A.3: Results comparing SRIF, LM, and SPF operating on real asteroid shapes with simulated χ^2-distributed errors. Dashed lines indicate the assumed future state for fits that had converged on a solution. These fits were run without penalty functions. Note that the solution arrived at by SPF for 1999 KW4 was a non-physical, pebble-sized asteroid. Avoiding non-physical minima in the χ^2 space would require human intervention to manually tweak the starting conditions. We did not perform such tweaks in order to maintain consistency in our tests.

a) 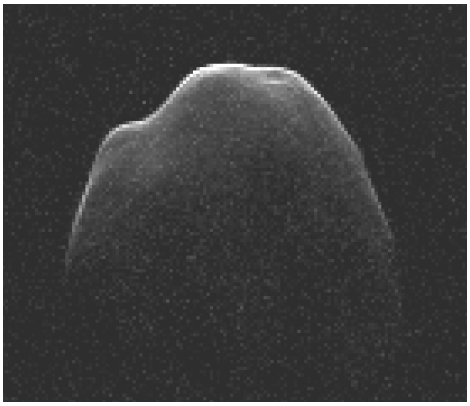 b) 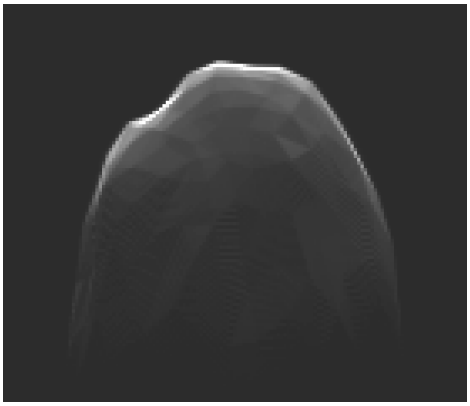

Figure A.4: (a) Example of a simulated input to the shape modeling algorithm. The input is generated by projecting the shape model into range-Doppler space at a specific observation epoch and adding random noise. (b) The corresponding synthetic image produced by the shape modeling algorithm after fitting for the shape.

a)

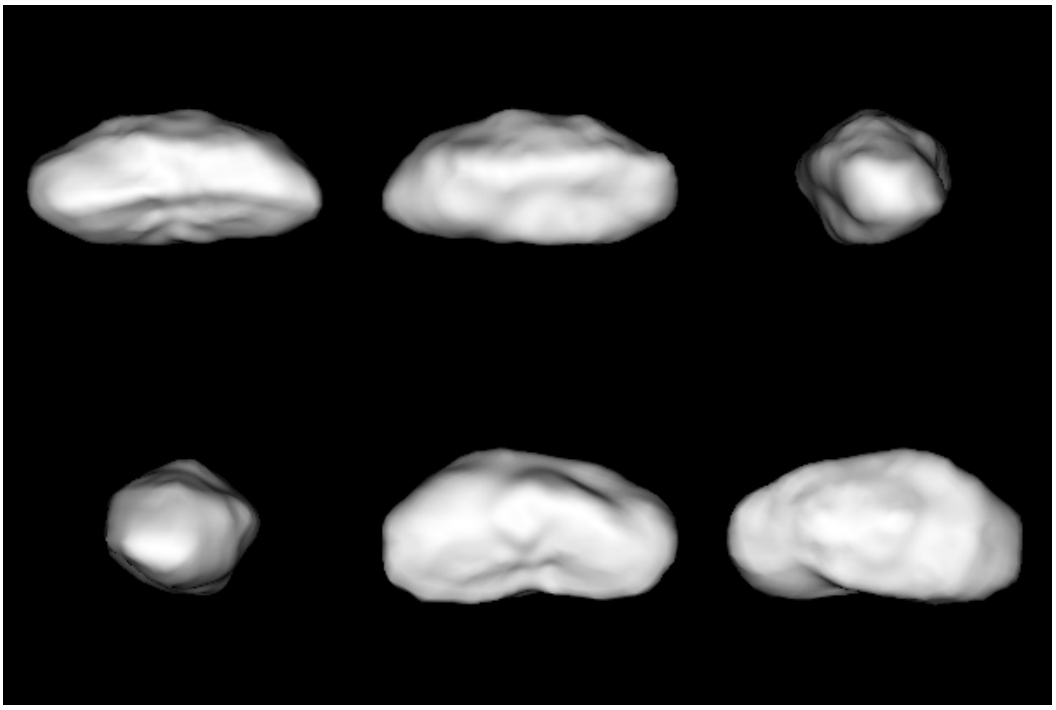

b)

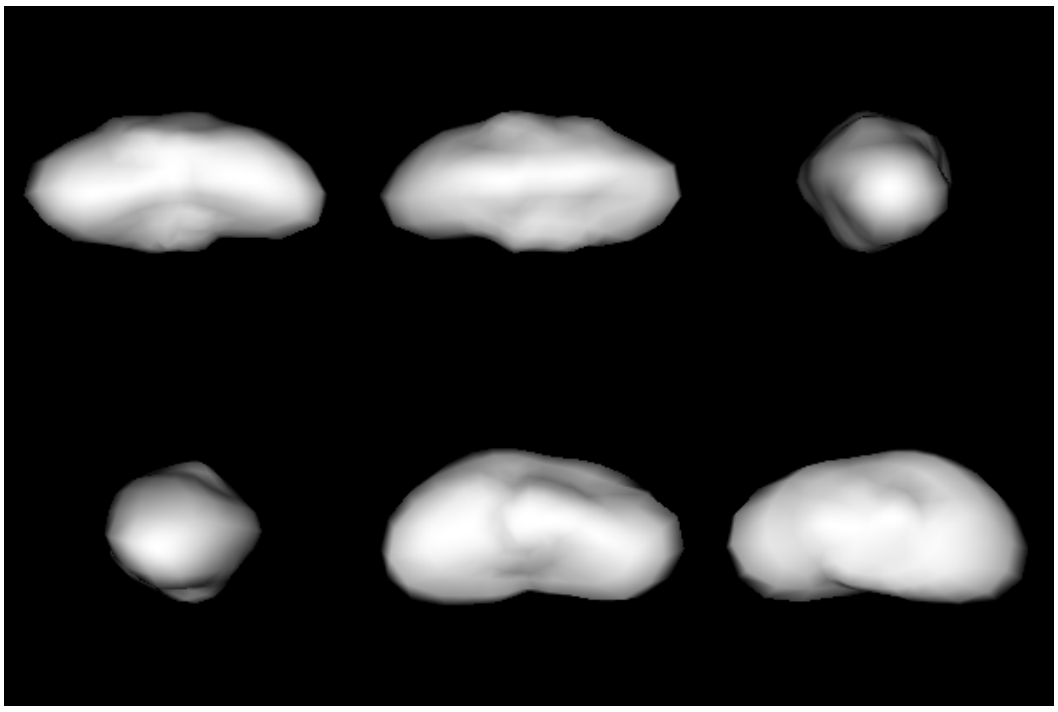

Figure A.5: a) The Itokawa shape model that was used to generate simulated radar images (Ostro et al., 2005). b) The best-fit SRIF tenth degree spherical-harmonics model for those simulated data, using penalty functions. The initial conditions for the shape parameters were a sphere with an offset spin axis latitude and longitude.

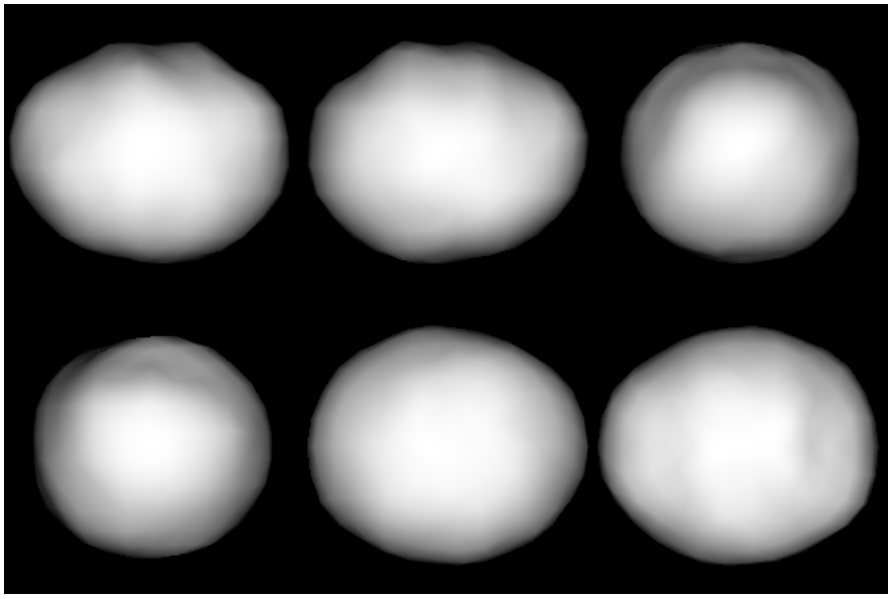

Figure A.6: The best SRIF fit spherical harmonic model for 2000 ET70, which is in good agreement with the model of Naidu et al. (2013).

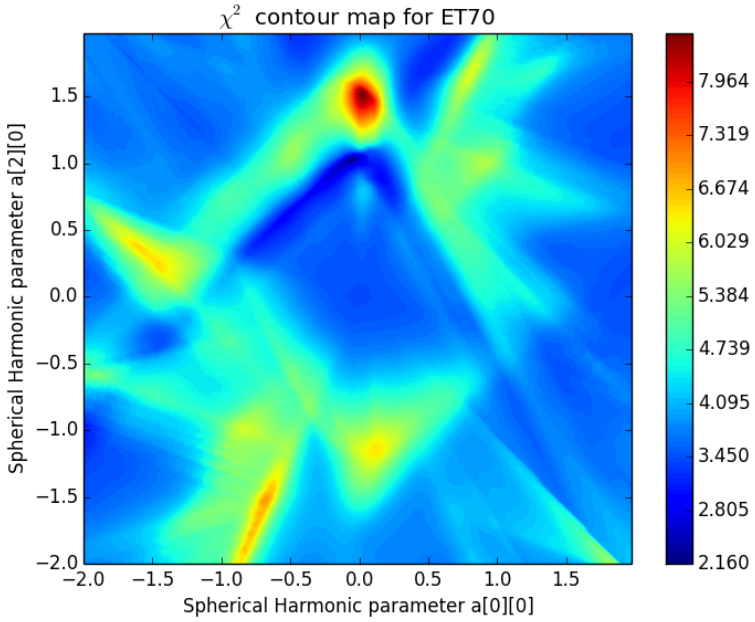

Figure A.7: A two-dimensional slice of the χ^2 space for fitting shape models to radar data. This contour map represents χ^2 for a spherical harmonic model with all parameters fixed except two of the elements of the primary coefficient matrix. Note that the blue regions indicate low χ^2, and that there are several of these regions for a derivative-based optimizer to fall towards, depending on the initial set of starting conditions.

APPENDIX B

Yarkovsky acceleration

For an object with diameter D, at distance from the Sun at time t of r_t, the energy absorbed per second is

$$\dot{E} = \frac{L_\odot}{4\pi r_t^2}\,\pi\left(\frac{D}{2}\right)^2,$$

assuming perfect absorption.

The acceleration $\ddot{r}$ is equal to the photon momentum absorbed, $\dot{p_\gamma}$, over the mass of the object, m.

$$\begin{aligned}\ddot{r} &= \frac{\dot{p_\gamma}}{m}\\ &= \frac{\dot{E}/c}{m}\\ &= \frac{L_\odot}{4\pi r_t^2}\,\pi\left(\frac{D}{2}\right)^2\,\frac{1}{c}\,\frac{1}{m}.\end{aligned}$$

Expressing the object mass in terms of density, ρ, and D, yields

$$\begin{aligned}\ddot{r} &= \frac{L_\odot}{4\pi r_t^2}\,\pi\left(\frac{D}{2}\right)^2\,\frac{1}{c}\,\frac{1}{\frac{4}{3}\pi\left(\frac{D}{2}\right)^3\rho}\\ &= \frac{3}{8\pi}\,\frac{L_\odot}{c}\,\frac{1}{r_t^2}\,\frac{1}{D\rho}.\end{aligned}$$

This acceleration is applied in the positive radial direction (in heliocentric coordinates).

$$\ddot{\vec{r}} = \frac{3}{8\pi}\,\frac{1}{D\rho}\,\frac{L_\odot}{c}\,\frac{1}{r_t^2}\,\hat{r}$$

Because it is purely radial, this acceleration will not cause a measurable change in the orbit.

However, the absorbed photons will eventually be re-radiated, and induce an acceleration upon emission as well. Since the object is rotating about some spin axis $\hat{p}$, this secondary acceleration will not (necessarily) occur along a radial direction. Furthermore, given that *all* the absorbed photons must eventually be re-radiated, we can express the magnitude of this secondary acceleration in the same manner as its radial counterpart. Here we define a phase lag, ϕ, to describe at what rotational phase (relative to the sub-solar longitude) the majority of the photons are re-emitted, and an efficiency factor, ξ, which is tied to the effective acceleration if one assumes that all photons are re-emitted with phase lag ϕ. $X_{\hat{p}}(\phi)$ is the rotation matrix of angle ϕ about $\hat{p}$.

$$\ddot{\vec{r}} = \xi \, \frac{3}{8\pi} \, \frac{1}{D\rho} \, \frac{L_\odot}{c} \, \frac{X_{\hat{p}}(\phi)\vec{r_t}}{||\vec{r_t}||^3}.$$

The Yarkovsky effect is caused by this *non-radial* secondary acceleration.

APPENDIX C

Historical data concerning 1566 Icarus' spin pole orientation

For the purpose of facilitating bandwidth comparisons, we normalize all bandwidths to the Arecibo S-band frequency of 2380 MHz and label the corresponding unit S-Hz. Except where otherwise noted, the bandwidths discussed here are relayed as they were reported in the corresponding articles – i.e., without any corrections applied for specularity. We also note the distinction between reported half-power bandwidths and zero-crossing bandwidths.

C.1 Pettengill et al. 1968 radar observations

The radar detection of Icarus by Pettengill et al. (1969) on 1968 June 13 marked the first detection of an asteroid with radar. These observations were conducted at the Haystack Observatory at a frequency of 7840 MHz. A second set of observations took place on 1968 June 15. Pettengill et al. (1969) observed half-power Doppler extents of 70 Hz on June 13 and 13 Hz on June 15. Because both sets of observations spanned multiple rotations of Icarus, the change in bandwidth cannot be attributed to the shape of the object.

The bandwidth reported on June 13 is over-estimated, for two reasons. First, the authors reported a drift of their data-taking ephemeris by 8 Hz over the data-taking period, indicating that the echo was at most 62 Hz. Second, the authors applied a variety of smoothing windows (8, 16, 32, and 64 Hz) and reported only

the spectrum with the maximum signal-to-noise ratio, which they obtained with the 64 Hz smoothing window. Because the convolution operation broadened the echo, we estimate that the original, intrinsic echo was between 32 and 62 Hz.

Thus, the June 13 Pettengill et al. (1969) half-power bandwidth correspond to a value between 9.7 S-Hz and 19 S-Hz, and the June 15 bandwidth corresponds to 4.0 S-Hz.

C.2 Goldstein 1968 radar observations

Goldstein (1969) detected Icarus between 1968 June 14 and 16 with a bistatic configuration at Goldstone. The frequency was 2388 MHz and the reported half-power bandwidth for observations between June 15 04:30 UT and June 16 10:00 UT is about 7 Hz (or 7 S-Hz).

C.3 Gehrels et al. 1968 lightcurve observations

Lightcurve observations of Icarus between 1968 June 14 and June 21 were analyzed by Gehrels et al. (1970) and re-analyzed by De Angelis (1995). Gehrels et al. (1970) reported a spin axis orientation of $\beta = 0° \pm 3°$, $\lambda = 223° \pm 3°$ or $49° \pm 3°$, whereas De Angelis (1995) found $\beta = 5° \pm 5°$, $\lambda = 214° \pm 5°$. These spin poles do not appear to be consistent with most of the radar CW bandwidths observed during the 1968, 1996, or 2015 apparitions (Table 3.9).

C.4 Mahapatra et al. 1996 radar observations

Mahapatra et al. (1999) used Goldstone and observed a zero-crossing Doppler bandwidth of 35 Hz at 8510 MHz. Because they used a 10 Hz smoothing window, the intrinsic bandwidth could be 35–45 Hz, or a value between 9.8 and 12.6 S-Hz.

APPENDIX D

Attempts to fit a lower specularity

The specularity reported in this work for 1566 Icarus is unusually high. When originally fitting the shape and scattering properties for this object, we initially forced a lower specularity on our models. After many such attempts, we came to the conclusion that a diffusely-scattering surface did not match the data we observed.

Figure D.1 demonstrates what an attempted fit to Icarus' CW spectra and delay-Doppler images looks like, when the specularity is fixed to a lower value of $C = 2$, and a 'cos' scattering law is utilized. This scattering behavior can be defined with respect to the differential radar cross section per surface element area (Section 3.3.1.1), via

$$\frac{d\sigma}{dA} = R(C+1)\cos^{2C}\theta. \tag{D.1}$$

These fits are the result of allowing all other model parameters (ellipsoid axis ratios, signal scaling parameters, etc.) to float, and performing a full fit on the same dataset used for the results reported in this article. The best-fit model has an equivalent diameter of 1.05 km and, as the figure demonstrates, results in a poor fit to the data. Note in particular that while the bounds of the model spectrum is approximately equal to the bounds of the data spectrum, the shape of the spectra do not match. In addition, the signal in the delay-Doppler image does not drop off fast enough as range from the observer increases. The fast drop-off noted in the data necessitates a specular model. Such a model can be realized with either a two-component 'cos' scattering law or a 'hagfors' scattering law.

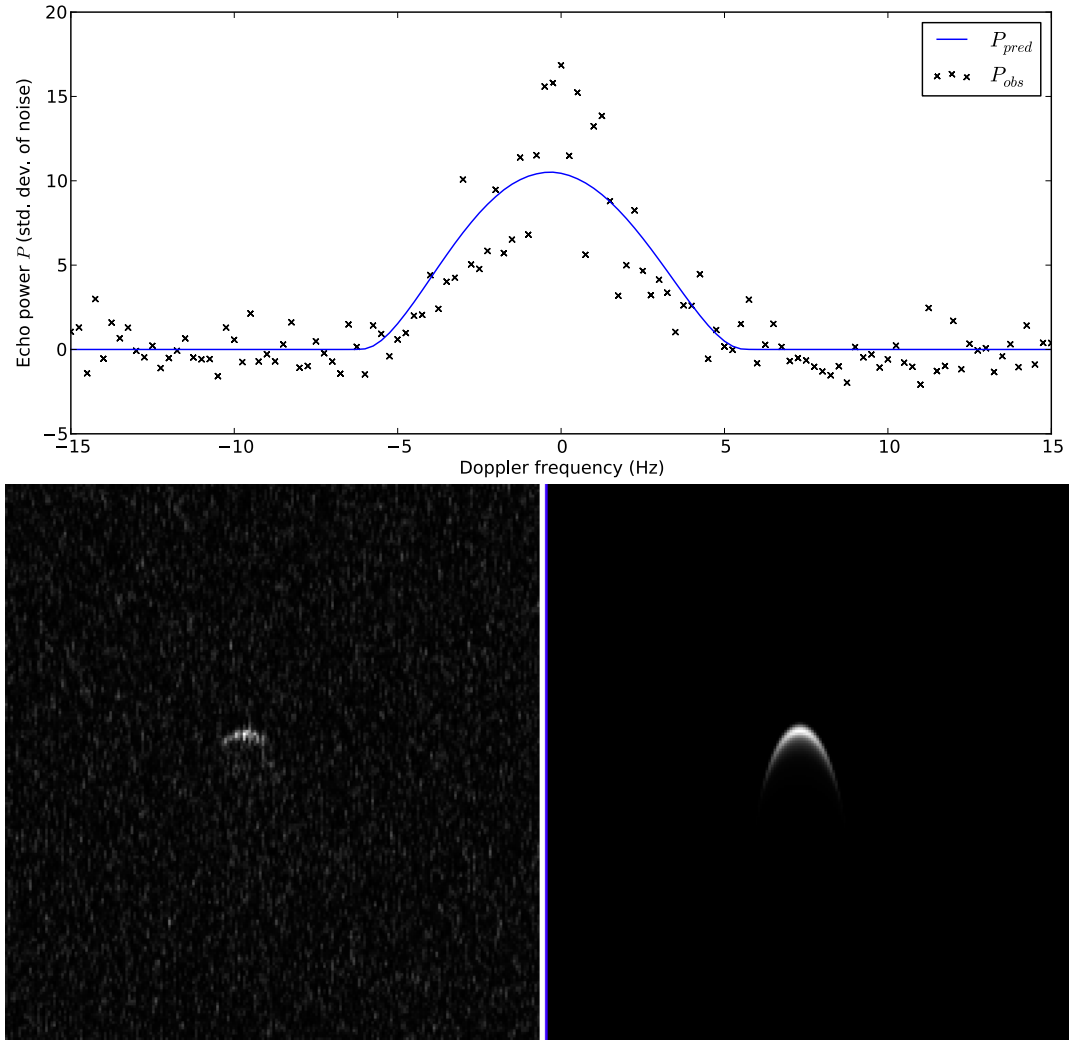

Figure D.1: A result of a global fit to CW spectra and delay-Doppler images of 1566 Icarus, with the specularity constant C fixed to 2.0. Shown is an example comparison between the observed data and best-fit model spectrum for data taken on June 17, (top), as well as a comparison between a best-fit model delay-Doppler image (bottom right) and the corresponding observed image (bottom left), also taken on June 17. The fit shown does not match the data, and suggests that a higher specularity model is needed.

APPENDIX E

Additional evidence of Yarkovsky detection

We performed a variety of analyses to test the rigor of our Yarkovsky result (Section 3.4.5).

E.1 Screening test

We re-ran our Yarkovsky analysis with an independently curated set of optical and radar astrometry (Jon Giorgini, pers. comm.). This data set has been screened for potential outliers and faulty measurements using a gravity-only model, with around 20% of the original astrometric data being discarded. Our analysis of these data (931 optical astrometric points and 23 radar astrometric points from 1949 to 2015) yielded a drift in semi-major axis of $\langle da/dt \rangle = -4.0 \pm 0.9 \times 10^{-4}$ au/My when including both radar and optical astrometry and $\langle da/dt \rangle = -3.8 \pm 1.1 \times 10^{-4}$ au/My when including optical astrometry only (Table 3.8).

As a further verification, one of us (JLM) used the software he developed in previous work (Nugent et al., 2012) with this independently screened data set and found $\langle da/dt \rangle = (-3.6 \pm 1.0) \times 10^{-4}$ au/My (Table 3.8).

E.2 Prediction test

One way to analyze the accuracy of a Yarkovsky result is to check its predictive power when compared to a gravity-only dynamical model. Instead of collecting

additional astrometry, which is not straightforward, we can simulate a prediction by re-analyzing a subset of the data before some fiducial point in time, t_f, and then checking how the resulting trajectory fares at predicting observations that were taken after t_f.

The first range measurement of Icarus was obtained from Goldstone on June 14, 2015 (Table 3.2). We therefore chose 2015-June-13 23:50 UT as t_f. We fit a Yarkovsky model to the data taken before t_f (936 optical observations and 11 radar observations, from which 55 optical observations were discarded as outliers), and found a semi-major axis drift rate of $\langle da/dt \rangle = (-3.7 \pm 0.7) \times 10^{-4}$ au/My. This fit yielded a goodness-of-fit of $\chi^2 = 634$. We also fit a gravity-only model to the same set of data, which resulted in a goodness-of-fit of $\chi^2 = 662$. We then compared how well these best-fit trajectories could predict the first Icarus range measurement on June 14, 2015. The best-fit Yarkovsky model residual for this prediction was 97 km, while the best-fit gravity-only model residual was 267 km. This demonstrates that the Yarkovsky model more accurately predicted a future measurement than the gravity-only model.

E.3 Incorporation test

Another test of rigor is an incorporation test. After performing the prediction test described above, we then added the first Doppler and range measurements of 2015 and fit both a gravity-only model and a Yarkovsky model once again. No additional outlier rejection was allowed. With these new Doppler and range measurements, the best-fit semi-major axis drift rate for the Yarkovsky model is $\langle da/dt \rangle = (-4.7 \pm 0.5) \times 10^{-4}$ au/My. The goodness-of-fit for the Yarkovsky model is $\chi^2 = 638$, or a $< 1\%$ increase as compared to the Yarkovsky fit prior to including the new radar measurements. The best-fit gravity-only model yielded a goodness-of-fit of $\chi^2 = 719$, or a 9% increase as compared to the gravity-only fit prior to

including the new radar measurements. These results suggest that incorporating the first Icarus radar measurements into a gravity-only model results in a general degradation in the quality of the fit to optical observations. However, these same radar measurements can be included in a Yarkovsky model with no appreciable effect on the goodness-of-fit.

E.4 Combined test

Finally, we re-ran both the prediction test and the incorporation test described above on the curated data set. The best-fit Yarkovsky model fit to data taken before t_f yielded a drift in semi-major axis of $\langle da/dt \rangle = (-3.53 \pm 1.11) \times 10^{-4}$ au/My, and a goodness-of-fit of $\chi^2 = 172$, while the gravity-only model had a goodness-of-fit of $\chi^2 = 182$. The Yarkovsky model predicted the first Goldstone range measurement with a residual of 43 km, while the gravity-only model predicted residual for that data point was 128 km. For the incorporation test, we again added the first Goldstone Doppler and range measurements to the data set. For the Yarkovsky model, the best-fit drift in semi-major axis was $\langle da/dt \rangle = (-3.95 \pm 0.97) \times 10^{-4}$ au/My, with a goodness-of-fit of $\chi^2 = 173$, or an increase of $< 1\%$ as compared to the Yarkovsky fit prior to adding the new radar measurements. The best-fit gravity-only model had a goodness-of-fit of $\chi^2 = 189$, or a 4% increase as compared to the gravity-only model fit prior to adding the new radar measurements. Note that these fits were performed on a data set for which outlier rejection had been performed assuming a gravity-only model — even so, a gravity-only model still required a marked decrease in fit quality in order to incorporate the first radar measurements, while the Yarkovsky model saw no appreciable change in goodness-of-fit.

Table E.1: The residuals of the first range measurement obtained of 1566 Icarus when using a Yarkovsky model and a gravity-only model, and when fitting these models only to data taken before the first radar measurements of 2015 (i.e., the prediction test).

	Residual (km)	
Data set	Yarkovsky model	Gravity-only model
MPC	97	267
Screened	43	128

E.5 Summary

The tests that we performed are summarized in Table E.1 and Table E.2, and confirm the robustness of the Yarkovsky detection.

Table E.2: The goodness-of-fit (χ^2) for a Yarkovsky model and a gravity-only model when fit to only data taken before the first radar measurements of 2015 (i.e., before t_f = 2015-June-13 23:50:00 UT), and how χ^2 changes when the first Doppler and range measurements are incorporated into the fit (i.e., the incorporation test).

MPC data set		
	Yarkovsky model	Gravity-only model
All data prior to t_f	634	661
All data prior to t_f + 1 range, 1 Doppler	638	719
Fractional increase in χ^2	$< 1\%$	9%
Screened data set		
	Yarkovsky model	Gravity-only model
All data prior to t_f	172	182
All data prior to t_f + 1 range, 1 Doppler	173	189
Fractional increase in χ^2	$< 1\%$	4%

Bibliography

Altman, N. S. 1992, The American Statistician, 46, 175

Benner, L. A. M., Nolan, M. C., Margot, J. L., et al. 2008, in Bulletin of the American Astronomical Society, Vol. 40, AAS/Division for Planetary Sciences Meeting Abstracts #40, 432

Bierman, G. J. 1977, "Factorization Methods for Discrete Sequential Estimation" (Dover)

Bottke, Jr., W. F., Vokrouhlický, D., Rubincam, D. P., & Nesvorný, D. 2006, Annual Review of Earth and Planetary Sciences, 34, 157

Burns, J. A. 1976, American Journal of Physics, 44, 944

Burns, J. A., & Safronov, V. S. 1973, MNRAS, 165, 403

Campbell, M. J., & Ulrichs, J. 1969, J. Geophys. Res., 74, 5867

Carry, B. 2012, PlanSS, 73, 98

Chesley, S. R., Baer, J., & Monet, D. G. 2010, Icarus, 210, 158

Chesley, S. R., Vokrouhlický, D., Ostro, S. J., et al. 2008, in Asteroids, Comets, Meteors 2008, Vol. 1405, 8330

Chesley, S. R., Farnocchia, D., Nolan, M. C., et al. 2014, Icarus, 235, 5

Ćuk, M., & Nesvorný, D. 2010, Icarus, 207, 732

De Angelis, G. 1995, Planet. Space Sci., 43, 649

Delbo, M., dell'Oro, A., Harris, A. W., Mottola, S., & Mueller, M. 2007, Icarus, 190, 236

Delbo, M., Libourel, G., Wilkerson, J., et al. 2014, Nature, 508, 233

DeMeo, F. E., Binzel, R. P., & Lockhart, M. 2014, Icarus, 227, 112

Deserno, M. 2004, How to generate equidistributed points on the surface of a sphere, https://www.cmu.edu/biolphys/deserno/pdf/sphere_equi.pdf

Evans, J. V., & Hagfors, T., eds. 1968, Radar Astronomy (New York: McGraw-Hill)

Evans, S., Taber, W., Drain, T., et al. 2016, in The 6th International Conference on Astrodynamics Tools and Techniques (ICATT), International Conference on Astrodynamics Tools and Techniques, Darmstadt, Germany

Fahnestock, E. G., & Scheeres, D. J. 2009, Icarus, 201, 135

Farnocchia, D., Chesley, S., Chamberlin, A., & Tholen, D. 2015, Icarus, 245, 94

Farnocchia, D., Chesley, S. R., Chamberlin, A. B., & Tholen, D. J. 2015, Icarus, 245, 94

Farnocchia, D., Chesley, S. R., Chodas, P. W., et al. 2013a, Icarus, 224, 192

Farnocchia, D., Chesley, S. R., Vokrouhlický, D., et al. 2013b, Icarus, 224, 1

Folkner, W. M., Williams, J. G., Boggs, D. H., Park, R. S., & Kuchynka, P. 2014, Interplanetary Network Progress Report, 196, 1

Fowler, J. W., & Chillemi, J. R. 1992, The IRAS Minor Planet Survey, 17

Fujiwara, A., Kawaguchi, J., Yeomans, D. K., et al. 2006, Science, 312, 1330

Gehrels, T., Roemer, E., Taylor, R. C., & Zellner, B. H. 1970, AJ, 75, 186

Giorgini, J. D., Ostro, S. J., Benner, L. A. M., et al. 2002, Science, 296, 132

Goldstein, R. M. 1969, Icarus, 10, 430

Greenberg, A. H., & Margot, J. L. 2015, AJ, 150, 114

Greenberg, A. H., Margot, J. L., Verma, A. K., et al. 2017, AJ, 153, 108

Hagfors, T. 1964, JGR, 69, 3779

Hanuš, J., Brož, M., Durech, J., et al. 2013, AAp, 559, A134

Harris, A. W. 1998, Icarus, 131, 291

Harris, A. W., Fahnestock, E. G., & Pravec, P. 2009, Icarus, 199, 310

Hudson, R. S. 1993, Remote Sensing Reviews, 8, 195

Hudson, R. S., & Ostro, S. J. 1994, Science, 263, 940

—. 1995, Science, 270, 84

Jacobson, S. A., Scheeres, D. J., & McMahon, J. 2014, ApJ, 780, 60

Jewitt, D., & Li, J. 2010, AJ, 140, 1519

Jones, E., Oliphant, T., Peterson, P., et al. 2001–, SciPy: Open source scientific tools for Python

JPL Solar System Dynamics. 2017a, JPL Radar Astrometry Database, `https://ssd.jpl.nasa.gov/?grp=ast&fmt=osod&radar=`

—. 2017b, JPL Small Body Database, `https://ssd.jpl.nasa.gov/sbdb.cgi`

Kalman, R. E. 1960, Transactions of the ASME–Journal of Basic Engineering, 82, 35

La Spina, A., Paolicchi, P., Kryszczyńska, A., & Pravec, P. 2004, Nature, 428, 400

Lawson, C. L., & Hanson, R. J. 1995, SIAM Classics in Applied Mathematics, Vol. 15, "Solving Least Squares Problems" (Philadelphia: Society for Industrial and Applied Mathematics)

Lowry, S. C., Fitzsimmons, A., Pravec, P., et al. 2007, Science, 316, 272

Magri, C., Consolmagno, G. J., Ostro, S. J., Benner, L. A. M., & Beeney, B. R. 2001, Meteoritics and Planetary Science, 36, 1697

Magri, C., Nolan, M. C., Ostro, S. J., & Giorgini, J. D. 2007a, Icarus, 186, 126

Magri, C., Ostro, S. J., Scheeres, D. J., et al. 2007b, Icarus, 186, 152

—. 2007c, Icarus, 186, 152

Magri, C., Ostro, S., Rosema, K., et al. 1999, Icarus, 140, 379

Mahapatra, P. R., Ostro, S. J., Benner, L. A. m., et al. 1999, lanss, 47, 987

Mainzer, A., Grav, T., Masiero, J., et al. 2012, ApJL, 760, L12

Mandel, J. 1964, The Statistical Analysis of Experimental Data (Dover Publications)

Margot, J. L., & Giorgini, J. D. 2010, in IAU Symposium, Vol. 261, IAU Symposium, ed. S. A. Klioner, P. K. Seidelmann, & M. H. Soffel, 183–188

Margot, J. L., Nolan, M. C., Benner, L. A. M., et al. 2002, Science, 296, 1445

Margot, J. L., Pravec, P., Taylor, P., Carry, B., & Jacobson, S. 2015, in Asteroids IV, 355–373

Micheli, M., Tholen, D. J., & Elliott, G. T. 2012, NA, 17, 446

Minor Planet Center. 2017, Minor Planet database, `http://minorplanetcenter.net/db_search`

Naidu, S. P., & Margot, J. L. 2015, AJ, 149, 80

Naidu, S. P., Margot, J. L., Busch, M. W., et al. 2013, Icarus, 226, 323

Nolan, M. C., Magri, C., Howell, E. S., et al. 2013, Icarus, 226, 629

Nugent, C. R., Margot, J. L., Chesley, S. R., & Vokrouhlický, D. 2012, Astronomical Journal, 144, 60

Ostro, S., Hudson, R., Jurgens, R., et al. 1995, Science, 270, 80+

Ostro, S. J. 1993, Reviews of Modern Physics, 65, 1235

Ostro, S. J., Benner, L. A. M., Magri, C., et al. 2005, Meteoritics and Planetary Science, 40, 1563

Ostro, S. J., Margot, J. L., Benner, L. A. M., et al. 2006, Science, 314, 1276

Peterson, C. A. 1976, PhD thesis, Massachusetts Institute of Technology.

Pettengill, G. H., Shapiro, I. I., Ash, M. E., et al. 1969, Icarus, 10, 432

Pravec, P., Harris, A. W., & Michalowski, T. 2002, in Asteroids III (Univ. of Arizona Press), 113–122

Press, W. H., Teukolsky, S. A., Vetterling, W. T., & Flannery, B. P. 1992, Numerical Recipes in C (2nd Ed.): The Art of Scientific Computing (New York, NY, USA: Cambridge University Press)

Rubincam, D. P. 1995, JGR, 100, 1585

—. 2000, Icarus, 148, 2

Scheeres, D. J., Fahnestock, E. G., Ostro, S. J., et al. 2006, Science, 314, 1280

Scheirich, P., Pravec, P., Jacobson, S. A., et al. 2015, Icarus, 245, 56

Stuart, J. S., & Binzel, R. P. 2004, Icarus, 170, 295

Takahashi, Y., & Scheeres, D. J. 2014, Celestial Mechanics and Dynamical Astronomy, 119, 169

Taylor, P. A., Margot, J. L., Vokrouhlický, D., et al. 2007, Science, 316, 274

Thomas, C. A., Trilling, D. E., Emery, J. P., et al. 2011, AJ, 142, 85

Verma, A. K., & Margot, J. L. 2016, JGR

Verma, A. K., Margot, J. L., & Greenberg, A. H. 2017, Astrophys. J., in press

Vokrouhlický, D. 1999, AAP, 344, 362

Vokrouhlický, D., Chesley, S. R., & Matson, R. D. 2008, AJ, 135, 2336

Vokrouhlický, D., & Farinella, P. 1998, AJ, 116, 2032

Vokrouhlický, D., Milani, A., & Chesley, S. R. 2000, Icarus, 148, 118

Warner, B. D. 2015, Minor Planet Bulletin, Vol. 42, http://www.minorplanet.info/MPB/MPB_424.pdf